THE ROLE OF ACTIVE CRUSTAL FAULTS IN GEOTHERMAL SYSTEMS IN
VOLCANIC AREAS: A CASE STUDY OF SOUTHERN CHILE BY
MAGNETOTELLURIC METHOD

Zur Erlangung des akademischen Grades eines

DOKTORS DER NATURWISSENSCHAFTEN (Dr. rer. nat.)

von der KIT Fakultät für Bauingenieur-, Geo- und Umweltwissenschaften

des Karlsruher Instituts für Technologie (KIT)

genehmigte

DISSERTATION

von
Maximiliano Alejandro Pavez Moreno

Tag der mündlichen Prüfung: 25.05.2023

Referent: Prof. Dr. Thomas Kohl
Korreferent: Prof. Dr. Bülent Tezkan

Karlsruhe 2023

Abstract

The Andean magmatic arc results from the on-going subduction of the Nazca and Antarctic beneath the South American Plates. The most active volcanoes in the Andes are concentrated in the Southern Volcanic Zone (SVZ) which extends from 33 to 46°S. This zone is characterized by the NNE-striking Liquiñe-Ofqui Fault Systems (LOFS), which extends over 1400 km and is offset by a group of NW-striking so-called Andean transverse faults (ATF).

Preferential fluid pathways along these regional fault systems are crucial for the spatial localization of surface manifestations in the Andean magmatic arc. Ranging from volcanoes to thermal springs, they represent the geothermal spectrum from high- to low temperature geothermal systems in this area. Both, magmatic (melt) and geothermal fluids, are linked to comparatively high electrical conductivity and thus, prone to electromagnetic exploration. Given the depth of occurrence, here, we use magnetotelluric methods to develop flow concepts for both, low- and high temperature, fault-driven geothermal systems in volcanic areas. The low-and high-temperature systems of the Pucón/Villarrica area including 29 thermal springs (geochemical temperature estimations ranging from 84 to 184°C) and the Tolhuaca area including geothermal wells with temperature between 160 and 300°C, respectively, are considered representative examples.

To identify the three-dimensional (3-D) effects generated by preferential fluid pathways in areas of interference between active cortical faults and volcanism surrounding the Pucón/Villarrica area, we used 31 broadband MT (BB-MT) stations deployed along E-W and N-S oriented profiles, intersecting the major fault systems. The 3-D inversion reveals eight electrical resistivity anomalies, which may be related to fluid pathways. Six of these anomalies are localized at a shallow-crustal level (<2 km) and are linked to volcanic or geothermal manifestations at the surface. Their connection to the surface is evident in the fault-related system, where the intersection of two damage zones may provide optimal vertical pathways. Highly conductive anomalies at mid-crustal level (>4 km and 2-5 km depth) coincide with or cross the

eastern branch of the LOFS, as well as with the Villarrica volcanic chain and the Mocha-Villarrica Fault Zone (MVFZ). In such classical step-over and fault intersections, fluids are presumed to accumulate in related damage zones acting as a vertical conduits extending to the surface. A proven link between the Villarrica volcanic chain and a deep anomaly (>8 km) could not be established thus far.

To better understand the context of the deep low resistivity anomalies in the Villarrica volcanic chain and to investigate the implications of crustal faulting and volcanism and their consequence on crustal reservoirs, long-period (LP-MT) and broadband (BB-MT) magnetotelluric data were acquired surrounding of Villarrica volcano. The resistivity distribution shows the upper crust as highly resistive, but below and east of Villarrica volcano, the model suggests the presence of a magmatic reservoir at shallow crustal levels (between 1.5 and 3 km b.s.l.). This may well be a temporary magma storage zone. The middle crust contains several intermediate to low conductive features interpreted as fluid pathways and melt storage channels, revealing the important role of the fault systems. The lower crust contains zones of low resistivity suggesting the presence of partial melt and/or fluids, associated with deep reservoirs (8-20 km). They may represent a deep source; a significant proportion of this volume is likely to be distributed in non-eruptible parts of the reservoir. This would suggest that the melt is accumulated as highly crystallized mush or disconnected melt pockets. We concluded, that the fault core can act as a conduit for fluid flow during deformation and as a barrier when open pores are filled with precipitated minerals after deformation.

To investigate the role of faults in the other geothermal end-member, a high-temperature field, the Tolhuaca volcano has been studied along its northwest flank using 3-D inversion of MT data. The 3-D MT model depicts a conductive body at ∼2 km beneath Tolhuaca volcano, would correspond to the long-term residence of a subsurface magmatic intrusion associated with ATF structural control. Since we found no indications of a deep conductor in the study area, such as those observed in other high enthalpy geothermal systems, we conclude that the shallow magmatic deposit, which is cooling but still hot, is the heat source of the geothermal system. It is not located beneath the geothermal field but laterally offset. Therefore, the prevailing tectonic configuration in the Tolhuaca system, the interaction between LOFS and ATF, would promote the development of a long-lived shallow reservoir. On the other hand, we also detect a 300 m thick layer of high conductivity associated with argillic hydrothermal alteration. The MT model includes two resistive

bodies in the upper crust beneath the laterally displaced argillic alteration layer to the west beneath the extinct Tolhuaca, which would correspond to a shallow reservoir (1000 m from the surface) and a deep reservoir (>1800 m from the surface) that previous resistivity models had not identified.

Zusammenfassung

Der magmatische Bogen der Anden ist das Ergebnis der anhaltenden Subduktion der Nazca- und der Antarktischen Platte unter die Südamerikanische Platte. Die aktivsten Vulkane der Anden sind in der Südlichen Vulkanzone (SVZ) konzentriert, die sich von 33 bis 46°S erstreckt. Diese Zone ist durch das NNE-streichende Liquiñe-Ofqui-Verwerfungssystem (LOFS) gekennzeichnet, das sich über 1400 km erstreckt und von einer Gruppe NW-streichender so genannter Andean Transverse Faults (ATF) abgelöst wird.

Bevorzugte Flüssigkeitswege entlang dieser regionalen Verwerfungssysteme sind entscheidend für die räumliche Lokalisierung von Oberflächenerscheinungen im magmatischen Bogen der Anden. Sie reichen von Vulkanen bis hin zu Thermalquellen und repräsentieren das geothermische Spektrum von Hoch- bis Niedertemperatur-Geothermiesystemen in diesem Gebiet. Sowohl magmatische (Schmelze) als auch geothermische Fluide sind mit einer vergleichsweise hohen elektrischen Leitfähigkeit verbunden und daher anfällig für elektromagnetische Exploration. Angesichts der Tiefe des Vorkommens verwenden wir hier magnetotellurische Methoden, um Strömungskonzepte für verwerfungsbedingte geothermische Systeme mit niedrigen und hohen Temperaturen in vulkanischen Gebieten zu entwickeln. Die Nieder- und Hochtemperatursysteme des Pucón/Villarrica-Gebiets mit 29 Thermalquellen (geochemische Temperaturschätzungen reichen von 84 bis 184°C) und des Tolhuaca-Gebiets mit geothermischen Bohrungen mit Temperaturen zwischen 160 und 300°C werden als repräsentative Beispiele betrachtet.

Um die dreidimensionalen (3-D) Effekte zu identifizieren, die durch bevorzugte Flüssigkeitswege in Bereichen mit Interferenzen zwischen aktiven kortikalen Verwerfungen und Vulkanismus in der Umgebung des Pucón/Villarrica-Gebietes entstehen, haben wir 31 Breitband-MT-Stationen (BB-MT) verwendet, die entlang von E-W- und N-S-orientierten Profilen aufgestellt wurden und das Hauptverwerfungssystem durchschneiden. Die 3-D-Inversion zeigt acht Anomalien des elektrischen Widerstands, die mit Flüssigkeitswegen in Verbindung stehen könnten. Sechs dieser Anomalien befinden sich in einer

flachen Krustenebene (<2 km) und sind mit vulkanischen oder geothermischen Erscheinungen an der Oberfläche verbunden. Ihre Verbindung zur Oberfläche ist bei dem verwerfungsbedingten System offensichtlich, bei dem die Kreuzung zweier Schadenszonen optimale vertikale Pfade bieten kann. Stark leitfähige Anomalien auf mittlerer Krustenebene (>4 km und 2-5 km Tiefe) fallen mit dem östlichen Zweig der LOFS sowie mit der Villarrica-Vulkankette und der Mocha-Villarrica-Verwerfungszone (MVFZ) zusammen bzw. kreuzen die LOFS. Bei solchen klassischen Übergängen und Verwerfungen wird davon ausgegangen, dass sich Fluide in den entsprechenden Schadenszonen ansammeln und als vertikale Kanäle an die Oberfläche führen. Eine nachgewiesene Verbindung zwischen der Villarrica-Vulkankette und einer tiefen Anomalie (>8 km) konnte nicht nachgewiesen werden.

Um den Kontext der tiefen Anomalien mit niedrigem spezifischen Widerstand in der Villarrica-Vulkankette besser zu verstehen und die Auswirkungen von Krustenverwerfungen und Vulkanismus sowie deren Folgen auf die Krustenreservoirs zu untersuchen, wurden langperiodische (LP-MT) und breitbandige MT-Daten in der Umgebung des Villarrica-Vulkans erfasst. Die gemeinsame Inversion der Daten wurde genutzt, um ein neues dreidimensionales Modell des elektrischen Widerstands der Kruste zu erstellen. Die Verteilung des spezifischen elektrischen Widerstands zeigt, dass die obere Kruste einen hohen Widerstand aufweist. Unterhalb und östlich des Vulkans Villarrica deutet das Modell jedoch auf das Vorhandensein eines magmatischen Reservoirs in flachen Krustenschichten (zwischen 1,5 und 3 km ü.d.M.) hin. Dabei könnte es sich durchaus um eine temporäre Magmaspeicherzone handeln. Die mittlere Kruste enthält mehrere mittel- bis niedrigleitende Merkmale, die als Flüssigkeitswege und Schmelzespeicherkanäle interpretiert werden, was die wichtige Rolle der Verwerfungssysteme verdeutlicht. Die untere Kruste enthält Zonen mit niedrigem spezifischen Widerstand, die auf das Vorhandensein von partieller Schmelze und/oder Fluiden hindeuten und mit tiefen Reservoiren (8-20 km) in Verbindung stehen. Sie könnten eine tiefe Quelle darstellen; ein erheblicher Teil dieses Volumens ist wahrscheinlich in nicht eruptiven Teilen der Lagerstätte verteilt. Dies würde darauf hindeuten, dass die Schmelze in Form von hochkristallisiertem Brei oder unzusammenhängenden Schmelztaschen akkumuliert ist. Wir kamen zu dem Schluss, dass der Verwerfungskern während der Verformung als Kanal für den Flüssigkeitsstrom und nach der Verformung als Barriere fungieren kann, wenn die offenen Poren mit ausgefällten Mineralien gefüllt sind.

Um die Rolle von Verwerfungen im anderen geothermischen Endglied, einem

Hochtemperaturfeld, zu untersuchen, wurde der Vulkan Tolhuaca entlang seiner Nordwestflanke mit Hilfe der 3-D-Inversion von MT-Daten untersucht. Um ein Modell zu erhalten, das mit der Geologie übereinstimmt, wurde eine Reihe von 3-D-Inversionsversuchen mit MT durchgeführt, bei denen die Daten des Impedanztensors (Z) und der geomagnetischen Übertragungsfunktion (T) gemeinsam invertiert wurden, wobei nicht-diagonale und diagonale Komponenten von Z verwendet wurden. Schließlich wurden bei der Inversion alle Z-Komponenten sowie die T-Komponenten einbezogen, um die Empfindlichkeit in der Tiefe zu verbessern und die seitlichen Beschränkungen zu untersuchen. Das endgültige 3D-MT-Modell zeigt einen leitfähigen Körper in ~2 km unterhalb des Vulkans Tolhuaca, was dem langfristigen Verbleib einer unterirdischen magmatischen Intrusion in Verbindung mit der strukturellen Kontrolle des ATF entsprechen würde. Da wir im Untersuchungsgebiet keine Hinweise auf einen tiefen Leiter gefunden haben, wie sie in anderen geothermischen Systemen mit hoher Enthalpie beobachtet werden, schließen wir, dass die oberflächliche magmatische Ablagerung, die sich abkühlt, aber immer noch heiß ist, die Wärmequelle des geothermischen Systems ist. Sie befindet sich nicht unter dem geothermischen Feld, sondern ist seitlich versetzt. Daher würde die vorherrschende tektonische Konfiguration im Tolhuaca-System, die Interaktion zwischen LOFS und ATF, die Entwicklung eines langlebigen flachen Reservoirs fördern. Andererseits stellen wir auch eine 300 m dicke Schicht mit hoher Leitfähigkeit fest, die mit argillischer hydrothermaler Alteration verbunden ist. Das MT-Modell umfasst zwei Widerstandskörper in der oberen Kruste unter der seitlich verschobenen argillischen Alterationsschicht westlich unter dem erloschenen Tolhuaca, die einem flachen Reservoir (1000 m von der Oberfläche) und einem tiefen Reservoir (>1800 m von der Oberfläche) entsprechen würden, die in früheren Widerstandsmodellen nicht identifiziert worden waren.

Contents

1. Introduction

The Earth's crust is composed of different tectonic plates. These drift apart, collide or slide towards another plate. Oceanic plate sliding towards a continental plate, subduction zones form, such as around the Pacific Ring of Fire. The oceanic plate sinks together with the sea water and the sediment by which it has been covered and penetrated. Heat and pressure cause mineral transformations which leads to the release of fluids such as water and gases at a depth of about 90-120 km. If the water released from the subducting plate penetrates the wedge-shaped overlying mantle, it reduces the melting point of the mantle rock. The resulting magmas ascend and create elongated chains of volcanoes on the continental plate as, for example, along the Andes or in New Zealand. The Andes serves as a natural laboratory and are an ideal location to study the Earth's dynamics and, in particular, the crustal mechanisms that control fluid transport processes.

Magma that reaches the surface can become in lava or remains trapped in large quantities below ground. Existing rocks that come into contact with magma may be melted and assimilated into the magma. Other rocks adjacent to the magma may be altered as they are affected by the heat and escaping or externally-circulating hydrothermal fluids. The hydrothermal circulation creates various hot water phenomena such as hot springs, fumaroles and geysers on the earth's surface. Fluids rich in minerals circulating at crustal levels through complex fracture network are important pathways for the migration, ascent and/or emplacement of deep-seated fluids in hydrothermal systems. The detection and imaging of fluids are considered as an important factor in the exploration of geothermal systems in volcanic environments and was the main objective described in this work.

The evolution of hydrothermal systems in the Andes Mountains of south-central Chile, where abundant geothermal resources, have recently been explored by mineralogical, geochemical and geophysical studies. This region also offers the opportunity to explore the relation between brittle deformation and heat-fluid-rock interaction because active hydrothermal systems occur

in close spatial relationship with volcanism, as well as with major seismically active fault systems (Cembrano and Lara 2009). Proof of this, is a high number of low-medium temperature thermal manifestations located along the fault systems or/and in the vicinity of the volcanic systems. The presence of fluids in the crust is related to a higher electrical conductivity, so there may be a direct connection between fluids trapped or flowing along fault systems and a magnetotelluric target. Thus, geological structures can be visualized through the electrical response using the magnetotelluric method.

Magnetotelluric (MT) is a passive geophysical method that uses as a source a wide spectrum of naturally occurring geomagnetic variations that generate electromagnetic induction in the Earth. By simultaneously measuring of fluctuations in the natural electric and magnetic fields in orthogonal directions at the surface of the Earth, a subsurface resistivity model can be generated (Simpson and Bahr 2005). Knowing the behavior of electromagnetic waves as they propagate into the earth's interior, it is possible to correlate the electrical resistivity contrasts with existing geological structures important for the migration, ascent and/or emplacement of deep-seated fluid.

Examining the nature, spatial distribution, and geometry faults and fracture networks can help to unravel the fundamental processes operating on both ancient and active geothermal systems in volcanic areas. One of the main geological structures present in the study area corresponds to the Liquiñe-Ofqui Fault System (LOFS), an intracortical fault system characterized by linear faults, presence of hot springs, monogenetic cones, and large depressions aligned along the main trace (Cembrano et al. 1996).

1.1. Exploration for geothermal systems in volcanic areas

As the world is looking to replace fossil fuels, the development of economically viable renewable energy sources is gaining interest. One of the renewable sources that provides an alternative is geothermal energy. In a geothermal system, the Earth's natural temperature gradient is used as a means to produce energy by transferring heat in fluids, either naturally occurring within the Earth or by injecting fluids. However, to generate energy efficiently, permeable pathways must first be established within the hot lithologies, as fluids play an important role in the utilization of the geother-

mal system, as they are necessary to transport heat from the reservoir to the surface.

The Andean geological context is favorable for the presence of geothermal systems with magmatic influence in terms of heat source, volcanism and thermal waters. Magmatic fluids can be a direct source of heat and fluids for the hydrothermal system. In south-central Chile, two distinct domains of geothermal systems, structural (non-volcanic) and volcanic have been identified (Alam et al. 2010). These two domains are distinct in their ways of heating meteoric water, which is the feeder of these geothermal systems. Volcanic domain of geothermal systems are associated with regional volcanic centers. The heating process is through deep circulation of meteoric water in the case of structural domain geothermal systems. In the case of volcanic domain geothermal systems, the heating of meteoric water is through heat absorption and condensation of steam and gases by the meteoric water during lateral circulation.

Despite the geothermal systems have been studied in the Andes, there is little scientific information on the characterization of their hydrothermal circulations pathways. A better understanding of the crustal inheritance and structural control on Andean arc magmatism is key to develop an exploration of geothermal systems, since one of the main unknowns is the tracking and characterization of the location of fluids in the crust.

1.2. The role of faults

The configuration of tectonic plates has a fundamental influence on the characteristics of a geothermal system. The thermal regime and heat flow, hydrogeological regime, fluid dynamics, fluid chemistry, faults and fractures, stress regime and lithological sequence are controlled by the plate tectonic framework and are fundamental to understanding the geothermal system (Gianelli and Grassi 2001). The thermal state of the crust at active plate boundaries is different from that of other large-scale geologic provinces, such as tectonically inactive environments, major fault zones (active or inactive), or sedimentary basins.

At tectonic plate margins, or in environments of active tectonism or volcanism, fluid flow induced by a heat source or high heat flow transports heat from deeper levels to the surface preferentially through zones of weaknesses

or permeabilities. Thus, structural controls have an important effect on fluid flow pathways (Pruess and Bodvarsson 1984). The permeability architecture is defined by the geometry and kinematics of fault-fracture networks (e.g. Sibson 1996). Faults may act as impermeable barriers to cross-fault flow or as high permeability conduits, although their permeability relative to the host rock depends on fault displacement, host rock lithology, hydrothermal mineral precipitation, and the seismic cycle (Sibson 1994).

The major crustal faults and fold systems of the convergent margins are usually organized in margin-parallel high-strain domains that form the first-order architecture of the orogenic belts. However, second-order structures oblique to the orogen can also be found within the overall margin-parallel structural grain that characterizes the convergent margins. Regional-scale transverse structures along the Andes cut across the well-organized N-S architecture of the central and southern Andean orogen (Melnick and Echtler 2006; Glodny et al. 2008). In the southern Andes Volcanic Zone, between 39° and 46°S, the volcanic and hydrothermal activity is controlled by the NNE-trending Liquiñe-Ofqui Fault System (LOFS) and the NW-striking Andean Transverse Faults (ATF), which host ∼25% of geothermal features in the Chilean Andes (Lahsen et al. 2010; Sánchez et al. 2013).

1.3. The Pucón/Villarrica and Tolhuaca areas

The research work was carried out within the Andean mountain range in the Central Southern Volcanic Zone (CSVZ), where the structural control is linked to the main geological features; the Liquiñe-Ofqui Fault System, which runs parallel to the Andean mountain range (Cembrano et al. 1996) and the Andean Transverse Faults, which includes a series of steeply- dipping NW-striking faults, most likely inherited from a pre-Andean architecture (Radic et al. 2002), with sinistral-reverse kinematics and local normal-slip re-activation (Pérez-Flores et al. 2016). In this work, two areas belonging the CSVZ have been investigated. The first one, is located in the vicinity of active Villarrica volcano, area called Pucón/Villarrica area. Meanwhile, the second one is located in the surrounding area of dormant Tolhuaca volcano, area called Tolhuaca area, which have the singularity that include the only one high-enthalpy geothermal system along the SVZ.

Villarrica volcano is located in the IX region of Araucanía, Chile, 100 km southeast of the city of Temuco, and is one of the most active volcanoes

of CSVZ. Villarrica volcano is placed at the northern end of the LOFS. Together with the LOFS, the central component that characterizes the system associated with Villarrica volcano is the volcanic chain aligned in a NW-SE direction composed of the major stratovolcanoes: Villarrica (2847 m a.s.l.), Quetrupillán (2360 m a.s.l.) and Lanín (3774 m a.s.l.) (Moreno and Clavero 2006). Villarrica is an active volcano that presents an almost perfect conical shape although the topography of its base is extremely irregular. The average height of its base can be estimated at 400 m a.s.l. The crater of 200 m diameter, open at the top is active, and shows continuous fumarolic activity (Lara 2004). At its bottom there is an almost permanent lava lake that varies between 50 and 100 m (Moreno and Clavero 2006), and sometimes forms small pyroclastic cones. The last relevant eruptive episode occurred in 2015. In the Villarica system area there are more than twenty thermal manifestations on the surface, of which some thermal areas are spatially associated with active stratovolcanoes, the Liquiñe-Ofqui Fault System or fault systems oblique to the arc.

Tolhuaca volcano is located in the border between Bío-Bío and Araucaní regions in southern Chile, 100 km northeast of the city of Temuco. Tolhuaca (2806 m a.s.l.) is a glacially scoured composite stratovolcano of late-Pleistocene to Holocene age that rises ~900 m over the basement (Thiele et al. 1987; Lohmar et al. 2012a). In the summit there are several NW-trending aligned craters with different degrees of preservation that indicate a migration of the volcanic activity from SE towards the NW (Thiele et al. 1987; Moreno and Gardeweg 1989). The latest eruptive phases are at the NW flank and correspond to a NW-trending fissure (~2 km long) and a pyroclastic cone (Thiele et al. 1987). Lavas are predominantly basaltic andesites and andesites, with minor presence of basalts and dacites (Thiele et al. 1987). Tolhuaca volcano and its surrounding area host a number of geothermal features, including natural springs, wells and fumaroles. On the northwest flank of Tolhuaca, geothermal exploration carried out by private companies (Melosh et al. 2010; Lohmar et al. 2012a; Melosh et al. 2012) indicating the presence of a high-enthalpy reservoir (250-300°C) located below Tolhuaca volcano at ~1-2 km. However, the Tolhuaca geothermal system still remain unexploited.

1.4. Thesis Structure

The first part of this work comprises the geological background of the study area (Chapter 2). The theoretical basis of the magnetotelluric method is presented in chapter 3. Furthermore, in chapter 3 the data processing is clarified as well as the inversion method with a three-dimensional approach. The results of the study of the role of fault systems in geothermal systems associated with volcanic systems are presented in the form of individual manuscripts, which are published (Chapter 4 and 6) or submitted (Chapter 5) to international journals. Chapter 4 presents the 3-D inversion model of broad-band magnetotelluric data and the interpretation of the most important features of these results. Chapter 5 presents a 3-D model that combines long- and broad-band magnetotelluric data, providing a visualization of the main geological structures in a model along the crust. Chapter 6 presents a 3-D model with a comprehensive understanding of the geoelectric properties of the geothermal system associated with Tolhuaca volcano. Finally, some concluding remarks are presented in Chapter 6.

Electrical image of faults in the upper-middle crust (chapter 4)

Fault zones are linked as the main geological structures that accomplish fluid circulation in the geothermal systems. In order to investigate the role of upper-mid crustal faults in the geothermal systems in areas surrounding the Villarrica-Lanín volcanic chain, magnetotelluric stations have been deployed distributed perpendicular to the branches of the Liquiñe-Ofqui Fault System (LOFS) and sub-perpendicular to an Andean Transverse Fault that runs parallel to the Villarrica-Lanín volcanic chain; Mocha-Villarrica Fault Zone (MVFZ). The two intersecting fault systems are conspicuously detected in the inversion results of the magnetotelluric data, revealing low-to-intermediate electrical resistivity responses at shallow depths. Thus, LOFS is identified as a subvertical fault that intersects a resistive upper crust. In addition, intermediate resistivity minima along the LOFS coincide with thermal sources and monogenetic volcanic activity as well as magma ascent near the active Villarrica volcano. In turn, MVFZ is characterized as a north-dipping fault zone connected to a mid-crustal conductor beneath the volcanic chain.

Broad understanding of the major geological features in the volcanic chain (chapter 5)

Tectonic and morphostructural controls on a volcanic internal structure pro-

vide important insights into the dynamics of a volcano. Despite, identifying these structures is a major challenge due to their complexity. Joint inversion of long- and broad-band magnetotelluric stations deployed in the surrounding area of Villarrica volcano aims to complement the conductivity models revealed in previous MT studies and investigate the implications of crustal faulting and volcanism and their consequence on crustal reservoir. The 3-D resistivity distribution shows the upper crust as highly resistive, but below and east of Villarrica volcano, the model suggests the presence of a shallow magmatic reservoir (between 1.5 and 3 km b.s.l), possibly correspond to a temporary magma storage. The upper crust contains several intermediate to low conductivity anomalies interpreted as fluid pathways, melt storage associated with non-vertical ascending conduits, which would be related to the N10°E Liquiñe-Ofqui Fault System. The lower crust contains zones of low resistivity material indicating the presence of partial melt and/or fluids, associated with deep reservoirs (8-20 km). They may represent a deep source; a significant proportion of this volume is likely to be distributed in non-eruptible parts of the reservoir. This would suggest that the melt is accumulated as highly crystallized mush or disconnected melt pockets.

Geoelectrical properties characterizing main features in the upper-middle crust (chapter 6)

The relationship between the role of major/minor tectonic features in fluid transport and magma ascent processes is crucial to understand processes in geothermal systems in volcanic areas. In order to explore the effect of fluids that improve electrical conductivity, a three-dimensional (3-D) inversion of magnetotelluric (MT) data has been used to examine the geoelectric characteristics of the geothermal system associated to Tolhuaca volcano. In order to gain a better knowledge of Tolhuaca volcano's magmatic and hydrothermal systems, this work presents the first resistivity model of the volcano obtained through 3-D MT inversion. For 3-D inversion, we chose data from 54 MT stations. The new 3-D MT model shows a conductive body that is inferred to represent a shallow magmatic storage compartment and is situated 3 km beneath Tolhuaca volcano. A 300 m thick layer of high conductivity that corresponds to argillic hydrothermal alteration is also seen. A shallow reservoir (1000 m from the surface) and a deep reservoir (> 1800 m from the surface) that had not yet been identified by earlier resistivity models are included in the MT model as two resistive bodies (200 m) in the upper crust beneath the laterally displaced argillic alteration layer to the west beneath the extinct Tolhuaca. The findings here presented offer new

perspectives of the complexity on the Tolhuaca geothermal system.

2. Geological setting

The Andes have become a place of high scientific interest because here it is possible to observe the result of millions of years of processes associated with the subduction zone. This subduction zone has resulted in uplift, orogenies, and volcanism, creating the Andes mountain range that runs along the entire western margin of the Southern Andes. The Andean subduction zone can be grouped into segments according to tectonic evolution as well as volcanism. These four regions, based on active Holocene volcanism (Figure 2.1; Stern 2004) are: the Northern Volcanic Zone (Colombia and Ecuador), the Central Volcanic Zone (Perú and Chile), the Southern Volcanic Zone (Chile), and the Austral Volcanic Zone (Chile).

The segment of the Southern Andes has gained significant attention due to the extraordinary geothermal energy potential associated with the magmatic arc. Currently, main scientific research studies, in term of the role of active crustal faults in geothermal systems in volcanic areas, are being carried out in the central and southern zones of Chile.

This chapter provides a general description of the geology, magmatism and tectonic processes of the Andes, focused in Chile on the 37°S to 41°S latitudes. A segment well-know as the Central Southern Volcanic Zone of the Andes, the region where the areas of study are found. Moreover, a detailed relationship between geothermal systems associated with active volcanic systems and fault systems are presented.

## 2.1. The Andean margin

The Andean margin is controlled by the subduction of the Nazca and Antarctic oceanic plates below the continental lithospheric plate in the past ~200 m.y. and currently conformation is ongoing, with a convergence rate between the Nazca and continental plates of South America occuring at a present speed 6.6 cm/year with an azimuth of 078° (Kendrick et al. 2003). However,

movement is more likely to have occurred at mean rate of ~8.5 cm/year during the past several million years (DeMets et al. 1990), confirming that the convergence rate has changed over time (e.g. Charrier et al. 2002). The convergence rate between the Antarctic and South American Plate has a velocity of 2.2 cm/year (DeMets et al. 1990) and, as a result, the tectonic and magmatic activity has traversed through several evolutionary stages, generating a variety of geological features, revealing different magmatic events, which are related to changes in the geodynamics of the ocean floor and changes in both the speed and the obliquity of the subducting plate. However, orogenic features such as the magmatic arc provide evidence of a tectonically active margin and magmatism related to subduction.

The active subduction process resulted in the formation of a magmatic arc that has migrated eastwards reaching the main Andean Cordillera due to tectonic erosion. The main Cordillera, a more than 8000 km long morphologically continuous mountain chain along the western margin of South America, reaches a highest altitude of ~7 km and with a maximum width extension of 800 km (Kay et al. 1989). Volcanism occurs in four separate regions named the Northern (NVZ, 5°N-2°S), Central (CVZ, 14-27°S), Southern (SVZ, 33-46°S) and Austral (AVZ, 49-55°S) Volcanic Zones (Figure 2.1). The first three volcanic regions are separated by flat-slab segments (Peruvian, 5-14°S and Pampean, 27-33°S), associated with shallow subduction angles related to the subduction of the thickened oceanic crust, causing an absence of volcanic activity, while the most austral segment is interrupted by a Patagonian volcanic gap (46-49°S) associated with the Chile rise. Each of these four volcanic regions is, in turn, divided into several smaller volcanic arc segments. The division between larger zones, and between smaller segments, and differences in the erupted magmas in each segment of each zone, reflect the geological and tectonic segmentation of the Andes Mountains (Stern 2004).

2.2. Southern Volcanic Zone

The volcanic region with the highest number of active volcanoes corresponds to the Southern Volcanic Zone (33-46°S) that includes more than 50 active volcanic edifices in Chile and Argentina, as well as three giant silica caldera systems and numerous minor eruptive centers (Figure 2.2; Stern 2004). Among the larger, active and known volcanic centers in the SVZ are Planchón-Peteróa volcanic complex, Laguna del Maule, Nevados de Chillán complex, Lonquimay volcanic complex, Copahue-Caviahue caldera complex,
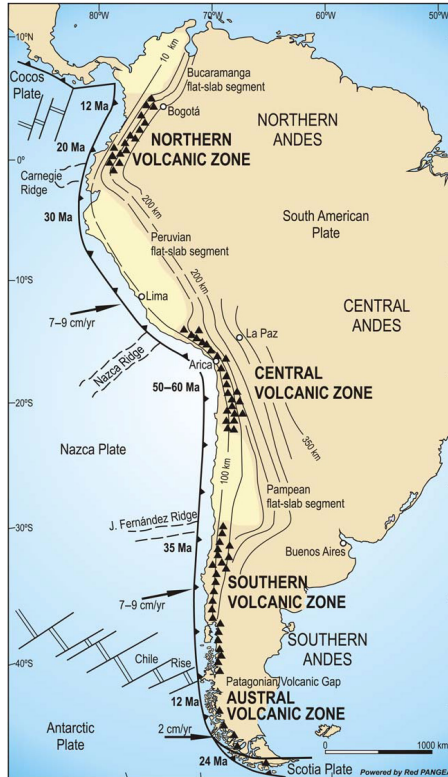
Figure 2.1.: Schematic map of geological setting of South America with the subduction zone grouped in segments according the tectonic and volcanism, modified from Stern 2004.

Llaima, Villarrica, Osorno, Puyehue-Cordón Caulle and Calbuco, all with eruptions in the last fifteen years with the exception of Laguna del Maule. However, Laguna del Maule is the only volcanic complex that has been experiencing an unprecedented and ongoing upward deformation of the soil in excess of 20 cm/year since 2007 (Cordell et al. 2019).

The northern end of the SVZ is associated with the intersection of the Juan Fernandez Ridge with the Chile-Peru Trench, meanwhile the southern end of the SVZ is linked with the triple junction Nazca-Antarctic-South American plates (López-Escobar et al. 1993). The entire SVZ, the Nazca plate is being subducted below the continental plate at 7-9 cm/year in a direction 22-30° northeast of orthogonal with the trench. The subduction angle increases from

~20° at the northern end to >25° to the south. Consequently, the distance from the trench to the volcanic front decreases from >290 km in the north to <270 km in the south, and the depth to the subducted slab below the front decreases from 120 to 90 km. Crustal thickness also decreases southwards from >50 km below the northern end of the SVZ to approximately 30-35 km below the southern end.

The SVZ has been divided into the northern, transitional, central and southern segments (Stanley and Tinkler 1983). The northern (NSVZ, 33-34°S) is delimited by the Juan Fernandez Ridge (northern end) and a boundary of different geochemical regime (southern end), characterized by a lack of basalts and basaltic andesites (Tormey et al. 1991). The transitional (TSVZ, 34.5-37°S) is delimited by the Juan Fernandez Ridge (northern end) and Mocha Fracture Zone (southern end). Here, the stratovolcanoes occur on an uplifted pre-volcanic basement separated by inter-arc extensional basins (Folguera et al. 2002) and characterized by a zone of melting, assimilation, storage, and homogenization (MASH) at the base of the continental crust, generating andesitic to rhyolite magmas. The central (CSVZ, 37-41,5°S) delimited by the Mocha Fracture Zone (northern end) and the Valdivia Fracture Zone (southern end). The southern (SSVZ, 41,5-46°S) delimited by the Valdivia Fracture Zone (northern end) and the triple junction Nazca-Antarctic-South American plates (southern end). A prominent tectonic feature in the CSVZ and SSVZ is the 1000 km long, ~N10°E tending Liquiñe-Ofqui Fault zone. Quaternary volcanic have at SSVZ Paleozoic to Mesozoic basement and Miocene to Pliocene volcanic formations (López-Escobar et al. 1993).

The SVZ has distinct arc-parallel morpho-structural units: The Coastal Cordillera, Central Valley and the Main Andean Cordillera. From west to east the first morpho-structural unit located is The Coastal Cordillera, which is separated by the Central Valley from The Main Andean Cordillera (Figure 2.3). The volcanoes of the SVZ occur in the Main Cordillera (Figure 2.3). A prominent tectonic feature in the CSVZ and SSVZ is the 1200 km long, ~N10°E tending Liquiñe-Ofqui Fault System (Cembrano et al. 2000; Cembrano et al. 1996), which along with northeast-southwest and northwest-southeast lineaments, control the location of some of the larger stratovolcanoes and hundreds of small monogenetic Holocene minor eruptive centers in the CSVZ and SSVZ (Stern 2004).

The volcanic front of the CSVZ occurs in Chile west of the continental divide, and in the southern part of the CSVZ along the boundary of the Central
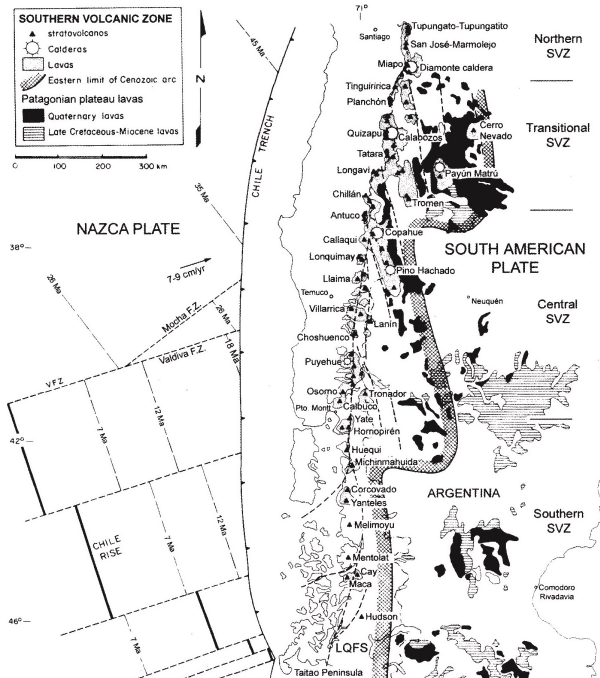
Figure 2.2.: Southern Volcanic Zone, modified from Stern 2004.

Valley and the western edge of the Main Cordillera. The volcanic front of the CSVZ either migrated to the west to its current position in the Late Pleistocene (Stern 2004), and the volcanic activity along the current front increased significantly at this time (Lara et al. 2001).

2.2.1. Tectonic setting

The main limits of the strike segment along the central and southern Andes occur at 33°S, with the southern end of the flat slab section, collision of the Juan Fernandez chain hot-spot and extreme north from the South Volcanic Zone; at 38°S, between the South Center and the Patagonian Andes with changes in the kinematics, topography, structural style of deformation assets and degree of deformation division; and at 46.5°S, between Patagonia and the Austral Andes with a collision between the Chilean expansion center and
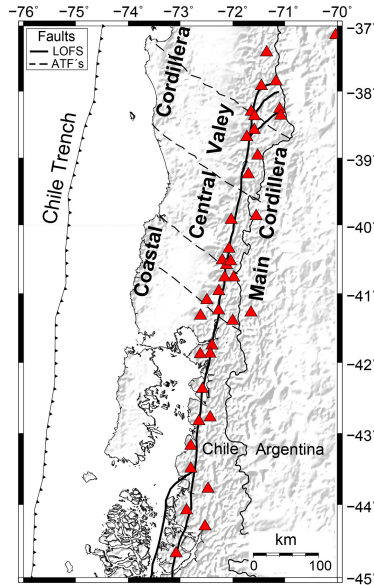
Figure 2.3.: Morpho-tectonic and structural setting of Southern Volcanic Zone.

the southern end of the South Volcanic.

Holocene volcanism in CSVZ and SSVZ is presumably controlled by the main predominant tectonic features of southern Chile, resulting from the oblique convergence that, with its component of the deformation partition, has acted in this region during the Paleogene and Miocene (Folguera et al. 2002), the Liquiñe-Ofqui Fault System (LOFS) (Cembrano et al. 1996; Charrier et al. 2002). A shear system runs parallel to the trench in direction N10°E, ~280 km westward from the trench, extending for more than 1000 km from the triple junction of the Antarctic, South American and Nazca plates to 38°S (Cembrano and Lara 2009). LOFS is characterized by bunches of NS to NNE-SSW alignments along the magmatic arc, regional-scale faults, horse-tails, graben, bending basins and fault separation, and is marked by a chain of stratovolcanoes, including some of the most active volcanoes in South America, e.g. Villarrica, Llaima and Lonquimay. Most volcanoes are located directly on the LOFS or along secondary structures that run parallel to the arc (Lavenu and Cembrano 1999; Melnick et al. 2006; Rosenau et al. 2006). However, regardless of this roughly NNE-SSW distribution of the large stra-

tovolcanoes, several minor eruptive centers, parasitic vents and flank craters are more well aligned with NE-SW and as well as NW-SE, both obliquely oriented to the LOFS. López-Escobar et al. 1995 have related the oblique-arc trend lines, N50-70°E with the maximum horizontal stress (S_H) in the arc region. and have postulated a system of crust fractures and stress cuts that allow the ascent of molten material or partially melted to the surface and generate feeder dikes for the crust. The activity of LOFS along the current SVZ volcanic arc zone begins between Neogene-Quaternary (Lavenu and Cembrano 1999). At the northern end, transpressional systems show post-glacial activity and are associated with the trace of the volcanic arc (Folguera et al. 2002), forming an east vergent set of high angle fault zones in form of an active fan or horsetail structure (Folguera et al. 2004). In the CSVZ segment, Quaternary deformation and Pliocene transpressional patterns result in vertical subsurface geometries (Lavenu and Cembrano 1999), partially controlling the paleo and recent fluid movement (Sánchez et al. 2013; Lara et al. 2006a). Moreover, in the southern end, the deformation front migrates between the Pliocene and the Quaternary, towards the Cordillera near the uprising line of the Patagonian Batholith (Folguera et al. 2002), accommodating structures in transpressional systems of positive flower (Thomson 2002).

The secondary predominant tectonic characteristics of southern Chile correspond to the oblique arch and trench fault system, Andean Tranverse Faults (ATF) (Pérez-Flores et al. 2016; Sánchez et al. 2013). Oriented NW-SE it crosses the arch and fore arch. At the western limit of the Longitudinal Valley, the fault system continues with strikes from N30°E to N40°E (Lavenu and Cembrano 1999). In the CSVZ the Bíobío-Alumine Fault (Pérez-Flores et al. 2016), Gastre Fault (Rapela and Pankhurst 1992), Lanalhue Fault (Glodny et al. 2008) and Mocha-Villarrica Fault (Melnick and Echtler 2006) constitute the ATF. Mocha-Villarrica, Lanalhue and BíoBío-Alumine Fault Zones, which also run obliquely to the main morphostructural units, are considered an inherited pre-Andean structure, continuously reactivated. The fault zones have been active since the Mesozoic and are therefore a long-lived structure that reactivates repeatedly in response to changes in subduction geometry. The subduction conditions modified by reorganization in the subducting plate affect the stress field and are reflected in the partitioning of the deformation and the kinematics of the faults. In this way, right-oblique subduction in the Eocene-Miocene (48-26 Ma) initiated or reactivated dextral sliding in the LOFS with a transtensional tectonic regime. After a phase in the Miocene with orthogonal convergence, due to the Farallon plate rupture, the subduction became oblique to the right again at 20Ma, which led to transpression

and dextral sliding in the LOFS (Cembrano et al. 2000; Rosenau et al. 2006; Cembrano et al. 1996).

2.2.2. Regional geology

In the eastern part of the SVZ, the Cenozoic basins accumulated between the Upper Paleocene and the Miocene-Pliocene, mainly fluvial deposits, with a marine intercalation during the Upper Oligocene-Lower Miocene. In the western part of SVZ, the characteristics of the Cenozoic basins (partly marine and metamorphosed), and the location of plutons Miocene, are associated with the activity of the Liquiñe-Ofqui Fault System. Additionally, the Main Cordillera is segmented into regions with distinct pre-Andean basement ages, Mesozoic and Cenozoic geologic evolution, crustal thickness, structural trends, active tectonics and volcanism. (Stern 2004).

The basement of the volcanic arc in NSVZ and TSVZ consists of sedimentary volcanic rocks (Melnick and Echtler 2006). While in CSVZ, between 38°-39.5°S, is described by a gradual transition from plutonic rocks to volcanic basal rocks. South of the 39.5°S, the Holocene volcanoes lie directly on plutonic basements of the North Patagonian Batholith (NPB) (Melnick and Echtler 2006). The NPB emplacement occurred episodically between the Cretaceous-Tertiary related to extensional tectonics. Three main plutonic events can be dated to the Cretaceous, the early Miocene and the late Miocene-Pliocene (Parada et al. 2007). Plutonic rocks are deposited on metasedimentary rocks, partially outcropping on the western margin of NPB (Herve et al. 2007). The eastern and western margins of the NPB show intrusive contacts with the underlying bedrock. The NPB locus of intrusion does not show temporal variations (Parada et al. 2007). LOFS runs within the central part of the NPB, often being the contact between different aged intrusive rocks. The fault zone is assumed to have controlled the spatial location of intrusive rocks since Mesozoic times (Hervé 1994). In the research area, the main outcrops of plutonic rocks can be found south of the Villarrica-Lanín volcanic chain (Moreno and Clavero 2006).

During the Eocene-Miocene extensional tectonic period (Pardo-Casas and Molnar 1987), a series of sedimentary formations occurred in the SVZ (Radic et al. 2002; Melnick et al. 2006). In the northern part of the SVZ, the basin deposits are formed by volcanoclastic and non-marine sedimentary rocks that reach thicknesses of up to 3000 m (Radic et al. 2002). These deposits

are known as the Cura-Mallin group and the Abanico formation (Charrier et al. 2002). The Cura-Mallin group overlaps with Jurassic sedimentary and volcanic rocks, as well as Cretaceous magmatic rocks. The group can be subdivided into two interdefined sub-series: the volcanic Guapitrio and the sedimentary Rio Pedregoso. The Guapitrio series contains lava deposits and volcanoclastic rocks, while the Rio Pedregoso formation consists of fluvial, lacustrine and deltaic sediments. During the Miocene, intra-arc basins, due to accelerated convergence and therefore compression, were inverted and elevated (Jordan et al. 2001). Between 33° and 41°S, the sedimentary volcanic deposits are within the current volcanic arc (Cembrano and Lara 2009) which gradually moves east towards positions within the posterior arc (Jordan et al. 2001).

In the study area, the metamorphic complexes of the Upper Paleozoic to Jurassic represent the accretion in the western margin of Gondwana, together with the rift Triassic sequences, and the Jurassic distal associations of the Neuquén basin associated to the Gastre System intrusive have been characterized (Moreno and Lara 2008). Over this basement is a Cretaceous magmatic arc, forming longitudinal plutonic strips with ages from the Lower Cretaceous (Maichin intrusive complex and Palguin granitoids) to the Upper Cretaceous (Reigolil and Caburgua granitoids). Over this plutonic basement, the Paleocene intra-arc basins (Estratos de Relicura) and a series of Oligocene-Miocene intra-arc basins (Cura-Mallin Formation) were developed. Contemporary with the development of the plutonic arc, the Pliocene volcanism is represented by the Curarrehue Formation (Moreno and Lara 2008). Over this relief, volcanic rocks were located, represented by the Malleco Formation in the Lower Pleistocene and the modern volcanic arc, with Pleistocene volcanic sequences, the actual stratovolcanoes and the Holocene monogenic eruptive centers.

2.3. Pucón/Villarrica area

The Villarrica volcano (39.5°S) is the outstanding volcano located at the northwestern end of the volcanic chain which also include the volcanoes: Cordillera El Mocho, Quetrupillán, Quinquilil and Lanín. Lanín, Quetrupillán and Villarrica volcanoes experienced eruptions during the Holocene, and Villarrica volcano is the only one with permanent fumarolic activity. The Villarrica-Lanín volcanic chain is northeast-southeast orientation, alignment N50°E (Lara and Clavero 2004), of 60 km in length. The volcanic chain, which

would represent a major fracture in the crust, is oblique to the quaternary volcanic arc of main orientation N10°E, associated with the Liquiñe-Ofqui Fault System (LOFS; e.g. López-Escobar et al. 1995; Cembrano et al. 1996; Moreno and Lara 2008). Along with the volcanic chain, five deeply eroded Pleistocene volcanoes together with more than 20 monogenetic cones and minor volcanic edifices (Figure 2.4) are remarkable volcanic centers in The Pucón/Villarica area. Related to both the inherited structural anisotropies and the current stress field (Lara 2004; Cembrano and Lara 2009).

Villarrica volcano is a Middle Pleistocene to Holocene eruptive center, ac-
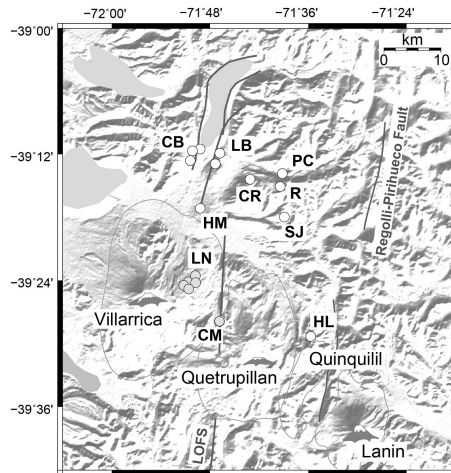
Figure 2.4.: Topographic map including location of the Villarrica-Lanín volcanic chain, in combination with the delimitation of the major volcanic edifies, and location of monogenetic cones (white circles) and minor volcanic eruptive center (gray circles). CB: Caburgua; CM: Cordillera El Mocho; CR: Cerro Redondo; LB: La Barda; LN: Los Nevados; HL: Huililco; HM: Huelemolles; PC: Pichares; R: Relicure; SJ: San Jorge (modified from Lara and Moreno 2004).

tive and characterized by an almost permanent lake of lava and persistent fumarolic activity in its crater(Lara 2004). During its evolution, it presents three characteristic eruptive periods. The last explosive event generating pyroclastic flows occurred ca. 530 years BP, with the generation of a small pyroclastic flow directed towards the north flank of the volcano. The historical activity of Villarrica volcano, however, has been essentially characterized by low explosive episodes, Hawaiian to Strombolian type (Moreno and Lara 2008). The first evolutionary unit whose age is estimated at 13,850 years BP (Moreno and Clavero 2006), is characterized by the composition of basaltic to

andesitic basaltic lavas, which built the caldera of the volcano. The collapse of this structure is recorded by outcrops on the eastern flank, which locally affected the Palguin valley. Unlike units 2 and 3, which are distributed mainly on the north and west flanks, the laharic are distributed on all flanks of the volcano. The second unit (age estimated between 13,850 and 3,700 years BP (Moreno and Clavero 2006)), is characterized by the presence of two deposits of pyroclastic flows such as the Lican and Pucón ignimbrites (Moreno and Clavero 2006) that cover large areas of land and also reflect a period of great explosiveness of the volcano. The third unit is made up of the eruptive products of recent years, which give shape to the current volcanic building and which have covered the area with pyroclastic deposits. The current cone was built on the northwestern edge of an elliptical caldera measuring 6.5×4.2 km (Lara 2004), formed in a larger, older building. The volcano is formed mainly by basaltic and andesitic-basaltic lavas and pyroclasts (Moreno and Clavero 2006).

To the southeast, the Quetrupillán is a compound stratovolcano that comprises a basaltic to dacitc rock-suite (Pavez 1997). It has an extensive postglacial explosive record, which includes pyroclastic flow and ash-fall deposits(Moreno et al. 1994). Its morphostructural features show a nested calderas and its magma chamber has collapsed as a result of a violent eruption. The crater of the Quetrupillán volcano is obstructed by a glacier.

The Lanín volcano, located at the southeastern end of the volcanic chain, is a compound stratocone, mainly effusive, comprised of four units defined through morphological criteria. The first unit represents an ancient volcano; the youngest three units form the present stratocone built since the Middle-Late Pleistocene. Compositionally, volcanic rocks from Lanín Volcano are mainly basalts/basaltic andesites and dacites with scarce intermediate types. Postglacial pyroclastic deposits are also silicic and confirm a sharp bimodality of the magmas (Lara et al. 2004).

Deeply eroded Plesitocene volcanoes such as Cordillera el Mocho, Quinquilil, Laguna Los Patos, Carilafquen and Pino Santo are located along the volcanic chain. The Cordillera El Mocho is an eroded and small stratocone located between Villarrica and Quetrupillán volcanoes (Figure 2.4). The Quinquilil volcano, placed northeast of the Quetrupillán volcano, is a prominent neck surrounded by basaltic lavas. The Laguna Los Patos and Carilafquen centers are gently dipping volcanic sequences cut by feeder dykes, both located between the Quetrupillán and Lanín volcanoes.

Due to the difference between the elaborated magmas of the stratovolcanoes of the volcanic chain and aggregated to the composition of primitive lavas of the monogenetic cones, from isotopic studies, the magma chambers below the stratovolcanoes are assumed at shallow depth (Hickey-Vargas et al. 1989). By contrast, the absence of main magma chambers below the small eruptive centers, indicates a short magma residence in the crust in relation to the reservoirs below the stratovolcanoes (Morgado et al. 2017). Furthermore, LOFS could facilitate a transport to the surface of the magmas of the monogenetic cones and also explain the differences observed with the eruptive conditions of the lava of Villarrica volcano (Morgado et al. 2015).

From a fluid dynamic point of view, a fault of seismic activity is not a necessary precondition for being the site of volcanism. A pressurized fluid can expand a sealed fault by inducing a displacement that drains the fluid through voltage drops. In a pre-fractured upper crust, ancient faults are the first-order geological boundaries and key points for fluid-driven dilation if they are compatible with the current stress field or if the pressures are supralithostatic (Lara 2004). The fault zones in the upper crust, composed of the fault core and the damage zone, are structurally anisotropic discontinuities. The fault core corresponds to the structural, lithological, and morphological portion of the fault zone in which most of the deformation is accommodated, including a simple slip surface, clay material, or highly hardened zones (Caine et al. 1996). The fault core can act as a conduit for fluid flow during deformation, and as a barrier when open pores are filled with precipitated minerals after deformation (Caine et al. 1996). Likewise, the damage zone or subsidiary structures that border the fault core increase permeability. Subsidiary structures in the fault zone include small faults, veins, fractures, cleavage, and folds that cause heterogeneities and anisotropy in the elastic and permeability properties in the fault zone. A wide damage zone could indicate multiple displacements and successive deformation processes (Caine et al. 1996).

The area is characterized by high hydrothermal activity. A significant number of intermediate temperature thermal sources (Sánchez et al. 2013; Held et al. 2018) are located mainly in valleys and mostly linked to fault systems associated with the volcanic chain. The thermal manifestations emerge through volcanic deposits, ashes and lapilli, which cover fluvial and alluvial deposits. These deposits cover Miocene granitoids (Moreno and Lara 2008). Depending on the characteristics of the thermal sources, structural domains associated with LOFS and ATF are observed (Sánchez et al. 2013). Thermal sources located along the ATF characteristics oriented to the W-NW generally have

a higher reservoir, but lower outlet temperatures. Conversely, as the LOFS implies the rapid ascent of magma (Cembrano and Lara 2009; Sánchez et al. 2013), the structural control of LOFS also is assumed as a pathway of a direct ascent to the surface of the hydrothermal fluids (Pérez-Flores et al. 2016; Held et al. 2018). Therefore, it is observed that the thermal waters under the structural control of LOFS increase with low temperature difference between the reservoir and the source, as well as with low dilution (Held et al. 2018; Nitschke et al. 2016).

2.4. Tolhuaca area

Tolhuaca volcano (38.32°S) is located at the northern end of the Liquiñe-Ofqui Fault System and is considered a dormant volcano due to there is no recent eruption recorded (Suárez and Emparan 1997). However, there is fumarolic activity emitted from the 600 m diameter secondary crater, located 1 km northwest of the main summit. Ten kilometers southeast of Tolhuaca is located the Lonquimay volcanic complex, which includes Lonquimay volcano, the Eastern Fisural Cordon and three minor eruptive centers that form a NE-SW alignment (Figure 2.5). Between Tolhuaca and Lonquimay, three minor Holocene pyroclast cones form a NE-SW alignment sub-parallel to the Eastern Fisural Cordon (Moreno and Gardeweg 1989) (Figure 2.5). The Lonquimay volcanic complex and Tolhuaca volcano and its geothermal system are expressions of the control of LOFS (Melosh et al. 2010; Pérez-Flores et al. 2016), due to LOFS turns towards east forming duplexes and horsetail geometries (Cembrano and Lara 2009; Rosenau et al. 2006) (Figure 2.5).

Tolhuaca volcano is a glacially scoured composite stratovolcano of late-Pleistocene to Holocene age that rises ~900 m over the basement (Lohmar et al. 2012a; Thiele et al. 1987). In the summit there are several NW-trending aligned craters with different degrees of preservation that indicate a migration of the volcanic activity from SE towards the NW (Thiele et al. 1987). The latest eruptive phases are at the NW extreme and correspond to a NW-trending fissure (~2 km long) and a pyroclastic cone. Lavas are predominantly basaltic-andesitic and andesitic, with minor presence of basalts and dacites (Thiele et al. 1987). In the surrounding area of Tolhuaca volcano, the basement of the Pleistocene-Holocene volcanic arc is Miocene volcano-sedimentary rocks (Figure 2.5, which have high intrinsic porosity and permeability and thus enhance the development of a hydrothermal reservoirs (Cembrano and Lara 2009). Plutonic rocks associated with the Miocene batholith are relatively
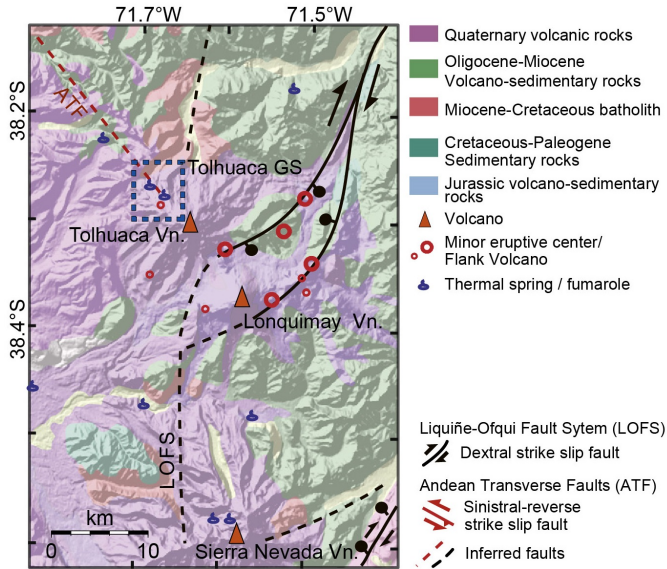
Figure 2.5.: Simplified geological map and major structural systems LOFS (black lines) and ATF (red dash line) and structural setting of the Tolhuaca geothermal system (modified from Sanchez-Alfaro et al. 2016).

impermeable unless highly fractured.

The Tolhuaca geothermal system is located on the northwest flank of Tolhuaca volcano and is characterized by several superficial thermal manifestations such as fumarole, solfatara, boiling pools, and hot springs (Figure 2.5). Geothermal exploration campaigns including surface mapping, fluid geochemistry analyses, resistivity (MT) measurements and borehole logging have revealed the existence of a high-enthalpy reservoir in the system (Melosh et al. 2012; Melosh et al. 2010). Two slim holes (Tol-1 and Tol-2) and two larger diameter wells (Tol-3 and Tol-4) were drilled down to 2117 m vertical depth. Of the two slim holes, rock cores were retrieved during drilling only from Tol-1; it is important to emphasize that this is the only available diamond drilled core material at Tolhuaca that can be used to undertake a detailed mineralogical analysis of veins and fractures. Temperature logging and fluid samples suggest the presence of a geothermal reservoir at ~1.5 km, at liquid-saturated conditions with temperatures up to 300°C and a strong meteoric water component (Melosh et al. 2012). The main reservoir

is overlain by a steam heated aquifer at shallow depths that reaches up to 160°C and controls the nature of most of the hot springs (Melosh et al. 2010; Melosh et al. 2012).

The Lonquimay volcanic complex (LVC) is a late-Pleistocene to Holocene age, and predominantly andesitic composition. LVC is comprised by Lonquimay volcano, a series of craters and pyroclast cones and lava flows, aligned in a NE-SW direction forming a 8 km chain called the Eastern Cordon Fisural (EFC; Moreno and Gardeweg 1989; Suárez and Emparan 1997) (Figure 2.5). Lonquimay volcano rises ~1000 m over the basement (Moreno and Gardeweg 1989). At its summit there is a main elliptical crater of 700 m diameter oriented WSW-ENE. On its northern edge there are three other secondary craters of 150-250 m diameter and on the WSW, one of 300 m in diameter (Moreno and Gardeweg 1989) and the last crater, Navidad cone and its lava flow, built in December 1988 (Moreno and Gardeweg 1989). The 1988 eruption is the last of five historical eruptions recorded (Naranjo et al. 2000). The explosive activity of Lonquimay has been frequent and relatively continuous during the Holocene (Polanco et al. 2014; Moreno et al. 2012).

3. Magnetotelluric method

The role of crustal fault systems in geothermal systems in volcanic areas necessarily implies a characterization of the different levels of the crust. Although geology provides valuable information, especially in cases where the effects of faults are observed on the surface, there are a large number of crustal fault systems that play an important role in geothermal systems in volcanic areas, which cannot be characterized entirely. Thus, electromagnetic methods help to solve this deficiency as they cover a wide range of depths. For this reason, the selection of appropriate geophysical techniques is highly dependent on the depth. Magnetotelluric method (MT) is suitable for exploring a wide range of depths, from hundreds of meters to hundreds of kilometers. Furthermore, MT is highly sensitive to the geoelectric response of geothermal fluids flowing through the fault systems by means of a conductivity contrast visualization.

3.1. Theoretical background

Magnetotelluric is a geophysical method that uses electromagnetic induction to investigate the electrical conductivity distribution of the Earth at deep underground. MT is a passive method that uses as a signal source the variations of the natural external electromagnetic field originated on various extraterrestrial processes, covering a wide spectrum of frequencies ranging from 10^4 to 10^{-5} Hz. Low frequency MT signals originated from the interaction of the solar wind with the magnetic field of the Earth. These low frequencies are generated when the solar wind emits currents of ions, which travel through the space and disturb the environment of the Earth's magnetic field. Whereas high-frequency MT signals ("atmospherics") originate from electrical discharges in the atmosphere, usually near the Equator. The signal produced by thunderstorm lightning travels in the waveguide formed by the conductive earth and the ionosphere; it can be observed over large distances due to relatively low attenuation along the propagation path. Between these

two natural signal sources, there is an energy gap around 1 Hz.

Theoretical bases of MT were introduced by Tikhonov 1950 and Cagniard 1953 with the objective of determining the vertical variations of the electrical conductivity distribution in the crust, as well as in the upper mantle of the Earth. In the 1960s it was shown that horizontal geoelectric inhomogeneities can be the cause of large distortions in MT survey results. Therefore, magnetotelluric needed a theory that considered the electromagnetic field within the Earth as horizontally inhomogeneous.

According to Faraday's law, time-varying causes an external variation on the magnetic field in the ionosphere, which induces an electric field inside the Earth. Additionally, this electric field induces a secondary internal magnetic field (Ampere's law). The induction process in a homogeneous isotropic medium is governed by Maxwell's equations and can be written as follows:

$$\nabla \times \vec{E} = -\frac{\partial \vec{B}}{\partial t} \tag{3.1}$$

$$\nabla \times \vec{H} = \vec{j}_f + \frac{\partial \vec{D}}{\partial t} \tag{3.2}$$

$$\nabla \cdot \vec{B} = 0 \tag{3.3}$$

$$\nabla \cdot \vec{D} = \eta_f \tag{3.4}$$

Where $\vec{E}$ is the electric field (V/m), $\vec{B}$ is the magnetic field (T), $\vec{H}$ is the magnetizing field(A/m), $\vec{j}_f$ the current density owing to free charges(A/m^2), $\vec{D}$ the electric displacement field (C/m^2) and η_f the electric charge density owing to free charges.

Assuming that time-varying displacements currents (arising from polarization effects) are negligible compared with time-varying conduction currents, Ampere's law (eq. 3.2) reduces to:

$$\nabla \times \vec{H} = \vec{j}_f \tag{3.5}$$

On the other hand, Maxwell's equations can also be related through their constitutive relationship:

$$\nabla \times \vec{J} = \sigma \vec{E} \tag{3.6}$$

$$\vec{D} = \epsilon \vec{E} \tag{3.7}$$

$$\vec{B} = \mu \vec{H} \tag{3.8}$$

Where σ, ϵ and μ describes the intrinsic properties of the materials through which the electromagnetic fields propagate. σ (S/m) is the electrical conductivity (its reciprocal is the electrical resistivity $\rho = 1/\sigma$ (Ωm), ϵ (F/m) is the electrical permittivity and μ (H/m) is the magnetic permeability. These magnitudes are scalar quantities in isotropic media. However, in anisotropic materials they must be expressed in a tensorial. It is necessary to emphasize that the properties of the materials are assumed to be isotropic.

Considering the equations 3.5, 3.6, 3.7 and 3.8, the Maxwell's equations can also be written as:

$$\nabla \times \vec{E} = -\frac{\partial \vec{B}}{\partial t} \tag{3.9}$$

$$\nabla \times \vec{B} = \mu_0 \sigma \vec{E} \tag{3.10}$$

$$\nabla \cdot \vec{B} = 0 \tag{3.11}$$

$$\nabla \cdot \vec{E} = \frac{\eta_f}{\epsilon} \tag{3.12}$$

Applying the following mathematical identities:

$$\nabla \times \nabla \times \vec{\varphi} = \nabla \left(\nabla \cdot \vec{\varphi} \right) - \nabla^2 \vec{\varphi} \tag{3.13}$$

Where $\vec{\varphi}$ is any vector. Taking the curl of equations 3.9 and 3.10 and including the fact that there cannot be accumulated free charges in a medium of uniform conductivity ($\sigma = 0$), i.e. $\nabla \cdot \vec{D} = 0$ and $\nabla \cdot \vec{E} = 0$, equations 3.9 and 3.10 can be expressed in term of the $\vec{E}$ and $\vec{B}$ by:

$$\nabla^2 \vec{E} = \mu_0 \sigma \frac{\partial \vec{E}}{\partial t} \tag{3.14}$$

$$\nabla^2 \vec{B} = \mu_0 \sigma \frac{\partial \vec{B}}{\partial t} \tag{3.15}$$

3.1.1. Plane wave

An important approximation assumption adopted is a plane wave, vertically incident on the conductive earth. Even if this assumption is violated, one can show that the incident wave is refracted vertically into the subsurface, also for angles close to $0°$. This assumption is based on the large distance to the source of these electromagnetic waves. Where the source is located in the outer space of the earth, i.e. the magnetosphere, and the observation point,

which is on the Earth's surface.

Assuming a plane wave with a surface amplitude E_0 and an harmonic time dependence of the form $e^{-i\omega t - qz}$, where ω is the angular frequency and q the wave number:

$$\vec{E} = E_0 e^{i\omega t - qz} \tag{3.16}$$

The right-hand side of Equation (3.14) can be evaluated to give:

$$\nabla^2 \vec{E} = i\omega\mu_0\sigma\vec{E} \tag{3.17}$$

Similarly for equation (3.15):

$$\nabla^2 \vec{B} = i\omega\mu_0\sigma\vec{B} \tag{3.18}$$

Equations (3.17) and (3.18) denote that MT measurements rely on a source of energy that diffuses through the Earth and is exponentially dissipated, as electromagnetic fields propagate diffusively.

Applying the second derivative in equation (3.16) as a function of depth (z):

$$\frac{\partial^2 \vec{E}}{\partial^2 z} = q^2 E_0 e^{i\omega t - qz} = q^2 \vec{E} \tag{3.19}$$

Matching equations (3.17) and (3.19) provide an expression for q:

$$q = \sqrt{i\mu_0\sigma\omega} = \sqrt{i}\sqrt{\mu_0\sigma\omega} = \frac{1+i}{\sqrt{2}}\sqrt{\mu_0\sigma\omega} = \sqrt{\frac{\mu_0\sigma\omega}{2}} + i\sqrt{\frac{\mu_0\sigma\omega}{2}} \tag{3.20}$$

And the inverse of the real part of q:

$$\delta\left(w\right) = \frac{1}{\Re\left[q\left(w\right)\right]} = \sqrt{\frac{2}{\mu_0\sigma\omega}} \tag{3.21}$$

Or

$$\delta(T) = \sqrt{\frac{T}{\pi\mu\bar{\sigma}}} \tag{3.22}$$

Where $\delta(T)$ is the electromagnetic *skin depth* in meters at a given period T, $\bar{\sigma}$ is the average conductivity of the medium penetrated, and μ is magnetic permeability. At a depth, $\delta(T)$, electromagnetic fields are attenuated to e^{-1} of their amplitudes at the surface of the Earth. This exponential decay of electromagnetic fields with increasing depth renders them insensitive to

conductivity structures lying deeper than $\delta(T)$. Hence, in MT studies, one electromagnetic skin depth is generally equated with the penetration depth of electromagnetic fields into the Earth. In studies of the Earth, μ is usually assigned the free-space value ($\mu_0 = 4\pi \times 10^{-7} Hm^{-1}$), and equation (3.22) can be approximated as:

$$\delta(T) \approx 500\sqrt{T\rho_a} \qquad (3.23)$$

Where ρ_a is *apparent resistivity*, or the average resistivity of an equivalent uniform *half-space*.

Depending on the target depth of interest in an MT study, the skin depth has implications for the frequency range needed to detect the target. Additionally, it has implications for inversion and numerical modeling problems, as boundary effects must be avoided. Electric fields are often forced to decay to zero at the boundaries of numerical models, which is non-physical, so the model mesh boundaries must be far enough away that the area of interest to be modeled is not affected by this non-physical electric field.

3.1.2. Impedance tensor

The electrical impedance Z is the ratio between the electric and magnetic field components, which comes from the matrix form relation: $\vec{E} = Z\vec{B}$. In a general 3-D earth, the impedance is expressed in matrix form using Cartesian coordinates (x, y horizontal and z positive downwards):

$$\begin{bmatrix} E_x \\ E_y \end{bmatrix} = \begin{bmatrix} Z_{xx} & Z_{yx} \\ Z_{xy} & Z_{yy} \end{bmatrix} \begin{bmatrix} B_x \\ B_y \end{bmatrix} \qquad (3.24)$$

Thus, each tensor element is $Z_{ij} = \dfrac{E_i}{B_j}$ and i, j represent x and y coordinates respectively.

3.1.2.1. Apparent resistivity

Electromagnetic waves that propagate through the Earth (linear, homogeneous and isotropic model) can be related by means of the impedance, which

is a characteristic measure of the electromagnetic properties of the subsurface and constitutes the basic MT response. Therefore, for a plane wave, the resistivity of the half-space is

$$\rho = \frac{T}{2\pi\mu} \|Z\|^2 \tag{3.25}$$

When the subsurface resistivity is not uniform, it corresponds to an average of the resistivities or an apparent resistivity. This apparent resistivity can be expressed as a function of the period and related to each component of Z. Replacing the values of *pi* and *mu* in equation 3.25, it can be rewritten as:

$$\rho_{a[ij]} = 0,2TZ_{ij} \tag{3.26}$$

3.1.2.2. Phase

The phase of the impedance tensor element, describes the phase shift between the electric and magnetic field components:

$$Z_{ij} = \left|\frac{E_i}{B_j}\right| e^{i\Phi_{ij}} \tag{3.27}$$

$$\Phi_{ij} = \phi E_i - \phi B_j \tag{3.28}$$

$$\Phi_{ij} = \arctan\left(\frac{\Im Z_{ij}}{\Re Z_{ij}}\right) \tag{3.29}$$

Where i, j = x, y and ϕE_i and ϕB_j are the phase of the electric and magnetic field components respectively.

3.1.3. Induction arrows

The so-called induction arrows (often termed induction "vectors") represent the ratio between vertical and horizontal components of the magnetic field (3.30). Vertical magnetic fields are generated by lateral conductivity gradients. Therefore, induction arrows can be used to infer lateral variations in conductivity.

$$B_z = \begin{pmatrix} W_x W_y \end{pmatrix} \begin{pmatrix} B_x \\ B_y \end{pmatrix} \tag{3.30}$$

$W = (W_x W_y)$ is also called tipper, as the secondary field has a lateral conductivity variation and is tilted out of the horizontal. Both T_x and T_y are complex

numbers. Therefore, real and imaginary parts of the equation 3.30 can be decomposed in two induction vectors:

$$\vec{P} = \Re\left(W_x\right)\vec{e}_x + \Re\left(W_y\right)\vec{e}_y \tag{3.31}$$

$$\vec{Q} = \Im\left(W_x\right)\vec{e}_x + \Im\left(W_y\right)\vec{e}_y \tag{3.32}$$

$\vec{e}_x$ y $\vec{e}_y$ are unit vectors. Graphical representation of the induction vectors is by means arrows. Additionally, is possible to estimate lateral changes in resistivity depending on their variations, directions, or size. There are two conventions for the graphical representation. In the Wiese convention, which is utilised in this work, the arrows point out of the conductive anomaly.

3.1.4. Phase tensor

The phase of a complex number is defined by the ratio between its real and imaginary part. This relationship has been represented as a tensor by Caldwell et al. 2004, where the phase is defined by:

$$\Phi = X^{-1}Y \tag{3.33}$$

X is the imaginary part, X^{-1} is the inverse of X and Φ is real. The phase tensor can be written as a function of the real and imaginary components of the impedance tensor Z, which in the Cartesian coordinate system is:

$$\Phi = \begin{bmatrix} \Phi_{xx} & \Phi_{xy} \\ \Phi_y x & \Phi_{yy} \end{bmatrix} \tag{3.34}$$

$$\Phi = \frac{1}{det\left(Z\right)} \begin{bmatrix} \Re Z_{yy}\Im Z_{xx} - \Re Z_{xy}\Im Z_{yx} & \Re Z_{yy}\Im Z_{xy} - \Re Z_{xy}\Im Z_{yy} \\ \Re Z_{xx}\Im Z_{yx} - \Re Z_{yx}\Im Z_{xx} & \Re Z_{xx}\Im Z_{yy} - \Re Z_{yx}\Im Z_{xy} \end{bmatrix} \tag{3.35}$$

Where $det(Z)$ is defined by:

$$det\left(Z\right) = \Re Z_{xx}\Re Z_{yy} - \Re Z_{xy}\Re Z_{yx} \tag{3.36}$$

To graph the phase tensor (Fig. 3.1), it is necessary to determine the following parameters:

$$\alpha = \frac{1}{2}\arctan\left(\frac{\Phi_{xy} + \Phi_{yx}}{\Phi_{xx} - \Phi_{yy}}\right) \tag{3.37}$$

α denotes the dependence of the tensor with the coordinate system and with the three invariant coordinates:

$$\beta = \frac{1}{2} \arctan\left(\frac{\Phi_{xy} - \Phi_{yx}}{\Phi_{xx} + \Phi_{yy}}\right) \tag{3.38}$$

β can be thought of as a rotation angle and refers to the asymmetry of the tensor. It should be noted that β depends on $(\Phi_{xy} - \Phi_{yx})$, which is invariant under rotation, but changes sign if the coordinate system is reflected.

$$\Phi_1 = \frac{\Phi_{xx} + \Phi_{yy}}{2} \tag{3.39}$$

$$\Phi_2 = \sqrt{\Phi_{xx}\Phi_{yy} - \Phi_{xy}\Phi_{yx}} \tag{3.40}$$

$$\Phi_3 = \frac{\Phi_{xy} - \Phi_{yx}}{2} \tag{3.41}$$

$$\Phi_{min} = \sqrt{\Phi_1^2 + \Phi_3^2} - \sqrt{\Phi_1^2 + \Phi_3^2 - \Phi_2^2} \tag{3.42}$$

$$\Phi_{max} = \sqrt{\Phi_1^2 + \Phi_3^2} + \sqrt{\Phi_1^2 + \Phi_3^2 - \Phi_2^2} \tag{3.43}$$

The phase tensor allows for knowing the dimensionality at a certain period. In a homogeneous semi-space (1-D case), the phase tensor will be a circle of radius 1. For the 2-D or close to 2-D case, β will be 0 or close to 0 respectively, and the phase tensor ellipse will have a major or minor semi-axis aligned with geoelectric strike. Furthermore, phase tensor allows the determination of gradients of resistivity given by the arc tangent function of Φ_{min} (3.42). When the angle is above 45°, Φ_{min} indicates the presence of a zone with conductive characteristics and when the angle is below 45° it indicates a resistivity characteristic.

3.2. MT data acquisition

In order to acquire MT data, it is necessary to measure the natural time-varying electric and magnetic fields at the surface of the Earth. These measurements are the vector sum of the primary source fields and the secondary fields induced in the Earth. Both the electric and magnetic fields are vector fields, therefore multiple components are measured. A schematic representation of MT site is shown in Figure 3.2.
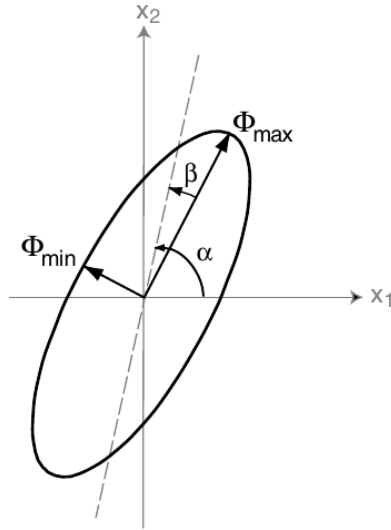
Figure 3.1.: Graphical representation of the phase tensor. Axes lengths of the ellipse are given by the main axes of the tensor. Direction of the main axis of the ellipse is defined by the relation $\alpha - \beta$. (Caldwell et al. 2004).
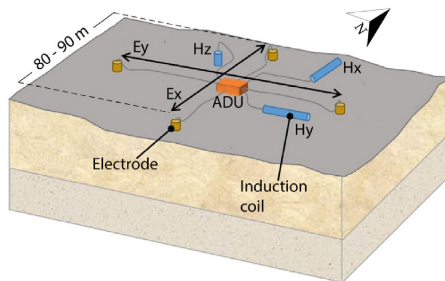
Figure 3.2.: Schematic figure of a MT setup in each station deployed in the study areas. Electrical field ($\vec{E}$) are measure with a four electrodes (orange) generally spaced 45 m respect with a data logger (red) in the center, forming two perpendicular pair of horizontal dipoles. Magnetic field ($\vec{H}$) are measure with three magnetic inductions coils. The horizontal induction coils (blues) measure the x and y component of the magnetic field, while the vertical induction coil (H_z) measures the z-component of the magnetic field. The incoming source wave is assumed to be a plane wave everywhere parallel to the Earth.

A given electric field component (e.g. the north-south component) is calculated by measuring the voltage between two buried, non-polarizing electrodes

separated by a default distance (e.g. 90 m) and forming a dipole (e.g. in the north-south direction). The electric field value is measured in volts per meter and voltages are usually in the order of milivolts. Electrodes are composed of an electrolyte mixture with a chemical composition that ensures stability over long time intervals with limited electrochemical interactions with the ground. Common electrode mixtures consist of lead-lead chloride ($Pb - PbCl_2$) or silver-silver chloride (Ag-AgCl) (Petiau 2000). Electrodes need good ground contact with low contact resistance to enable low-noise measurements. The vertical electric field is not measured in the MT method partly because there is an assumption that the vertical field approaches zero at the surface and also because it is impractical to construct a 90 m vertical dipole.

The magnetic field can be measured using two different sensors: an induction coil or a fluxgate magnetometer. Induction coils consist of many thousands of turns of copper wire wrapped around a core with a high magnetic permeability (e.g. iron). The more turns of copper wire, the higher the sensitivity of the coil to the rate of change (i.e. time derivative) of the magnetic field (Stanley and Tinkler 1983). As a trade-off, the more turns of copper wire, the heavier the coil. Because of this, practical induction coils are usually limited to periods <1000 s and are used primarily in broadband MT. An induction coil only measures one magnetic field component; therefore, three orthogonal induction coils are needed to measure the north-south, east-west and vertical magnetic field components. In contrast, flux-gate magnetometers are much more sensitive to long-period magnetic field variations (e.g. >1000 s) and usually measure all three field components simultaneously. A flux-gate magnetometer works by driving an alternating current through one coil of wire which is wrapped around a ring core of magnetically permeable material which undergoes magnetic saturation on each current cycle. For both induction coils and flux-gate magnetometer, the magnetic field is measured in nanotesla (nT).

Both the magnetic field and electric field data are recorded in a data acquisition system which includes an analog-to-digital converter. Usually, these converters sample the signal at variable rates depending on the frequency of interest, Nyquist aliasing considerations, and data storage.

The north-south and east-west electric and magnetic field components are measured simultaneously as well as the vertical magnetic field. Five different signals are continuously recorded over time, obtaining digital time-series that can be acquired simultaneously by different frequencies sampling. The

transfer functions are calculated by solving the linear expansion of equation 3.24:

$$E_x = Z_{xx}(\omega) B_x(\omega) + Z_{xy}(\omega) B_y(\omega) \qquad (3.44)$$

$$E_y = Z_{yx}(\omega) B_x(\omega) + Z_{yy}(\omega) B_y(\omega) \qquad (3.45)$$

Due to the plane wave source, field assumption is only an approximation, a statistical solution for the impedance is required. Then the remaining function $\delta Z(\omega)$ is minimized, assuming that the errors in the magnetic field measurements are negligible compared with the errors in the electrical field, the equations 3.44 and 3.45 can be written as:

$$E_x = Z_{xx}(\omega) B_x(\omega) + Z_{xy}(\omega) B_y(\omega) + \delta Z(\omega) \qquad (3.46)$$

$$E_y = Z_{yx}(\omega) B_x(\omega) + Z_{yy}(\omega) B_y(\omega) + \delta Z(\omega) \qquad (3.47)$$

3.3. MT data processing

Data processing consists of the conversion of the time-series domain in the frequency domain to calculate the transfer function. To accomplish this conversion, this work used a routine developed by Egbert and Booker 1986. This routine has been used for the robust estimation of geomagnetic transfer functions, which incorporates a robust automatic analysis scheme that iteratively reduces the weight of data that does not fit the Gaussian distributed variables of the model (M-estimated regression), producing reliable estimations of the transfer function with realistic errors. These are automated schemes that decrease the influence of outliers by repeatedly calculating the residuals $\mathbf{r} = \mathbf{e} - \mathbf{b} \cdot \mathbf{Z}$ and updating $\mathbf{Z}$ by removing window estimates which do not pass some criterion. These more statistically robust methods also have the advantage of producing more accurate estimates of error terms using the covariance matrix.

An additional way to minimize noise and biasing when computing tensor data using a robust method is to include electrical and magnetic field data from a remote site which was recording at the same time as the site processed. The remote reference technique, proposed by Gamble et al. 1979, minimizes the statistically residual error by correlation of the electromagnetic signal from the measurement site with a remote station installed several kilometers away from the measurement station. This signal is noise-free or generally low random noise and incoherent. Thereby, coherence is expected for the natural

electromagnetic field at least for a certain distance, while the noise of local origin will be incoherent between those two stations. The distance between the local site and the remote station is necessary to make the uncorrelated noise assumption, and depends on the noise source, the anticipated frequency range, and the conductivity of the medium. Due to the instruments being located several kilometers apart, simultaneous data recording is guaranteed by GPS devices. Thus, remote reference processing makes a cross spectra of magnetic and electrical field components from local and remote sites. Applying the estimations of the impedance tensor it is possible to obtain the apparent resistivity and phase curves, according to the given definitions in equations 3.26 and 3.29. Figure 3.3 exhibits the results between apparent resistivity and phases for the impedance tensor components obtained using a single site processing and remote reference processing.

Robust processing is usually able to remove most source field effects but
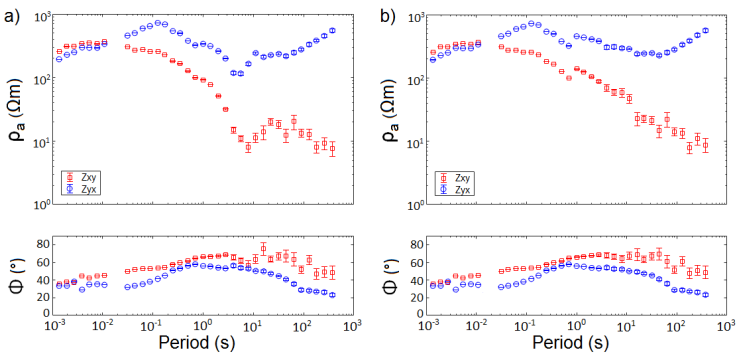
Figure 3.3.: Representative transfer function of MT station 24 in Villarrica survey using a) single site processing and b) remote referenced processing.

certain aspects may remain and lead to poor impedance estimates with significant scatter especially at long periods which have fewer time windows to stack. This is also significant when cultural noise sources which may be non-random and close to MT measurement locations (such as electric generating stations or DC train lines) (Szarka 1987) are present. Assessing the level of noise in an MT sounding and removing outliers is an important process to ensure high data quality.

3.4. 3-D MT inversion

The goal of MT explorations is to visualize subsurface structures in terms of the electrical resistivity as a function of position (e.g. $\rho(x,y,z)$). Therefore, from the measured data of the impedance tensor $(\vec{d})$ is generated a model $(\vec{m})$, which corresponds to the vector of model parameters known as the inverse geophysical problem:

$$\vec{m} = F^{-1}\left(\vec{d}\right) \qquad (3.48)$$

In the case of MT, the solution takes $\vec{d} = (Z_1, Z_2, \ldots, Z_N)$ and solves for $\vec{m} = (\rho_1, \rho_2, \ldots, \rho_M)$. In this notation, there are 2N independent data parameters (real and imaginary impedances) and M model parameters equal to the number of cell centers in a finite difference or finite element.

The inverse problem is non-unique, for a given data set there is an infinite set of models that can fit the data and non-linear:

$$F^{-1}\left(\vec{d}\right) = (m_1, m_2, m_3, \ldots) \qquad (3.49)$$

The non-linearity of the problem implies that there is no linear operator matrix that can be formed which multiplies the model vector to find the data vector. Non-linear problems are, in general, significantly more difficult to solve than linear problems, and most methods seek to linearize the problem prior to finding a solution.

The non-uniqueness solutions are due to the physics of the MT problem implying an inherent non-uniqueness between conductivity and volume. The most realistic MT inverse problems have l>n, and, as a consequence, there are more unknown model parameters than known data values and all real field data contains an error term, such that $\vec{m} = F^{-1}(\vec{d} + \vec{e})$ (Parker 1977). Therefore, the non-uniqueness of the inverse problem means that any model is only an approximation of the real Earth structure and the findings using this model must be considered carefully when choosing one that best represents the Earth.

There are different inversion methodologies used to determine the inverse problem. One methodology is based on Tikhonov regularization or damped least squares that seek to minimize data misfit by modeling smoothness, balanced by a user-defined regularization parameter:

$$S(\vec{m}, \tau) = (\vec{d} - F(\vec{m}))^T \vec{C}_d^{-1}(\vec{d} - F(\vec{m})) + \tau(\vec{m} - \vec{m}_0)^T \vec{C}_m^{-1}(\vec{m} - \mathbf{m}_0) \qquad (3.50)$$

Where S is the function to be minimized, $\mathbf{m}_0$ is an initial reference model, τ is the regularization parameter and $\| \|^2 = ()^T()$ denotes the L2, Euclidean norm. Here, $\vec{C}_d$ is the data covariance matrix (i.e. diagonal matrix containing data errors) and $\vec{C}_m$ is the model covariance (i.e. a matrix that enforces smoothness via derivatives or weights).

In this thesis, 3-D inversion models have been configured based on NLCG as a minimizer for the penalty function (Rodi and Mackie 2001; Kelbert et al. 2014). Thus, 3-D inversion of the MT data has been carried out by a modular system of computer codes for the inversion of electromagnetic geophysical data (ModEM) developed by Kelbert et al. 2014. The system is constructed with a fine level of modular granularity, sensitivity computations, inversion search algorithms, model parametrization and regularization, data functional-interchangeable, reusable and readily extensible (Kelbert et al. 2014; Egbert and Kelbert 2012; Meqbel and Ritter 2015).

ModEM is based on the approximation of Maxwell's equations on a step grid using a finite difference approximation. The discretized form of Maxwell's equations are solved for the electric field using iterative quasi-minimal residue (QMR) solutions. ModEM offers several procedures to minimize the governing penalty function in the inversion process, and its main advantage lies in the rapid development of inversion, which reduces CPU time and does not require a large memory size, allowing joint inversion of the impedance tensor together with the induction vector.

4. Visualizing preferential magmatic and geothermal fluid pathways via electric conductivity at Villarrica volcano, S-Chile

Abstract

Preferential fluid pathways along regional fault systems are crucial for the spatial localization of volcanic and geothermal manifestations. Differences in electric properties of fluids and hydrothermal alteration products against the unaltered matrix allow for visualization of such pathways. Unfavorable geometry for 2-D inversion resulting from the fluid pathways in regional faults often being aligned along the geo-electric strike can be overcome by using 3-D inversion of magnetotelluric data. For a section in the 1400 km long Liquiñe-Ofqui Fault System (LOFS), we demonstrate the potential of 3-D inversion of magnetotelluric data for visualization of fluid pathways. Six out of eight electric resistivity anomalies at intermediate depth are connected to volcanic or geothermal surface manifestations. Deep and highly conductive anomalies are detected in the vicinity of the volcanic chain and where the LOFS is cross-cut by a fault that belongs to the Andean transversal fault system. The anomaly related to the fault crossing reveals a vertical pathway extending to the surface. Phase tensor analysis indicate a structural origin of the latter anomaly that may be connected to a line of volcanic cones that occurs in the NE of Villarrica volcano.

4.1. Introduction

Preferential fluid pathways in subduction settings at different scales result e.g. in volcanoes, monogenetic cones and thermal springs. They cross-cut the crystalline basement which is typically characterized by low matrix porosity and permeability. Bulk porosity and permeability are mainly controlled by fracture network properties (Bense et al. 2013), which in turn depends on both the fracture network connectivity and the aperture distribution (Brown and Bruhn 1998). Near fault zones, the fracture density and connectivity tend to increases significantly and thus, bulk rock permeability near fault zones is generally larger than that of the protolith (Bense et al. 2013). Shearing and brecciation, common in faults within brittle crystalline rocks such us basalts, can increase of permeability by as much as five orders of magnitude (Walker et al. 2013). The aperture of fractures is also very sensitive to the pressure and stress conditions in the rock, which lead to more permeable fracture networks under favorably-oriented stress (Barton et al. 1995). Thus, the heterogeneous distribution of a fault's core and damage zone in crystalline and volcanic rock leads to tortuosity and preferential flow paths (Bense et al. 2013).

Worldwide, zones of low resistivity within continental fault systems have been attributed to the presence of fluids of different type (Unsworth et al. 1999; Unsworth and Bedrosian 2004a; Bedrosian et al. 2004; Cordell et al. 2019). In volcanic environments, low resistivity has been interpreted as a sign if either hydrothermal fluids, conduits, magmatic deposits, or a combination of these features (Bertrand et al. 2012; Hill et al. 2009; Díaz et al. 2015). In geothermal systems, low resistivity is associated with hydrothermal alteration, revealing either a cap layer in volcanic environment (e.g. Heise et al. 2008) or changes to fracture networks in non-volcanic systems (Geiermann and Schill 2010).

To visualize heterogeneities in the electric resistivity distribution along fault zones, one typically compares cross-sectional profiles across the fault zone by magnetotelluric technique (Jones and Groom 1993; Unsworth and Bedrosian 2004b). In contrast to earlier 2-D inversion of localized profiles, regional scale 3-D inversion of magnetotelluric data from the Lonquimay, Villarrica, and Llaima active volcanoes was able to reveal upper crustal conductors, interpretable as magma reservoirs (Kapinos et al. 2016).

The area extends from Villarrica volcano in the south to Pucón Lake in the north and runs along the Liquiñe-Ofqui Fault System (LOFS) intersected by

the WNW-ESE aligned pre-Andean Mocha Villarrica Fault Zone (MVFZ), belonging of Andean Transfers Fault (ATF) (Pérez-Flores et al. 2016). The fault zone is accompanied by the Villarrica-Quetrupillán-Lanín volcanic chain that trends N50°W (Lara 2004). Along this LOFS section, one finds both geothermal springs (Sánchez et al. 2013; Wrage et al. 2017; Held et al. 2018) and monogenetic cones (Cembrano et al. 1996). Anomalously high electric conductivities found in the lower crust (Brasse and Soyer 2001; Kapinos et al. 2016; Held et al. 2016) suggest a way to connect near-surface anomalies at the LOFS to their underlying roots.

Held et al. 2016 revealed substantial information about the geoelectric properties of the subsurface by means of two cross sections through the dominant geological structures. 2-D interpretation models based on the best geoelectric strike for all periods exhibits an NS trend (Brasse and Soyer 2001; Held et al. 2016), validating the execution of 2-D inversion in transversal profiles of the strike to visualize the predominant structures on the strike. However, variation between shallow, intermediate and deep levels, ranging from a NS to N30-40°E and NS strike respectively, requires a three-dimensional inversion to study the effects of secondary geological structures, mainly to overcome problems with the 2-D inversion along the geoelectric strike. The main objective of this study based on magnetotelluric data from Held et al. 2016 is clarify the 3-D effects generated by preferential fluid pathways in interaction areas between active cortical faults and volcanism surrounding the Villarrica area. In addition, provide a comparison of the results of electrical conductivity anomalies with the surface manifestations of the volcanic and geothermal system to conclude the potential origin of these anomalies.

4.2. Geological background

The volcanic and structural features of the study area are embedded in the compressive plate boundary system of the Southern Andes. Here, the subduction of the Nazca and Antarctic plates below the South American continental plate result in a system of parallel and oblique to the arc faults as well as a large number of active volcanoes. The study area is part of the Southern Volcanic Zone that includes regional faults, namely the Liquiñe-Ofqui Fault System (LOFS, López-Escobar et al. 1995) and a number of ATFs, which are associated with major volcanic eruption centers of Quaternary to recent age (Fig. 4.1a). In the northern part of LOFS, the regional stress field is characterized by a maximum sub-horizontal compressive regime trending in

N60°E direction (Lavenu and Cembrano 1999; Rosenau et al. 2006). Besides the volcanic systems, the study area is characterized by a large number of thermal springs (Fig. 4.1b). In the following, major structures and the thermal springs are detailed.

4.2.1. Liquiñe-Ofqui Fault System

Extending over > 1200 km, this prominent fault system runs parallel to the N-S oriented volcanic chain of the Southern Andes and is associated with a dextral transpressional regime (Cembrano et al. 1996; Cembrano et al. 2000). In the north, it reaches the Lonquimay-Tolhuaca volcanic complex, where it has been described as a "horsetail" that branches towards the east (Rosenau et al. 2006). A similar structure with bending the LOFS towards west is found at its southern rim in Patagonia. In its northern half, the LOFS is divided into two branches, of which the western on the dominant and structurally well-know. In this study, we neglect the eastern branch since it is at the rim of the study area. Moreover, the LOFS is offset during the reactivation of the ATFs.

Such an offset characterizes also the study area (Fig. 4.1b). Here, the LOFS north of the offset reveals two characteristic features. 1) It is split into two parallel branches running to east and west of Caburgua Lake. 2) Both branches are associated with groups of Holocene pyroclastic cones (Hickey-Vargas et al. 1989; Melnick et al. 2006) originating from different eruptive episodes and mostly of mafic composition (Lara et al. 2006b, Lara et al. 2006a). At the eastern branch, the monogentic cones follow the local N10°E trend of the LOFS (Cembrano et al. 1996), whereas at the western branch a N50°E alignment is observed (Lara et al. 2006b). Both groups reveal similar geochemical compositions. Single monogenetic cones further to the east differ partly or significantly from this signature (Hickey-Vargas et al. 2016; McGee et al. 2017) and occur in an area of high density of thermal springs.

In the southern part of the study area, the LOFS is characterized by one single fault plane. The outline of LOFS through the ATF (corresponding to MVFZ in Fig. 1) is a matter of discussion. In their regional studies Lara and Moreno 2004, Rosenau et al. 2006 and Melnick et al. 2006 indicate an interruption and offset of LOFS throughout this fault zone. Yet in a more detailed study, Sánchez et al. 2013 and Sernageomín 2010 do not find clear evidence for the offset of the fault zone and just describe it as an inferred fault in the area to

the north of the volcanic chain between Villarrica and Quetrupillán following the southern outline of LOFS.

4.2.2. Andean transverse fault

Kinematic condition along the LOFS result in NE and NW striking faults and volcanic alignments such as stratovolcanoes and monogenetic cones (Cembrano and Lara 2009; Melnick et al. 2006; Cembrano et al. 2002). The oblique-to-the-arc ATFs develop in NNW-WNW directions. The major ATFs, namely Bío-Bío Aluminé, Lanalhue, MVFZ, and Valdivia Fault Zones (Fig. 4.1a), are oriented in parallel to the minimum horizontal stress and undergo active compression (Lara et al. 2006b; Cembrano and Lara 2009). In this kinematic regime, the stratovolcanos along ATFs reveal an elaborated magmatic evolution and eruptive styles due to the long residence of magma in the upper crust (Lara et al. 2004). In contrast, NE-SW oriented fractures facilitate a rapid rise of magma (Lara et al. 2006b; Cembrano and Lara 2009). In the study area, such fault zones occur on the northeastern flank of Villarrica volcano (Cembrano and Lara 2009).

At Villarrica volcano, the ATF is represented by the MVFZ that crosses the crystalline basement and displaces the LOFS by a few kilometers indicating a sinistral movement (Lange et al. 2008). The MVFZ accompanies the N50°W alignment of the Middle Pleistocene to Holocene Villarrica-Cordillera El Mocho-Quetrupillán-Quinquilil-Lanín volcanic chain (Lara et al. 2004). Of these, the Villarrica, Quetrupillán and Lanín volcanoes have erupted during Holocene times. Villarrica volcano, with a basaltic to andesitic-basaltic composition, builds on the MVFZ (Moreno and Clavero 2006). This compressive tectonic situation, along with the overload exerted by the building of Villarrica volcano, is expected to hinder the rise of magma (Pinel and Jaupart 2000) and thus, facilitating the accumulation of magma in shallow reservoirs (Hickey-Vargas et al. 1989). Both the volcanoes of the Villarrica-Quetrupillán-Lanín volcanic chain and the monogenetic cones root deep down to the mantle-crust boundary. In contrast to Villarrica volcano, the monogenetic cones do not have a shallow magma chambers, probably due to the role of the LOFS as an efficient conduit for the rise of magma (Hickey-Vargas et al. 1989; Morgado et al. 2015).

Cembrano and Lara 2009 proposed volcanic-tectonics associations based on spatial distribution and overall morphology of individual volcanoes and

groups of volcanoes. Primarily controlled by the present-day compressional or dextral-transpressional tectonics of the volcanic arc, responsible for the geometry and kinematics of second-order structures such as tension cracks, shear factures and volcanic fissures. As is the case of Los Nevados complex, it corresponds to a set of pyroclastic cones and associated lavas located on the northeastern flank of Villarrica volcano (Moreno and Clavero 2006).

4.2.3. Hot springs

In the study area, there is a significant number of thermal sources of intermediate temperature (Sánchez et al. 2013; Held et al. 2018), which are topographically located in valleys and mostly linked to faults. The thermal sources located along W-NW oriented ATF features, generally present higher reservoir, but lower outflow temperatures, whereas the LOFS favors fast migration of magma and/or hydrothermal fluids (Pérez-Flores et al. 2016; Held et al. 2018). Thus, the thermal waters under the structural control of LOFS are observed to rise with little temperature difference between reservoir and the source as well as low dilution.

4.3. Magnetotelluric method

Magnetotelluric is a geophysical exploration technique belonging to the electromagnetic field allowing obtaining information on the geoelectrical properties of the subsurface by the temporal dependent fluctuations of the natural electric (**E**) and magnetic (**H**) fields. This technique has been extensively applied in studies of fault zones, volcanic and geothermal systems (Unsworth et al. 1999; Hill et al. 2009; Bertrand et al. 2012; Cordell et al. 2019).

31 magnetotelluric stations has been measured between November and December 2013. The stations have been deployed along two profiles in E-W and N-S direction with a mean inter-station distance of about 3 km between Caburgua Lake and Villarrica volcano (Figure 4.1b). Based on the quality of processing of these data, in this study, the entire data set was processed using a robust code based on Egbert and Booker 1986 including the 50 *Hz* filter. Remote referencing leads to significant improvement of transfer function quality in the low frequency range. More information of acquisition, processing and 2-D inversion of the magnetotelluric data are detailed in Held et al. 2016.
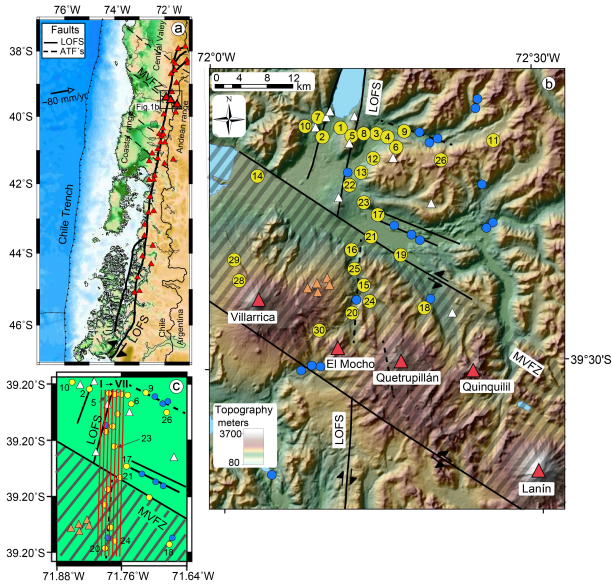
Figure 4.1.: a) Tectonic setting of the Southern Volcanic Zone including the Liquiñe-Ofqui Fault System (LOFS), the Andean Transverse Faults (ATFs) and the main volcanic edifices (modified from Cembrano and Lara 2009; Pérez-Flores et al. 2016; Somoza 1998). b) Topographic map of the study area including the LOFS and further fault zones (black lines), the Mocha-Villarrica Fault Zone (MVFZ, dashed area), monogenetic cones (white triangles), Los Nevados group (orange triangles), major volcanic buildings (red triangles), and thermal springs (blue dots) (modified from Sánchez et al. 2013 and Sernageomín 2010). Magnetotelluric sites are labeled with numbers in yellow dots. c) Seven N-S section across the LOFS.

Held et al. 2016 evaluated dimensionality by phase sensitive skew of impedance tensor after Bahr 1991. Results validate the assumption of 2-D distribution; however, there are period gaps with high skew (Held et al. 2016, Fig 4). In this area, the assumption would give unreliable results, particularly in sub-surface near to fault systems and/or hot springs manifestation.

In the presence of heterogeneities considered at the surface, the amplitude of the electric field seen can be distorted. The defined phase tensor seeks to recover the regional phase relationship of a set of distorted measurements, both for surface heterogeneity and for regional conductivity structures are 3-D (Caldwell et al. 2004). The phase tensor can be graphically represented by an ellipse with its main axes (Φ_{max} and Φ_{min}). Detailed explanation and analysis of the phase tensor is included in supplementary material. The main

resistance structures can identify before modeling by means of phase tensor ellipses, as seen in figure 4.2 with a pseudo section and greater geological features. In the uppermost section, short periods, the ellipses show high scattering in terms of elongation, orientation and mostly high β-angles point to 3-D structures. The change in direction of the principal axes of the phase tensor it is an indicator of a 3-D (regional) conductivity structure. Over long periods, the phase tensor ellipses are affected mainly E-W change in the depth resistivity distribution.
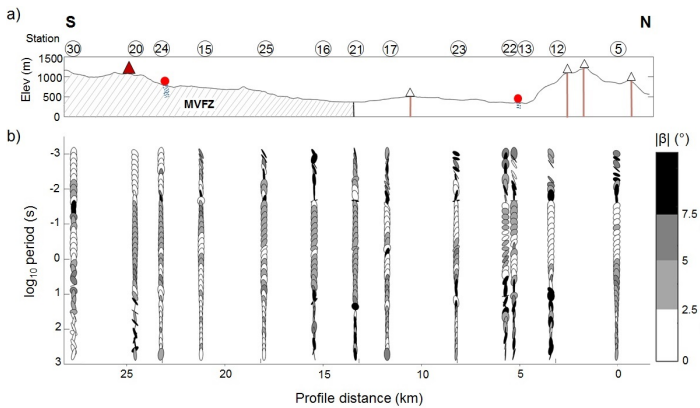
Figure 4.2.: a) Elevation and major geological features including MVFZ, the monogenetic cones and thermal springs across the N-S profile (Figure 4.1). b) Phase tensor ellipse with angle β.
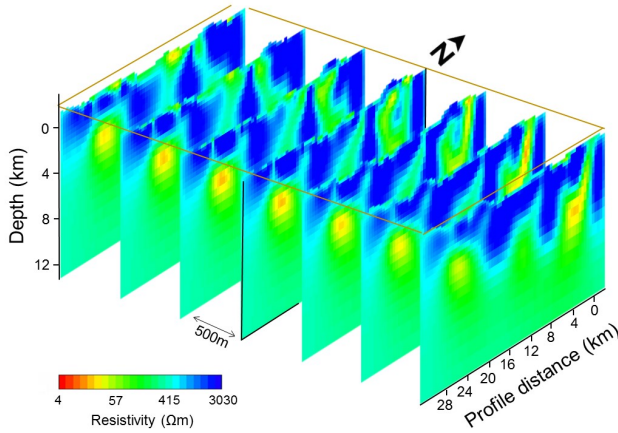
4.4. 3-D inversion

The 3-D inversion of the magnetotelluric data was carried out using the Modular System for Inversion of Electromagnetic Geophysical Data, ModEM developed by Kelbert et al. 2014. It includes forward modeling, sensitivity computations, inversion search algorithms, model parametrization and regularization, and data functionals (Kelbert et al. 2014; Egbert and Kelbert 2012). Its main advantage here is the fast convergence that finally allows for joint inversion of the impedance tensor together with the induction vector.

A subset of the data has been chosen to efficiently use the 3-D inversion program, calculated in 43 periods, logarithmically distributed between 0.0026 s and 512 s, with 7 periods per decade. All the elements of impedance tensor

Z and vertical magnetic component are relevant. In this study, we established a data error of 10% of $\left|Z_{xy}Z_{yx}\right|^{1/2}$ and 10% of $\left|T_yT_x\right|^{1/2}$, starting from a homogeneous half-space of 100 Ωm. The level of error was determined by the low data quality stations due to the presence of noise. A regular grid centered at the crossing of the E-W and N-S profiles was defined. The grid extends over 70 (E-W, positive towards the east) $\times$ 90 (N-S, positive towards the north) cells with a uniform size of 500 m $\times$ 500 m with 10 padding cells in each direction increasing gradually. To avoid lateral boundary effects, these padding cells with increasing size of the factor 1.3 were added. Topography was included using 50 m cells of linear increase up to 2000 m to continue with an increase factor of 1.1, allowing including topographic relief in whole region with a maximum elevation of 2847 m a.s.l. and minimum elevation of 243 m a.s.l. The increasing size in vertical direction sum up 89 layers. In total, the grid represents a volume of 70 km $\times$ 90 km $\times$ 89 km.

3-D inversion started from a homogeneous half-space of 100 Ωm. The best-fit model was achieved after 82 iterations with a normalized RMS error of 2.18. For examples of the data fit, see Figure S4.8 in the supporting information. The inversion results along the LOFS are presented in seven N-S profiles parallel to the LOFS (from its eastern branch in the north to the presumed outline through the MVFZ) with distances of 500 m to each other in Figure 4.3. The resistivity distribution along the LOFS is highly variable down to approximately 8 km depth. The near-surface is characterized by a resistivity ranging from a few Ωm to a few thousands Ωm that are distributed very locally. Below, a background resistivity of a few thousands Ωm extends down to about 4-5 km depth. This background is interrupted locally by low resistivity in the few Ωm to few tens or few hundreds Ωm range. In the northern part, some of these anomalies root rather deep. On the other hand, the prominent low resistivity anomaly in the south seems more root shallow. It reveals a resistivity minimum in the central profiles, whereas the northern low resistivity anomaly is most prominent in the eastern profiles. Below about 8 km, a resistivity of a 100 Ωm is prevalent. Comparable changes in electric resistivity have been attributed to the brittle-ductile transition zone (Bertrand et al. 2012) or changes in magnetic properties at the boundary between the upper and middle crust (Hernandez-Moreno et al. 2014).

Figure 4.3.: N-S cross-sections of the 3-D inversion of magnetotelluric data across the LOFS with an offset of 500 m to each other and including the majority of the measured MT stations (sections I-VII in Figure 4.1c).

4.5. Discussion

### 4.5.1. Influence of the main structures on dimensionality

Results of the 3-D model of resistivity distribution for the subsurface are consistent with main resistance features predicted before modeling by phase tensor analysis. As observed, high values of β angle, high dispersion in Φ_{max} orientation and elongated ellipses indicate three-dimensional effects in short periods. In the inversion model, the 3-D effects are observable up to 0.25 km $a.s.l.$ (Figure 4.4a). The 3-D effects would be ascribed to different Holocene volcanic stratigraphic layers belonging to several eruptive episodes of the Villarrica-Quetrupillán-Lanín volcanic chain.

At 0.4 km b.l.s. (Figure 4.4b) structures begin to be identified on a larger scale. MT sites deployed parallel to LOFS exhibit a trend of both low electrical resistivity and high electrical resistivity anomalies accommodated following the LOFS NS alignment, evidencing the presence of LOFS throughout the study area (Figure 4.1b). In turn, the difference in the electrical response would be related to the degree of damage to the fault. Greater fracturing favors the infiltration of hydrothermal fluids, decreasing the resistivity in the rocks. Implications of physical properties are discussed in next sections.

Enhanced of electrical response are mainly noticeable in the northern part of LOFS (Figure 4.4c), where the monogenetic cones are located. According to the spatial distribution and organization of individual volcanic buildings and cluster of volcanoes, the volcanic-tectonic association of LOFS would be evident.

From 2 km depth to 4 km, both fault systems would play a leading role. The lowest resistivity anomalies are related to N-S tectonic structures (LOFS) and partly NW-SE (MVFZ). We interpret this interaction as a favorable place for the development of highly fractured areas, facilitating the appearance of horizontal conductive anomalies. Below 4 km (Figure 4.4d), low resistivity anomalies would be highly influenced by active/inactive basement faults (ATFs).
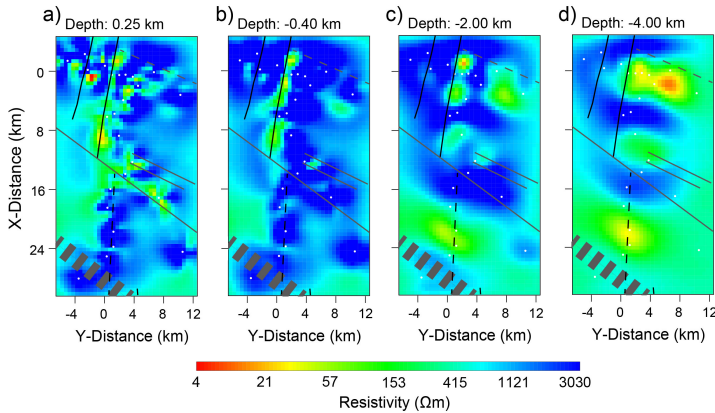
Figure 4.4.: Plan view 3-D Model results focused on the area with the highest density of stations shown 4 horizontal slices through the model at approximate depths of a) 0.25 km a.s.l., b) 0.40 km b.l.s., c) 2.00 km b.l.s., and d) 4.00 km b.l.s. Location of the MT stations are represented by white dots. Major fault traces of LOFS and ATFs are represented by black and gray lines, respectively.

4.5.2. 2- versus 3-D inversion results

For comparison with 2-D inversion (Held et al. 2016) and volcanic and geothermal manifestations, two representative cross-sections of the 3-D inversion results are presented in Figure 4.5 and 4.6.

Since the main geo-electric strike is parallel to the LOFS, the comparison

between 2-D and 3-D inversion is provided for the E-W section (Figure 4.5). The resistivity distribution obtained from 2-D inversion reveals a resistive environment down to about 7.5 km depth crosscut by an intermediate conductive anomaly at the LOFS (Figure 4.5a; Held et al. 2016). In the 3-D inversion, resistivity of this zone reaches lower values and its vertical extension to about 5 km is smaller. Its lateral resistivity variation reveals a higher dynamic. In contrast, to geological indications pointing to an about 2 km broad LOFS between the two boundary faults along each side of Caburgua Lake, the 2-D forward modeling of magnetotelluric data revealed a lateral extension of the LOFS about 0.25 km fixed to the eastern branch of the LOFS as best fit to the intermediate anomaly. The high-resolution image obtained in this study by 3-D inversion confirms this picture, but reveals a rather narrow branch rooting in the deep anomaly C1 at this eastern branch of LOFS (Figure 4.5b). In the section that is well-covered by magnetotelluric stations (between -8 and 8 km in Figure 4.5), our high resolution results reveal a number of low-resistivity anomalies (about < 20 Ωm, C_1 and C_2) as well as one of intermediate values (several hundreds of Ωm, R_1 and R_2). While the anomaly R_1 is roughly indicated and the anomaly C_2 occurs at deeper levels in the 2-D inversion. The anomaly C_3 is revealed by 3-D inversion, only. Due to the limited number of stations in this area, one must be careful in interpreting these anomalies. However, it would also occur at deeper levels in the 2-D inversion Anomaly C_3 would represent an overestimated anomaly of less resistivity than surrounding area located at shallow depth between stations 11 and 0 in Held et al. 2016 (Fig. 4.5a).

4.5.2.1. Why are important characteristics not evident in long period in 3-D inversion?

Discussed in the previous section, both the vertical extension of the resistivity distribution is less compared to 2-D inversion and the C_2 anomaly occurs at shallower levels. Sensitivity tests have been performed to verify the reliability of these features, adjusting different setup focused in main anomalies located below three km.

As shown in the supplementary material, replacing anomalies poor fit for intermediate and long periods obtained compared to the selected model. In the case of intermediate periods, the worst fit is directly related to the location of the modified features. For long periods, inversions are struggling to adjust some important features in absence of conductive anomalies (for example,
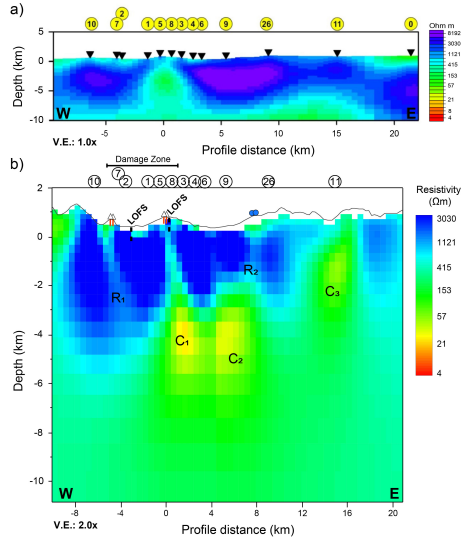
Figure 4.5.: E-W section of a) the 2-D inverted electric resistivity distribution along east-west profile modified from Held et al. 2016, and b) the 3-D inverted electric resistivity distribution of section VIII in Figure 4.1. High and intermediate conductivity anomalies are labeled with $C_1/C_2/C_3$ and R_1/R_2, respectively. Anomaly C_1 corresponds to the C_1 in Figure 4.6. Elevation (gray line) and major geological features including MVFZ, the monogenetic cones and thermal springs across the N-S profile (Figure 4.1) are included. In the top of each graph, MT stations (circles) of the profiles are shown.

Con2 in Held et al. 2016). Most distinguishable problem is in sites near to this feature. This behavior in 2-D inversion has also been observed. To solve this issue in 2-D inversion, the preferred model was obtained with error floor 70% for TE mode, which is predominant to detect conductive features. In our case, as the goal is on the features at medium to shallow depths, we set 10% error floor for both modes.

4.5.3. High-resolution resistivity distribution along the LOFS

Figure 4.6 displays the resistivity anomalies obtained from 3-D inversion along the section IV in Figure 4.1 and Figure 4.3 that is subparallel to the LOFS covering from north to south its eastern branch, several monogenetic cones, two thermal springs and reaching the MVFZ towards the El Mocho

volcano. In contrast to section VII, the magnetotelluric station coverage and data quality along the profile is rather homogeneous. Thus, resistivity anomalies along the section are equally reliable.

A low-resistivity anomaly extends from the surface to about 7 km depth in the northern part of the profile (C_1), revealing two branches towards the surface, a southern and a northern branch. While along section IV the northern branch appears to be dominant, towards the east in the sections VI and VII, the southern branch develops to the surface and reveals increasing electric conductivity (Figure 4.3). Highest electric conductivity in this section occurs in the southern part of the section towards the volcanic chain at a depth of about 3-4 km. Although intermediate resistivity values are observed throughout the entire model above this anomaly C_4, it appears to be rather connected from the surface (Los Nevados complex). Major intermediate resistivity anomalies crosscutting the resistive body down to about 4 km depth, R_4 and R_5, occur at the edges of C_4, while R_3, the anomaly with the highest conductivity seems to represent a more important structure.
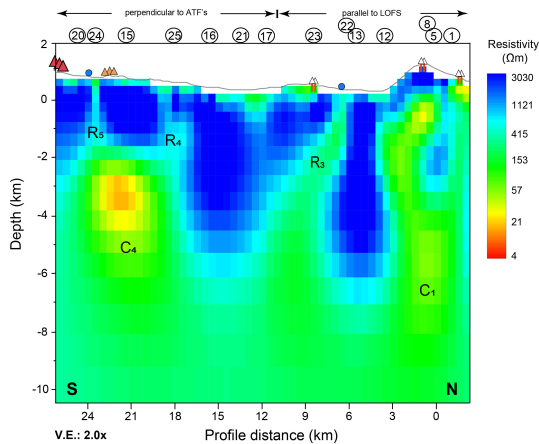
Figure 4.6.: N-S section subparallel to the LOFS in the study area of the 3-D inverted electrical resistivity distribution of section IV in Figure 4.1 and 4.3. This profile corresponds to the central profile in Figure 4.3. High and intermediated conductivity anomalies are labeled with C_1/C_4 and $R_3/R_4/R_5$, respectively. Anomaly C_1 corresponds to the C_1 in Figure 4.5. Elevation (gray line) and major geological features, the monogenetic cones and thermal springs across the N-S profile (Figure 4.1).

4.5.4. Comparison between geothermal and magmatic manifestations and resistivity

A summary of the observed anomalies in the representative cross sections (Figures 4.5b and 4.6) and their connection to volcanic and geothermal manifestations at the surface is provided in 4.1. It results that low-resistivity anomalies are typically occurring at depth >4 km. The anomaly C_1 coincides with the eastern branch of the LOFS and connects to the surface, where it reveals resistivity of a few hundreds of Ωm. Along its extension of about 5 km to the north, a number of monogenetic cones are observed at the surface. It should be mentioned that south of anomaly C_1, the representative profile deviates from the mapped surface outline of the LOFS.

Anomalies of intermediate resistivity are typically limited to depths <1 or <2 km. The anomaly R2 is an exception and links to a fault zone that is part of the ATFs and hosts thermal springs that reveal reservoir temperature that are among the highest in the area (120-140°C; Held et al. 2018). The anomalies R_3 and R_5 are linked to thermal springs of reservoir temperatures of about 100-110°C. The deeper-rooting intermediate resistivity anomalies R_1 and R_4 are not connected to a thermal springs. R_1 links monogenetic cones at the western branch of Caburgua Lake, the so-called Caburgua cluster with an age of about 8000-6000 yrs. (Moreno and Clavero 2006). Although a clear anomaly appears, no manifestations is observed at the surface linked to R_4. This anomaly develops into a near surface low-resistivity anomaly towards the west, where the easternmost volcanic cones of Villarrica volcano occur. Interestingly, this coincides with the change in orientation of the phase tensors from approximately N-S to about N30-40°E at the stations 25 and 16 and about N60°E further to the north at periods of about 1 s.

The origin of C_2 and C_4 is largely unknown. Kapinos et al. 2016 have suggested that this type of anomalies represent magma chambers.

4.5.5. Implications of the physical propierties

4.5.5.1. Porosity effects in resistivity response in faults

The effects of porosity in shear fault zones in the upper crust have been estimated using magnetotelluric in different parts of the world (Unsworth et al. 1999; Bedrosian et al. 2004; Becken et al. 2008; Yoshimura et al. 2009).

Table 4.1.: Summary of the range of extension in depth of the observed low (C) and intermediate (R) resistivity anomalies and the connected volcanic and geothermal manifestations at the surface from Figures 4.5 and 4.6.

Depth extension (km)	0 to 2	0 to >5	>2 to >5
Anomalies (connected surface manifestations)	R_1 (monogenetic cones, LOFS-western branch)	R_3 (thermal spring, monogenetic cone?)	C_2 (-)
	R_2 (thermal springs)		C_4 (Los Nevados complex?)
	R_4 (volcanic cones/MVFZ?)	C_1 (LOFS-eastern branch, monogenetic cones)	
	R_3 (thermal spring)		

Fault systems generate anomalies of lower resistivity than their environment, by fractures, increasing porosity and infiltrating hydrothermal fluids with salt content, improving the electrical properties of the rocks.

While Held et al. 2016 provides properties insights of LOFS, significant assumptions are required for fault zone parameters such as cementing factor, porosity, and clay content that are currently not well defined. Resistivity depends on the properties of the host rock and the content of fluids, since the dependence of the geoelectric response of the rocks on the crust is controlled by the ions contained in the water enclosed in pores. Therefore, the electrical response in rocks varies proportionally to the increase in porosity, temperature or molten fraction.

The role of the fluid in resistivity is determined by the amount of electrolytes that interconnect through the pores of the rock. Thus, a high percentage of porosity filled with saline fluids decreases the resistivity. Taking into account the characteristics of geothermal fluids in the Villarrica area (Nitschke et al. 2016); Saline fluid resistivity estimated at $\sim$10 Ωm and cementing factor between 1 to 1.3, quantifications for the C_1 anomaly on the LOFS by Archie's law (Archie 1942) reveal a required porosity range of 5-20%. This range is coherent with porosity values in shear fault zone, therefore the partial fraction option has been excluded for this characteristic, being consistent with the hypothesis that magmas would have migrated directly to the surface through LOFS from the deep reservoir (Morgado et al. 2015). Then, anomaly C_1 would represent the place where fluids accumulate in a large, damaged, high-porosity area produced by rock fracture at $\sim$4 km depth, from where fluid flows to the surface along the interface acting as a preferential medium temperature fluid exchange route. Furthermore, the location of the C_1 anomaly (Fig. 4.6) below the Caburgua monogenetic cones, would confirm the hypothesis that the eastern branch of LOFS facilitated the rise of magma

and reveals a vertical pathway extending to the surface.

R_1 anomaly, located below the group of monogenetic cones and in western branch, LOFS would also have functioned as a direct ascending conduit for magma. Here, we assume the same hydrothermal fluid fills the fractures, since it is part of the damage zone. Quantification for the R_1 anomaly reveal a porosity of less than 5%. Therefore, we infer that the western branch of LOFS is a more cohesive area with less content of hydrothermal fluids.

4.5.5.2. Implication of melt fraction in high conductivity features

Explaining high conductivity in anomaly C_4 presents greater complexity than the case previously analyzed for C_1. The absence of a main branch of LOFS makes the porosity analysis based on fracture parameters of this fault difficult. On the other hand, the presence of the group of young volcanic buildings, Los Nevados, suggests the presence of a certain amount of melt fraction, validated by the hypothesis of a shallow intermediate deposit for elaborate magmas belonging to the Villarrica volcanic chain (Morgado et al. 2015).

Taking into account the pyroclastic cones that compose Los Nevados group are oriented N60°E, this alignment would reflect fissures through magmas would have reached the surface (Moreno and Clavero 2006), we can estimate the porosity by Archie's law. Applying same assumptions for C_1, hydrothermal fluids and cementing factor range reveal a required porosity range of 20-60%. Range considered unreliable, due to geological considerations, therefore, the surrounding area of this anomaly would be discarded as a direct ascent pathways.

In order to characterize this high conductivuty structures their possible origin was estimate incorporing the melt fraction based on Archie's modified law (Glover et al. 2000). Taking into account melt fraction between 2-10% with a conductivity of 10 Sm^{-1} based on the range of electrical conductivity of the andesitic molten rock stablished by Tyburczy and Waff 1983, and the best porosity range scenario of 10-20% with cementation factor m = 1.3-1.6, we can explain a resistivity bulk of 15-20 Ωm. Therefore, the resistivity values obtained for the model with the best data fit, this conductive anomaly could be related to a remaining conduit or shallow reservoir of andesitic-basaltic composition.

4.5.6. Volcanic seismic background

Mora Stock 2015 detects a low seismic velocity zone located east of the main building of Villarrica volcano, where the group of volcanic cones of Los Nevados complex are located. This zone of low velocity matches in location and depth with the structure of low resistive anomaly (C_4) coincides with the second-order structures such as tension cracks, shear factures and volcanic fissures described by Cembrano and Lara 2009 Fig.6F. As we discussed in previous section, the feature C_4 would be interpreted as a remnant conduit/dike. Sensitivity data of C_4 has been evaluated by sensitivity test (Figure S4.9 in the support material) to delimit the possible magnitudes of this feature.

4.6. Conclusions

In this study, we demonstrate the potential of 3-D inversion of a magnetotelluric station network for detecting preferential fluid pathway along fault zones. Compared to earlier 2-D inversion, here, all anomalies of intermediate depth that are mostly of intermediate conductivity are traced up to the surface, where seven out of eight can be clearly linked to volcanic or geothermal surface manifestations. Phase tensor analysis indicate a structural origin of the high conductivity anomaly that may be connected to a line of volcanic cones that occurs in the NE of Villarrica volcano.

Deep and highly conductive anomalies are detected in the vicinity of the volcanic chain and the crossing of major faults, in our case LOFS and a fault that belongs to the ATF system. The connection to the surface is very clear for the fault-related system, where crossing of two damage zones may provide optimal vertical pathways. The link between the volcanic chain and the deep anomaly in the south of the study zone is less evident. For further clarification, an extension of the high-resolution data set towards Villarrica volcano would be necessary.

Our results have major implications for the understanding of the subsurface of Villarrica volcano, of which little is known. More important, the results of the 3-D inversion of high-resolution magnetotelluric data reveal great potential for geothermal exploration. The link between electric conductivity and thermal springs reveals images and depth of the respective hydrothermal reservoir.

Acknowledgements

Supplementary Material

Magnetotelluric analysis – Induction arrows

The Induction arrows represent the ratio between the vertical and horizontal components of the magnetic field (real and imaginary part); it is generated by lateral conductivity gradients. Therefore, the induction arrows are used to infer the occurrence of lateral variation in conductivity. According Wiese convention (Wiese 1962), induction arrows point away from relatively high conductive features. The orientation of the induction arrows change at
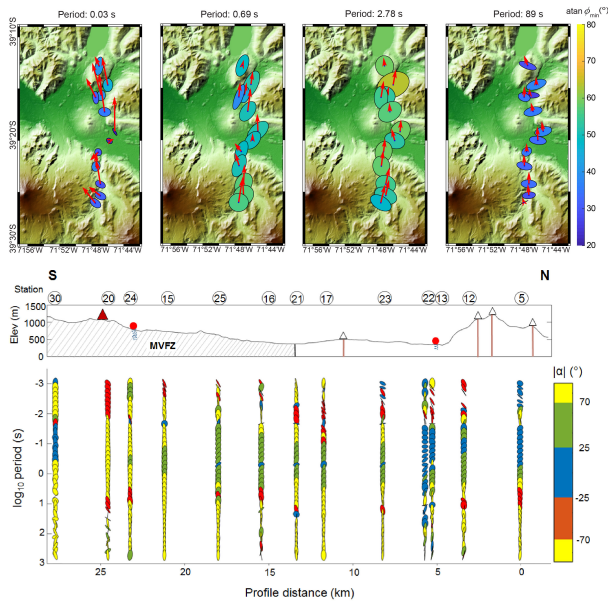
Figure 4.7.: Top, graphical representation of Phase tensor ellipses and induction arrows (Wiese convention) for periods of (a) 0.03 s, (b) 0.69 s, (c) 2.78 s, and (d) 89 s. Middle, Elevation and major geological features including MVFZ, the monogenetic cones and thermal springs across the N-S profile. Bottom, Phase tensor ellipses filled with angle α across the N-S profile.

periods of 0.03 s (Figure S4.7a) indicates a variation of lateral conductivity across the N-S direction, clearly indicator of three-dimensional regional structures analysis deduced from the ellipses of the phase tensor for depths near subsurface. In figure S4.7 top for depths attributed to periods greater than 2 s the structures reveals 2D behavior in general.

Data fit

Sensitivity test
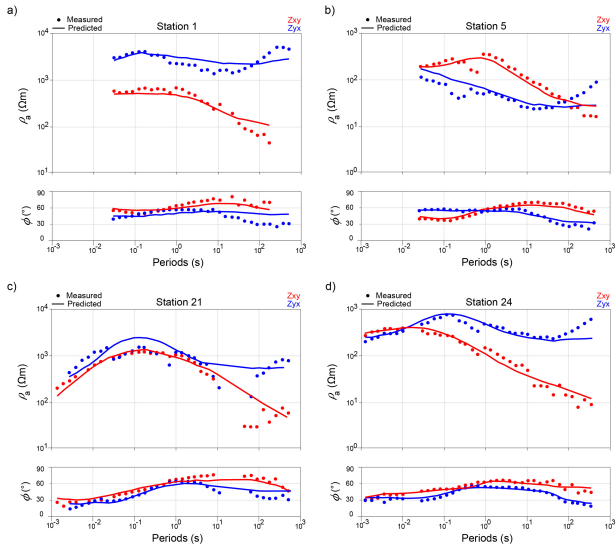
Figure 4.8.: Data-fit examples. a), b) y c) stations belonging to profile N-S.
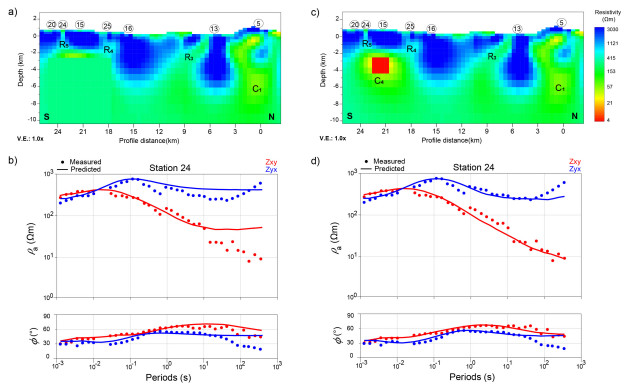
Figure 4.9.: Sensitivity test to determine the size of the conductor C4. a) Resistivity block (100 Ωm) is inserted instead of the Los Nevados Complex anomaly. c) Conductive block (1 Ωm) is inserted instead of the Los Nevados Complex anomaly. The forward responses for resistivity and conductivity block were calculated and compared with final model responses shown in b) and d), respectively. Based on the test, the depth of the anomaly that would represent magma chambers of Los Nevados Complex ranges between ~2 and 5 km.

5. Magma storage and transfer in the Villarrica volcanic chain, South Chile: MT insights into volcano-tectonic interactions.

Abstract

The active magmatic arc of the Andes is controlled by subduction of the Nazca and Antarctic Plates beneath the South American Plate. The Southern Volcanic Zone is the segment with the most active volcanoes in the Andes and one where volcano-tectonics are more evident. Magmatic fluids are channeled through the brittle crust by faults and fractures, becoming an important region for understanding the mechanisms associated with melt migration and storage in subduction zones. The Liquiñe-Ofqui Fault System and the Andean Transverse Fault, controll the overall architecture of the volcanic arcand play an important role on magmatictransport and compositional partitioning. Evidence of this is the oblique volcanic chain composed of Villarrica, Quetrupillán and Lanín stratovolcanoes, and a number of minor eruptive centers, where a wide range of magma compositions have been erupted with basalts and basaltic andesites dominating the suite. We used long-period and broad-band magnetotelluric stations deployed surrounding of Villarrica volcano to investigate the implications of crustal faulting and volcanism and their consequence on crustal reservoirs. Inversion of the data was used to generate three-dimensional electrical resistivity models. The resistivity distribution shows the upper crust as highly resistive, but below and east of Villarrica volcano, the model suggests the presence of a magmatic reservoir at shallow crustal levels (between 1.5 and 3 km b.s.l.), possibly corresponding to a transient magma storage. Meanwhile, the middle crust

contains several intermediate to low conductive features interpreted as fluid pathways and/or melt storage, respectively, revealing the important role of fault systems. The lower crust also contains low resistivity zones indicating the presence of partial melt and/or fluids, associated with deep reservoirs (8-20 km), with a significant proportion of them likely non eruptible parts. This would suggest that melt is accumulated as highly crystallized mush or disconnected melt pockets and highlight the complex vertical extent of the structurally-controlled plumbing systems even in thin crust settings.

5.1. Introduction

The Andean margin is controlled by the subduction of the oceanic Nazca and Antarctic oceanic plates beneath the continental South American Plate in the past ~200 m.y. (Kendrick et al. 2003). Volcanism in the main Andean Cordillera occurs in four separate volcanic regions. The region with the highest number of active volcanoes corresponds to the Southern Volcanic Zone (SVZ) (33-46°S) that includes >50 active volcanic edifices in Chile and Argentina, as well as three giant silica caldera systems and numerous minor eruptive centers (Stern 2004). Among the larger, active, and known volcanic complex in the SVZ are Planchón-Peteróa, Laguna del Maule, Nevados de Chillán, Copahue-Caviahue, Lonquimay, Llaima, Villarrica, Puyehue-Cordón Caulle, Osorno and Calbuco. All of them with eruptions in the last fifteen years with the only exception of Laguna del Maule.

The SVZ, is a key region for understanding the mechanisms associated with fluid/melt migration through the lithosphere in subduction zones. Primary melts in the SVZ are generated by flux melting of the subarc mantle wedge triggered by the dehydratation of the subducted Nazca (Stern 2004). In general, a small fraction (estimated in the range of 5-20%) of the primitive melt erupts at the surface with the rest cooling in the crust or upper mantle (White et al. 2019). Thin crust settings as Southern Andes (Ramos et al. 2014) are thought to be zones of more direct ascent from the mantle, with little or no interaction with lithosphere (Cembrano and Lara 2009). Thick crust settings are in turn able to form vertically extensive plumbing systems (e.g., Annen et al. 2015). Often interacting with the crust on their passage to the surface the melts generate a feeding zone for magmatic bodies at different crustal levels where magmas may reside in melt lenses or magma chambers for long periods, before erupting or definitively freezing. In the upper crust, magmatic fluids may circulate and ascend through the fault/fracture network,

especially enhanced by lithospheric-scale fault systems (Cembrano et al. 2000) and are usually stored beneath active volcanoes, at depths of a few kilometers below the surface. These processes lead to a considerable increase in electrical conductivity at different levels of the crust, forming ideal targets to be identified by geophysical methods, such as magnetotelluric.

Magnetoteluric (MT) method has been widely used to characterize active magmatic arcs in various convergent zones (Díaz et al. 2012; Araya Vargas et al. 2019; Bedrosian et al. 2018; Hill et al. 2015). MT method allows mapping the electrical resistivity of the subsurface using natural electromagnetic signals (Chave and Jones 2012). Electrical resistivity of dry crystalline rocks may have high resistivity, while saline liquids or molten rock zones may have low resistivity or their inverse high conductivity. This large variation offers the possibility of elaborating well-defined models of the electrical conductivity structure of the Earth. Therefore, MT method is useful for investigating the distribution of fluids and melts in the subsurface and has the potential to show magma batches moving throughout the lithosphere, including the first-order conduits responsible for feeding active volcanism.

In the SVZ, specifically at the Villarrica volcano, long-period (Brasse and Soyer 2001; Brasse et al. 2009; Kapinos et al. 2016) and broad-band (Held et al. 2016; Pavez et al. 2020) magnetotelluric studies have resolved some characteristics of the structure underneath the edifice. However, details and structure of the magma storage regions, and the pathways between those zones and the overlaying volcanoes are still scarce. The latter hinder the ability to image the architecture of the plumbing systems, which even in thin crust settings may be more complex than previously expected.

To better resolve the conductors and distinguish between shallow conduits and deeper magma reservoirs in the surrounding area of Villarrica volcano, 3-D inversion of the MT data sets acquired at about 39°S over the past decades was carried out. This study reveals detailed images of crustal resistivity and additional evidence on magmatic fluids in the lower crust and their storage in upper crustal levels depicting vertically extensive plumbing systems.

5.2. The study area in the Southern Volcanic Zone

Permanent deformation of the crust in the SVZ is mostly focused on two groups of faults, as shown in 5.1a. The first group corresponds to the Liquiñe-Ofqui Fault System (LOFS), an active transpressional system composed of NNE trending master faults with dextral displacement accompanied by compatible normal faults roughly oriented from NE to ENE (Lange et al. 2008; Lavenu and Cembrano 1999; Cembrano and Lara 2009; Rosenau et al. 2006; Pérez-Flores et al. 2016). Geological evidence indicates that LOFS is a long-lived continental-scale shear zone that partially accommodates the margin parallel component of the oblique plate convergence. The second family of faults corresponds to the Andean Transverse Faults (ATF; Pérez-Flores et al. 2016), a group of NW-trending sinistral and inverse sinistral faults oblique to the current orogen that are apparently inherited from basement structures (Melnick and Echtler 2006; Cembrano and Lara 2009; Pérez-Flores et al. 2016). The latter are thought to be related to the tectonic segmentation of the Andes (Figure 5.1a) (Cembrano et al. 1996; Cembrano et al. 2002; Melnick et al. 2006). For instance, Lanalhue Fault marks the contact between two distinct units of continental basement (Melnick et al. 2006).

The study area is located at the northern segment of the LOFS intersected by the NW-trending Mocha Villarrica Fault Zone (MVFZ), which has controlled the active Pleistocene-Quaternary volcanism, a forearc structure that becomes an alignment of active Pleistocene-Quaternary stratovolcanoes belonging to the Villarrica-Quetrupillán-Lanín volcanic chain (VVC) (Moreno and Clavero 2006; Lara 2004; Lara et al. 2006b) (Figure 5.1b). Further east, the Reigolil-Pirihueico Fault (RPF) is a second-order fault parallel to the LOFS forming also both a geological discontiniity and a norphological feature that separetes a basament that is highger eastwards (Lara 2004). Lanín volcano is placed on this uplifted block (Lara et al. 2004). In addition, a significant number of minor basaltic erupted centers appear spatially associated to the LOFS (Cembrano and Lara 2009; Moreno and Clavero 2006; Morgado et al. 2015) while some partially eroded Pleistocene volcanoes as was the case in the for the oblique volcanic chain (Moreno and Clavero 2006) (Figure 5.1b).

Villarrica volcano is a Middle Pleistocene to Holocene edifice (Moreno et al. 1994) formed by the emission of mostly basaltic to basaltic-andesitic lavas, generating elliptical calderas (Moreno and Clavero 2006). Caldera 1 was
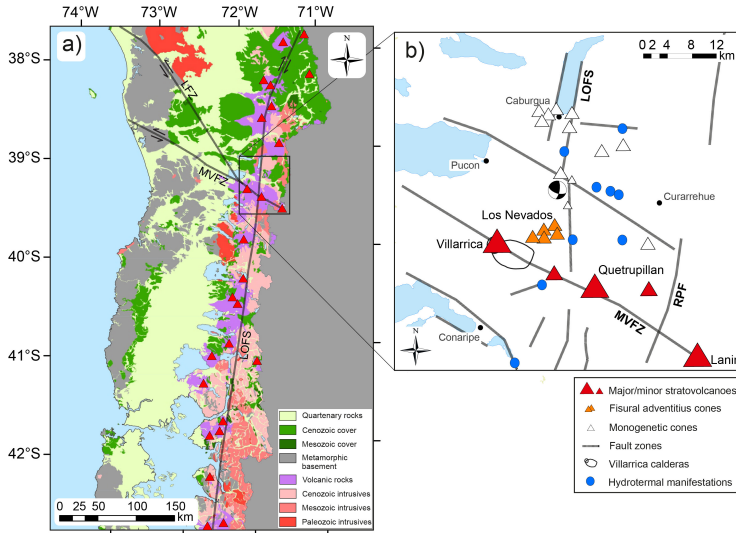
Figure 5.1.: a) Regional geological and tectonic map of the Southern Volcanic Zone. It includes the Liquiñe-Ofqui Fault System (LOFS), the Andean Transverse Faults (ATF) and the major stratovolcanoes (modified from Cembrano and Lara 2009; Pérez-Flores et al. 2016; Sernageomín 2010). b) Schematic map of the study area including NS faults (LOFS and Reigolil-Pirihueico fault (RPF)) and NW faults (MVFZ). Major volcanoes of the Villarrica-Quetrupillán-Lanín volcanic chain (red triangles) and minor volcanoes by monogenetic cones (white triangles) and Los Nevados complex (orange triangles) are displayed. Blue dots represent thermal springs.

formed about 100 ka by a collapse. A second collapse, embedded in the previous one, occurred about 14 ka (Caldera 2), creating a series of pyroclastic flows. The current cone has been built and continues to be built on the northwestern edge of calderas 1 and 2, within caldera 3, through a succession of effusive and explosive eruptions. Lately, the activity of Villarrica volcano has been essentially characterized by low explosive episodes (Hawaiian to Strombolian), occurring inside the crater of a small and permanent lava lake, of variable depth, with continuous fumarole activity (Moreno and Clavero 2006; Lara 2004).

Los Nevados Complex (LNC) is a set of pyroclastic cones and andesitic-basaltic lavas (Holocene) on the northeastern flank of the Villarrica volcano, northeast of the edge of Caldera 1, aligned in an N60°E orientation (Moreno and Clavero 2006).

Quetrupillán Volcanic Complex corresponds to a stratovolcano built on a

caldera and a series of minor centers aligned on on the flanks (Simmons et al. 2020). In contrast with the neighbors, Quetrupillán mostly erupted trachytes during the Holocene (Brahm et al. 2018) while Lanín is formed by a wide range of products where basalts predominate (Lara et al. 2004).

5.3. Magnetotelluric method

Magnetotellurics (MT) is a passive method that uses the natural fluctuations of the Earth's external magnetic field and electromagnetic induction to obtain the distribution of the Earth's electrical conductivity. Broadband MT data (period range: $10^{-3} - 10^3$ s) is able to image crustal features of km and tenths of km. Long periods MT data (period range: $10^0 - 10^5$ s) is able to image crustal and lithospheric structures.

5.3.1. Previous MT studies in SVZ (39-40°S)

The first magnetotelluric deep soundings in south of Chile were carried out around Villarrica volcano by Muñoz et al. 1990, who detected a conductive layer at 35-50 km depth. Brasse and Soyer 2001, inverting data along three transects near the 39th parallel, unveiled zones of high conductivity below the active volcanic arc. Subsequently, Brasse et al. 2009 provide 2D models with evidence for structurally anisotropic, deeply fractured and fluid-rich lower crust that can explain the unique pattern of uniformly deflected long-period induction vectors derived from geomagnetic transfer functions. The geomagnetic transfer functions, usually plotted as induction vectors, are indicative of lateral conductivity distribution. Furthermore, and based on long-period MT soundings, Kapinos et al. 2016 confirmed conductivity anomalies in previous 2-D models by new 3-D inversion models. The 3-D models of the Villarrica-Quetrupillán-Lanín volcanic chain show a conductivity anomaly below the magmatic arc that might correspond to a magmatic reservoir in the crust displaced to the east of the arc front at Villarrica volcano (Kapinos et al. 2016). Held et al. 2016 found a connection of the mid-crustal conductor with the transversal fault zones in the area. More recently, Pavez et al. 2020 provided additional evidence of deep and highly conductive anomalies detected in the vicinity of the volcanic chain, where the LOFS seems to be segmented by the oblique fault systems.

5.3.2. MT data sets

The Villarrica volcanic chain has been explored by MT campaigns conducted in 2000, 2005 and 2016 (Brasse and Soyer 2001; Kapinos et al. 2016; Held et al. 2016). The data set used in this study consists of long-period MT data with a period range of $10^0 to 10^5$ s and a broadband data set with a period range of $10^{-3} to 10^3$ s. Sampling sites are displayed in Figure 5.2 with different colors according to the year of acquisition.

The 2000-05 data set provided by Kapinos et al. 2016 is composed by 17 long-period MT data deployed in a long E-W profile (Figure 5.2a). The minimum distance between 2 neighboring sites is 6 km (sites cvo-vin) and the average distance in the Villarrica volcanic chain is ~11 km. The 2013 data set is composed by 31 broadband MT data deployed along two profiles in E-W (Caburgua Lake) and N-S direction (between Caburgua Lake and Villarrica Volcano) Pavez et al. 2020 (Figure 5.2b). For the latter, the minimum distance between 2 neighboring sites is 1.5 km (sites E01-E05) and the average distance is 1.8 km.

5.3.2.1. Three dimensional MT inversion

In order to obtain a high-resolution 3-D image of the conductivity distribution below Villarrica and to be able to interpret it in relation to magmatic structures in the crust, we performed an inversion of broadband and long-period magnetotelluric data using the 3-D inversion code ModEM (Egbert and Kelbert 2012; Kelbert et al. 2014; Meqbel and Ritter 2015; Meqbel 2009).

For the 3-D inversion, we selected high-quality, low-noise data from 9 MT sites from 2000 to 2005 campaigns and 23 MT sites from 2013 and thus obtained a network of 32 regularly spaced stations with a minimum distance between sites of 1.5 km (sites E01-E05) and an average distance of 3.6 km (Figure 5.2b). The final data set addressed by the inversion was composed of the 32 sites (Figure 5.2b). Data in a period range between $10^{-2} - 10^4$ s was used, resampled into 45 values. The error floors were set of 8% for the full impedance components and 5% was set for the geomagnetic transfer function. The resampling was calculated using 3-D Grid Academic software (Meqbel, personal communication).

The full impedance tensor and the geomagnetic tensor were inverted invoking a grid of $65 \times 105 \times 93$ cells in lateral and vertical directions respectively,
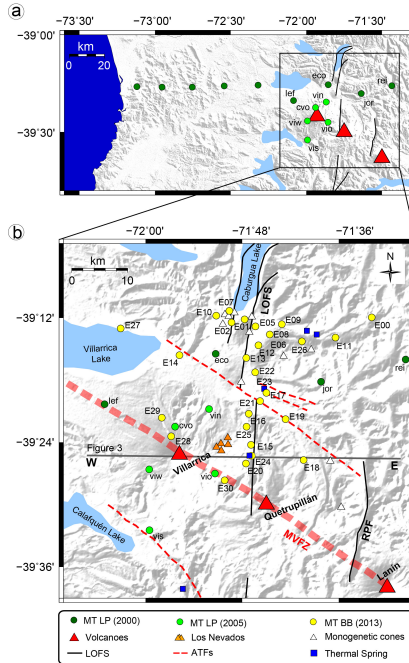
Figure 5.2.: a) Simplified topographic map of the research area that include main geological features and 2000-05 MT stations (circles). b) Zoom of research area including LP- and BB-MT stations (circles) used in the 3-D inversion models.

including the topography of the study area discretized from SRTM3 data using 50 m cell size in vertical direction and including topographic relief in the central region with a maximum elevation of 2850 m a.s.l. The vertical cells increased gradually to a maximum of 305 km. Horizontal mesh size was 1500 m × 1500 m in x and y directions, and in the central part of the mesh (30 km × 42 km) covers a 420 km × 380 km model space.

To test the robustness of the structures and their dependence on the inversion settings and the model parameters, we calculated models with different initial values and performed sensitivity tests. Despite the change in the initial resistivity values, the shape and position of the anomalies are preserved. The best fit of the model responses to the data was obtained with a homogeneous half-space of 100 Ωm. Detailed information is provided in the supplementary material.

5.3.2.2. The electrical resistivity models in the Villarrica Volcanic Chain

A cross-section of the preferred 3-D model along the Villarrica volcanic edifice to a depth of 30 km is shown in Figure 5.3, revealing asymmetric electrical structures across the volcanic chain. In fact, a strong lateral change in electrical resistivity along the east-west profile can be observed. At the western end of the profile the subsurface is highly resistive, R1 (>500 Ωm). Further east, the model shows a prominent near-surface C1 conductor with an electrical resistivity between 5 and 20 Ωm, located 1.5 to 5 km below sea level and 3 km east of the active Villarrica volcano (Figure 5.3a). C1 seems to be not connected to a deeper conductive zone. A second deeper, extensive conductivity anomaly C2 (20-35 Ωm) is located at depths between 4.5 and 18 km below sea level, and 15 km east of the active Villarrica volcano, below the extinct caldera of the Quetrupillán volcano, extending to the north (Figure5.3b). Two high resistivity structures, R2 and R3, with resistivity >500 Ωm, are located beneath the Los Nevados flank vent and the Quetrupillán caldera at depths above conductor C2 (Figure 5.3a). To the north, R2 and R3 are merged to form a single resistivity anomaly (Figure 5.3b).
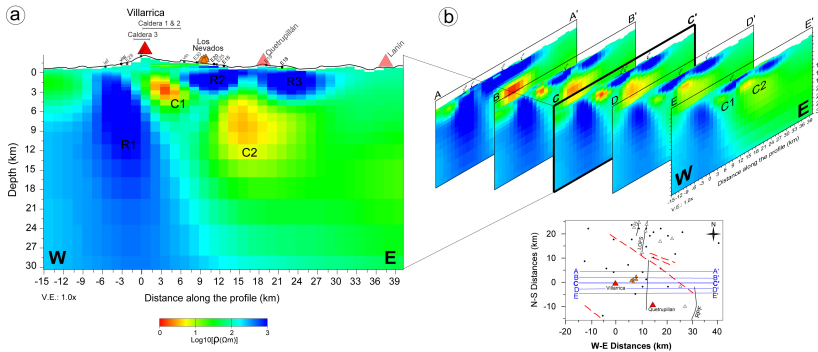
Figure 5.3.: a) Preferred 3-D MT inversion model shown by an east-west section across of Villarrica volcano. The location of W-E cross-section is shown in Figure. Villarrica volcano (red triangles) and their calderas and Los Nevados flank vent (orange triangles) are displayed. Cross section include MT stations by black dots on the profile and gray dots nearby sites. Quetrupillán and Lanín volcanoes has been included as a reference. b) E-W cross-sections.

5.4. Discussion

By using MT datasets with periods between 10^{-2} and 10^4 s, we aim to complement the conductivity models of previous MT studies (Held et al. 2016; Kapinos et al. 2016; Pavez et al. 2020) in the Villarrica volcanic chain, in particular by providing a more detailed and better resolution of the near-surface structures. We identified two structures in the crust with low resistivity values The first, labeled as C1, between 1.5 and 5 km below sea level and 3km east of the active Villarrica volcano. While, the second one structure, C2, between 4.5 and 18 km below sea level, and 15 km east of Villarrica volcano, but nearby the caldera of Quetrupillán volcano.

According to Morgado et al. 2015, analysis of the plagioclase phenocrysts from lavas of the 1971 Villarrica eruption indicating their origin from a shallow reservoir and that the lavas were fed from deep reservoirs with temperature and pressure conditions coincident with the depth of mantle-crust boundary. While, Lohmar et al. 2012a provides the conditions of a shallow magmatic reservoir for Villarrica based on the Licán ignimbrite (pressure of 0.67 kb and temperature between 900 and 1100 °C). This suggests the existence of more than one magmatic reservoir (shallow and depth) related to Villarrica, as interpreted by geophysical observations in other volcanic systems in the Central Andes (Pritchard et al. 2018; Díaz et al. 2020).

According to Simmons 2021, the plumbing system of Quetrupillán has developed as a transcrustal magmatic system composed of pockets of trachytic melt within a crystal mush, generated by fractional crystallization and crustal contamination of the basaltic melt injected into the system.

The identification of C1 and C2 will be based on the variable volcanic products observed in the Villarrica and Quetrupillán volcanoes, considers a magmatic system with two different magmatic reservoirs at different depths, with different magmatic composition and storage conditions.

Melt conductivity is controlled by temperature, pressure and melt composition (mainly SiO_2, Na_2O and water content). Several options of composition and storage conditions were tested, considering a range variability of several parameters such as magmatic SiO_2 content, temperature and pressure conditions, H_2O weight % and partially molten rate. The ranges of eruptive products in this area are established, mainly basaltic and basaltic-andesitic magmas in Villarrica and monogenetic and more evolved centers in Quetrupil-

lán (Table 5.1, Brahm et al. 2018; Hickey-Vargas et al. 1989; Lohmar et al. 2012a; Morgado et al. 2015; Robidoux et al. 2021; Simmons 2021).

The variability of electrical resistivity with all mentioned parameters is cal-

Table 5.1.: Whole-rock compositions of magmas belonging volcanic chain: Villarrica (Morgado et al. 2015; Lohmar et al. 2012a); Quetrupillán (Simmons et al. 2020); Los Nevados flank vent (Robidoux et al. 2021); Caburgua and Huellemolle (Morgado et al. 2015).

	SiO2 wt%	Na2O wt%	H2O wt%	T (°C)	P (MPa)	ρ (Ωm)
Basaltic-Andesite						
Villarrica 1	53.00	3.32	2.0	996	37	0.85
Villarrica 2	62.35	5.44	2.0	913	40	1.96
QVC 1	54.84	3.22	2.69	1022	49	0.53
QVC 2	65.03	4.75	2.42	1118	52	1.14
LNC 1	49.95	2.62	1.2	1128	41	0.87
LNC 1	57.06	3.26	1.1	983	19	1.16
Basaltic						
Caburgua	50.24	3.34	1.22	970	140	0.33-0.37
Huellemolle	50.95	3.23	1.22	1180	140	0.26-0.29

culated using equations derived from experimental data using SIGMELTS (Pommier and Le-Trong 2011) and a significantly changing the resistivity of a magmatic reservoir was estimated (Table 5.1). Thus, SiO_2 content ranges from 49.95 to 65.03 wt%, Na_2O 2.62 to 5.44 wt%, and water content ranges from 1.10 to 2.69 wt%. Assuming temperature ranges of 970-1200 °C for magmas of basaltic-andesitic composition, pure melt resistivity was estimated from ~0.85 to ~1.96 Ωm for Villarrica volcano, from ~0.53 to ~1.14 Ωm for the Quetrupillán volcanic complex (QVC) and from ~0.87 to ~1.16 Ωm for Los Nevados flank vent.

If the low resistivity anomalies detected beneath the Villarrica and Quetrupillán volcanoes are due to partial melting only, the minimum melt fraction needed to explain the MT data might be determined using a two-phase mixing models, which estimate low resistivity anomalies of magma reservoir and a resistivity of surrounding rocks. Modified Archie's law (Glover et al. 2000) as well as the Hashin-Shtrikman equation (Hashin and Shtrikman 1963) are used to combine the estimation of the electrical resistivity of the pure melt and the rock matrix. In the modified Archie's law (Glover et al. 2000) the melt bulk geometry can be distributed in highly interconnected (m=1.0), intermediate interconnected (m=1.5) and isolated pores (m=2.0). Hashim-Shtrikman upper bounds (HS+) would best represent the interconnectedness

of the melt, comparable with a high intermediate interconnected (m=1.3) in the modified Archie's law (Figure 5.4a). Therefore, to estimate melt rates, we used Hashim-Shtrikman upper bounds and high intermediate interconnected in modified Archie's law, which provide more realistic values.

The conductive anomaly C1 observed below Villarrica, with an electrical resistivity ranging between 5-20 Ωm, requires a basaltic melt fraction of 8 to 20% to explain the resistivity range (Figure 5.4b), while for the conductive anomaly C2, observed below Quetrupillán, a melt fraction of 5-12% is required (Figure 5.4c). Depending on the assumed temperature (900-1300 °C), a melt fraction ranging between 3% and 11% is possible. If higher values of pure melt resistivity are used, e.g., due to lower water or Na_2O content, then a higher melt fraction would be required. A water content of 1 wt% implies 13% melt (range 7-15%). Assuming a mush volume with melt fraction varying up to 20%, an extensive low-melt fraction crystal mush at depths between 8 and 20 km could be supported by the data. Even though, a melt fraction of 20% seems to be high, a significant part of this volume is likely to be distributed in non-eruptive parts of the reservoir (Allard 1997). Moreover, melt fraction between 8 and 16% would be required in the case of Los Nevados (Figure 5.4d) to explain the electrical resistivity of the intermediate crustal conductive C2 (Figure 5.3).

For instance, the upper crustal conductor C1 could be a temporary magma reservoir active during eruptions and fed by a deeper permanent and more permanent source, which is a working hypothesis from the petrological studies (e.g. Morgado et al. 2015). The conductivity is probably caused by partial melting and interconnected fluids and a resistivity of 20 Ωm at 2 km from the surface requires a melt fraction range of 8-20% depending on the melt resistivity (Figure 5.4b). Some constrained inversions show that even a resistivity below 10 Ωm is consistent with the data. Melt fractions >25% are also unlikely based on the geochemistry of the products.

Enhanced crustal permeability created by the LOFS enables the eruption of geochemically diverse magmas on a small scale (Hickey-Vargas et al. 2016; Morgado et al. 2017). In the SVZ, magmatic ascent has been facilitated by the LOFS (Cembrano and Lara 2009), and in fact diverse magma types have reached the surface, despite some common features acquired in the mantle source. These include melts directly extracted from the subduction-modified asthenosphere and magmas with signatures interaction with lithospheric mantle or even the upper crust. An important result observed in the resis-
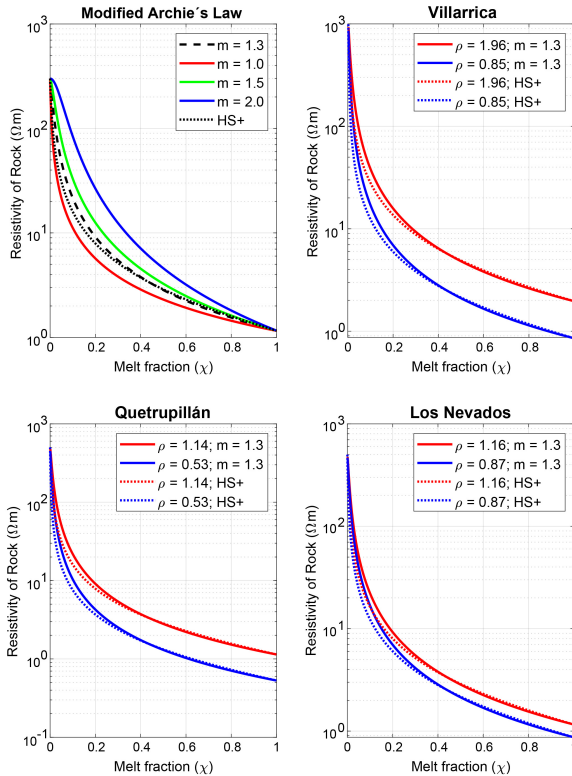
Figure 5.4.: Bulk resistivity of a partially molten rock as a function of melt fraction. a) Show the bulk resistivity computed using the modified Archie's law (Glover et al. 2000) for different degrees of melt interconnection: Highly interconnected (m=1.0) and moderately-well interconnected (m=1.5) to isolated (m=2.0). The dotted black line shows the Hashin-Shtrikman lower-resistivity bound (Hashin and Shtrikman 1963), which is representative for interconnected crustal melts. The dashed black line show the best scenario of interconnected (m=1.3). b) Villarrica lavas (from Moreno and Clavero 2006 and Lohmar et al. 2012a). c) Quetrupillán lavas (from Simmons et al. 2020). d) Los Nevados lavas (from Robidoux et al. 2021). The melt conductivity data were estimated using the SIGMELTS algorithm of Pommier and Le-Trong 2011. In b, c and d, high and low melt conductivity are plotted with red and blue colors respectively.

tivity models is associated with the intermediate crustal conductive zone (C2), which extends eastward from the LOFS. This feature might be showing that fluids are channelized but also trapped in the crust depending on the permeability of major structural systems as the LOFS and the transversal MVFZ. The damage zones of major faults would be channels for vertically di-

rect transport of fluids or for dispersed circulation depending on the tectonic domain (Held et al. 2018). Crustal rocks weakened by active faulting may also be able to capture and store magma ascending via dykes and hydrofructures (e.g. Gaffney et al. 2007; Le Corvec et al. 2013).

For the case study we observe that the conductive anomaly C2, below the volcanic chain, extends between the LOFS and the second-order RPF fault from a depth of 7 km (Figure 5.5) as a regional conductor. Although the 3-D inversion of the regional magnetotelluric data (Kapinos et al. 2016) with a coarser resolution shows a single conductor, which could be related to C2, is also spatially restricted between LOFS and RPF. This anomaly revealed in long-period MT data, could include the low-resisvity anomalies near and distant from the volcanic chain at intermediate depths (Figure 5.5).

Additionally, in our 3D model (Figure 5.5), the spatial orientation of C2 together with a conductivity anomaly to the north could explain the geoelectric strike rotation from N07°E at shallow depths to N30°E at intermediate depths. As well as, the direction and magnitude of the induction vectors, particularly at a depth interval of 11 s (Held et al. 2016). Therefore, the extension of the intermediate-low resistivity anomaly C2 most likely be connected to the NE-SW striking features such as the nowadays stress regime.

The conductive anomaly C2 shifted 15 km to the east of active Villarrica volcano is probably related to an offset of the LOFS (Figure 5.6). A deep magmatic reservoir shifted to the east of the arc font was also detected further south in the area of Osorno volcano (Díaz et al. 2020) and further north in the Planchon-Peteroa volcanic complex (Pearce et al. 2020). Likewise, MT studies at active volcanoes in the SVZ have provided evidence of low melt fraction (<15%) (Cordell et al. 2018; Díaz et al. 2020).

Magma arrest at C2 level could be a result of thermally or mechanically induced shear or tensile failure (Cruden and Weinberg 2018; Smith and Bruhn 1984) facilitated by deeply fractured crust where large temperature gradients between upper crustal rocks and the intruding magma are expected (Žák and Klomínský 2007). Simirlarly, C2 would be spatially and temporally associated with inherent pre-existing NW-striking pre-Andean structure (MVFZ) that promote the development of crustal magma reservoirs (Cembrano and Lara 2009).

Other physical properties of the earth can complement the characterization of the subsurface structure. For example, elastic properties of rocks that
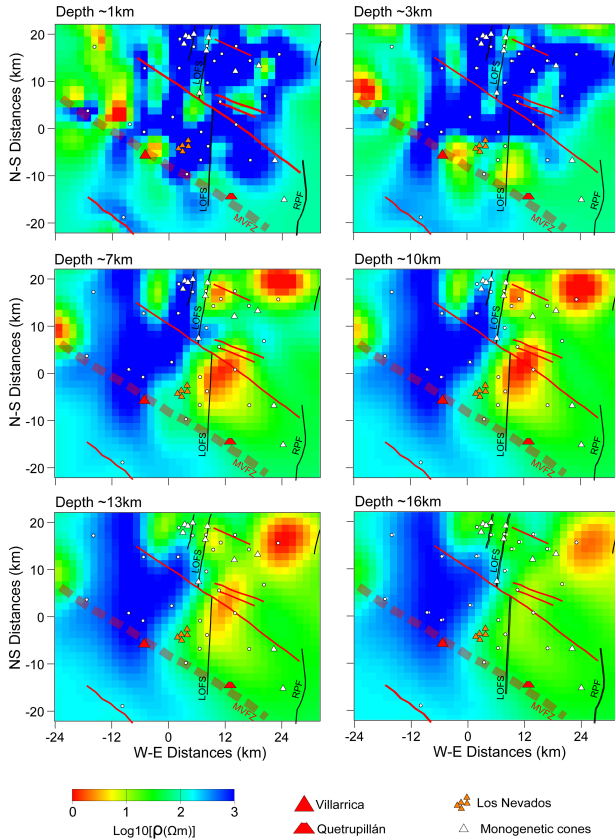
Figure 5.5.: Role of faults delineating conductivity anomaly at depth. Four horizontal plan view at different depths of the three-dimensional joint inversion modeling, in order to delimit conductivity anomaly as a function of the main N-S trend faults. Main tectonic feature are represented by black lines. a) ~0.5 km a.s.l., b) ~1.5 km b.l.s., c) ~2.5 km b.l.s., and d) ~4.5 km b.l.s.

are affected by partial melting can be used to constrain the melt fraction or densities of geological units vary with respect to the melt fraction, modifying the mass distributions (density deficiencies or excesses).

In the 2015 Villarrica eruptive episode, the pre-eruptive deformation was too small to be detectable (Córdova et al. 2015) and the eruption was followed by a short lived uplift of 5 cm in the SE part of the volcano from a source
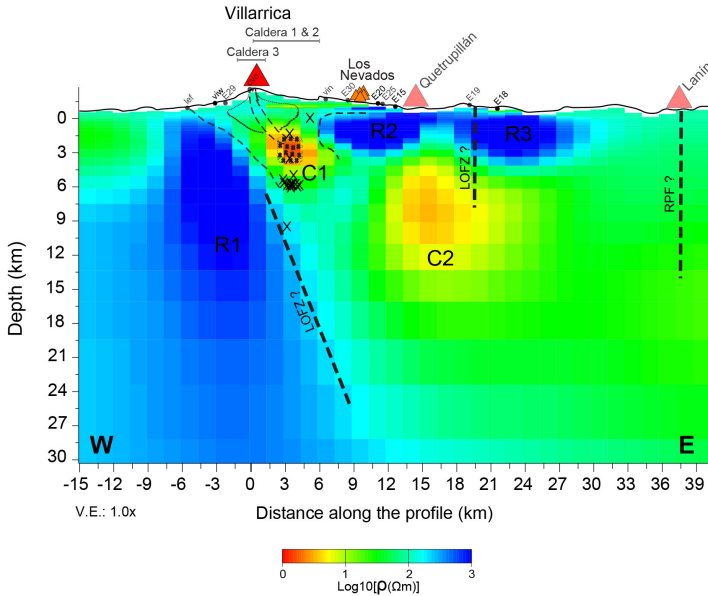
Figure 5.6.: Conceptual scheme of probable volcanic conduit and small shallow magmatic deposit associated to active volcano modified from Mora-Stock (2015) integrated with our preferred 3-D-MT inversion model. Black X represent the hypocenters of VT events (Mora Stock 2015.

depth of 6 km (Delgado et al. 2017). The source of ground uplift following this eruption is thought to be 5 km southeast of the volcanic edifice at a depth of ~4 km (Delgado et al. 2017), which is in agreement to the conceptual model proposed in this work (Figure 5.6) and support by the hypothesis suggested by Morgado et al. 2015 where a shallow magmatic reservoir (anomaly labeled as C1) may be activated during eruptions, fed an intermediate reservoir that underwent a heating episode (anomaly labeled as C1).

A logical scenario is that the melts do not necessarily reach the surface through the shortest and mostly vertical pathway but rather follow the direction of least resistance, i.e., they use existing fractures, ruptures, cracks of the brittle continental crust as conduits to reach the surface. Thus, the melt pathways proceed the geometry of the fractures. This may account for an offset between the magma deposit in the crust and the volcano edifice.

Aiuppa et al. 2017 demonstrated for the 2015 Villarrica volcano eruption that

the evolution towards CO_2 enriched gas was likely caused by unusual supply of deeply source gas bubble to the shallow Villarrica feeding conduit, possibly sourced by deeply primitive magma. In addition, Mora Stock 2015 identified low-velocity zones between 1 and 5 km depth related to the presence of magma or magma-derived fluids possibly communicating a deeper one.

Recent eruptive activity occurred between November 2022 and February 2023 at Villarrica has triggered a large number of volcano-tectonic events reported by Sernageomin (Figure 5.7a). The complete seismicity is located in the east border of Villarrica and coincide with anomaly C1. Most of the seismic activity are localized below and east of C1 and the high magnitude of VT-events are located close to the C1 (Figure 5.7b). Three horizontal sections (Figure 5.7c) would indicate that the localization of the seismicity can be classified in two clusters, one NW-aligned cluster at shallow depth (<4.5 km) and second NE-aligned cluster below of it. Therefore, C1 seems to be not only a transient feature but a long-live one, probably related to the geological structures.

The C1 anomaly can be imaged as a level of neutral buoyancy for fluids migration from a deep reservoir, probably facilitated by LOFS, while C2 would be a zone of magma storage or crystalline mush evolving through fractional crystallization within the crust. The link between C1 and C2 cannot be truly resolved in this study.

On the other hand, the high resistivity anomaly to the west of E-W profile, R1 (Figures 5.3 and 5.6), suggests that the deep-reaching fault acts as a lateral barrier between the more heterogeneous crust, as has been observed in previous studies in the Southern Volcanic zone (e.g., Brasse and Soyer 2001; Pavez et al. 2020; Pavez et al. 2022). Furthermore, in the E-W profile, east of anomaly C1, two high resistivity layer are observed at near-surface to a depth of about 3 to 5 km but merged to the north.

5.5. Conclusions

We show a 3-D resistivity model of the Villarrica volcanic chain in which both shallow conductors and deeper magma reservoirs are visible. The resistivity distributions show conductive anomalies associated with partial melting and/or fluids in reservoirs or faults, providing new insights to investigate the structural relationship with the Villarrica volcanic system.
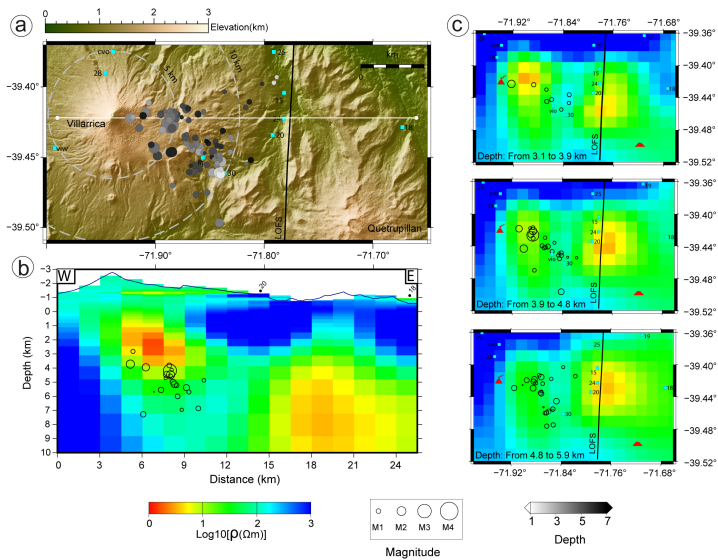
Figure 5.7.: a) Topographic map including the seismic activity at the Villarrica volcano recorded between November 07th, 2022 and February 07th, 2023 by SERNAGEOMIN (https://rnvv.sernageomin.cl/volcan-villarrica, accessed on 20 April 2023). Topographic highs correspond to Villarrica and Quetrupillán volcanoes. Cyan squares denote the MT stations. White line denotes the location of the W-E section. White dashed lines indicate the 5 and 10 km distance from the summit of Villarrica. b) Localized seismic events integrated with the W-E section across of MT model at Villarrica. c) Three horizontal plan view at different depths where seismicity well delimitate the lower boundary of anomaly C1.

Below and east of Villarrica volcano, the model indicates the presence of two magmatic reservoirs at crustal levels. A remarkable feature in the model is an extensive conductive structure C2 (<35 Ωm resistivity). Located below the volcanic chain at depth between 4.5 and 18 km. Given the resistivity value and in conjunction with geochemical and petrological observations, C2 would correspond to a deep reservoir where the melt has accumulated as a highly crystallized mush or a collection of discrete melt pockets. These NE-oriented low resistivity anomalies within the crust could be an explanation to the electrical resistivity anisotropy inferred in other works in south Chile (Soyer 2002; Brasse et al. 2009.

Another substantial finding is a well-constrained shallow conductivity anomaly C1 (5-20 Ωm). Based on geochemical and petrological observations, C1 could

be explained as transient basaltic andesitic reservoirs with variable melt amounts that could be controlled by the tectonic regime. The first-order LOFS would enhance the ascent of magma from different reservoirs providing a permanent, though not necessarily direct, connection between the mantle source and surface. Additionally, based on seismicity, C1 seems to be not only a transient feature but a long-live one, probably related to the geological structure.

The location of C2 within the intersection between LOFS and ATF results in compressive tectonic stresses that hinder magma ascent and so promote stalling and evolution of melt within the crust. A possible link between both reservoirs (C1 and C2) and a deeper reservoir would be due to LOFS that could enhance the deep magma, through a system composed of tensile and shear fractures, in a strike-slip regime, but oriented subparallel to the maximum horizontal stress (Cembrano and Lara 2009).

A next step in the use of geophysical methods such as magnetotellurics for volcanic exploration, is the use of this technique for monitoring purposes. Experiments of magnetotelluric monitoring in other volcanoes worldwide have been growing during recent years (e.g. Aizawa et al. 2013; Piña-Varas et al. 2023), showing interesting results when analyzing time varying signals and physical parameters obtained for different time frames. Through a collaborative project between the University of Chile and the National Geology and Mining Service from Chile (SERNAGEOMIN for the Spanish acronym), a permanent magnetotelluric station will be installed at Villarrica volcano, as an experimental effort to identify the capabilities of this geophysical technique to enhance the monitoring network of this volcano. For this experiment, the 3D model presented will be the baseline to identify changes in the electrical resistivity distribution along time.

Another key question concerns the plumbing system of Quetrupillán volcano and the magmatic system identified in the volcanic chain in this work. Deploying stations eastward of Quetrupillán volcano also allow investigating the role of RPF and its relationship with regional tectonic features.

Acknowledgements

Supplementary Material

Data fit

Figure 5.8.: Data-fit examples. a) and c) LP-MT stations. b) and d) BB-MT stations.

Inversion test settings

The resistivity of the homogeneous starting model was chosen after some inversion tests on four different resistivity values: 10, 100, 500, and 1000 Ωm. The inversion settings are as in Table S1. Each test required hence a different number of iterations. Figure S5.9 shows that the final RMS range between 1.15 and 1.37. The starting-model resistivity of 10 and 100 Ωm resulted in the lowest RMS values. The 10 Ωm test resulted in the lowest RMS and in the fewest number of iterations, the final model provide an overestimated deep resistivity contrasts. For this reason and due to the average apparent resistivity of all the sites, the resistivity of 100 Ωm was chosen for the starting model.

Model Assessments and Robustness of Features

Providing a realistic inversion model requires in addition to a thorough analysis of the data, an important review of the factors that determine the execution and the result of the inversion. In order to investigate the robustness of the

Table 5.2.: The inversion test settings performed on the MT data set of Villarrica Volcanic Chain. Inversion C inverted only the impedance (Z). Inversions A, B, D, E inverted, respectively, full Z and T.

Settings	A	B	C	D	E
Starting model	10 Ωm	100 Ωm	100 Ωm	500 Ωm	1000 Ωm
Tensor inverted	$Z + T$	$Z + T$	Z	$Z + T$	$Z + T$
Error floor $Z_{xy}Z_{yx}$	10%	10%	10%	10%	10%
Error floor $Z_{xy}Z_{yx}$	15%	15%	15%	15%	15%
Error floor $Z_{xy}Z_{yx}$	8%	8%	-	8%	8%
RMS	1.135	1.154	1.232	1.301	1.370
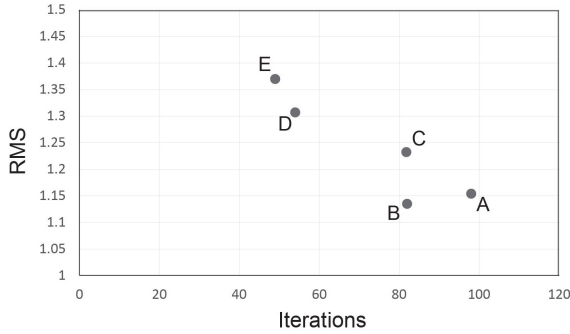
Figure 5.9.: Sensitivity analysis on the resistivity values of the homogeneous starting model for 3-D inversion. The RMS was using according with the last iteration for each 3-D inversion model setting.

low resistivity feature below the volcanic chain a sensitivity analysis was performed. We compared the anomalies labeled "a", "b" and "c" in Figure S5.10 to understand the differences between our model and previous. In the top of Figure S5.10 the LP-MT stations used by Kapinos et al. 2016, corresponding to the extended W-E profile, are shown, while in the bottom of Figure S2 display our preliminary resistivity model along the Villarrica-Quetrupillán-Lanín volcanic chain. We used the conductive characteristic "B" framed in the box for the assessments (Figure S5.10) and robustness of our model. It is well known that the accuracy and resolution of feature detection depends on the station separations, in some cases the accuracy of the model is limited due to the low electrical contrast between the surrounding structures. For example, intermediate resistivity anomalies could be dissipated in models with large
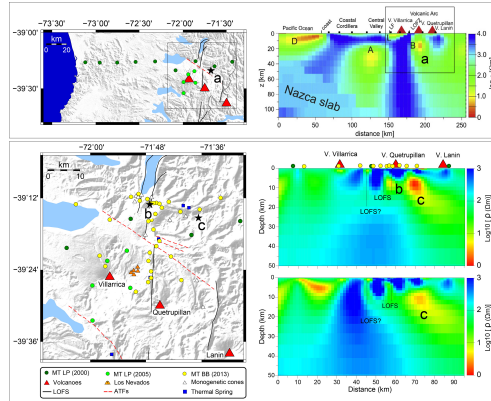
Figure 5.10.: Three high conductivity anomalies labeled with a, b and c selected to investigate variations as a function of grid size and minimum distance between nearby MT sites.Top left; topographic map of the research area that include main geological features and spatial distribution of high conductivity anomalies (black stars) and LP-MT stations (circles). Top right right; vertical cross-section of 3-D model modified from Kapinos et al. 2016, figure 8 Bottom left; ; topographic map including LP- and BB-MT stations. Bottom right; example of vertical cross-section of 3-D model of broadband data at south of Caburgua

cell sizes. Comparing the low resistivity responses, it shows that the greatest effect is seen in the small anomaly, i.e., anomaly characterizing LOFS (Figure S4.9). Therefore, the largest cell size to detect the anomaly labeled as "b" in Figure S4.8 is 3000 m. As the cell size increases, anomaly "b" vanishes and seems to merge with anomaly "c", obtaining anomaly "B" located below the volcanic chain, described by (Kapinos et al. 2016).

On the other hand, the lower crustal inversion model appears to recover the horizontal extension of anomaly B. This anomaly would extend northward between the LOFS and Reigolil-Pirihueico fault (RPF) faults. At the northern end of the anomaly, east of Lake Caburgua, it would form one structure, while at the southern end, volcanic chain; it would split forming two structures (Figure S4.8). Regarding the position in the vertical, anomaly "B" is located at shallow depth (~2 km upward), while its extension remain at approximately 20 km. This upward shift in the vertical is related to the size of the first cell, since it does not change the fit of the curves.

Sensitivity test
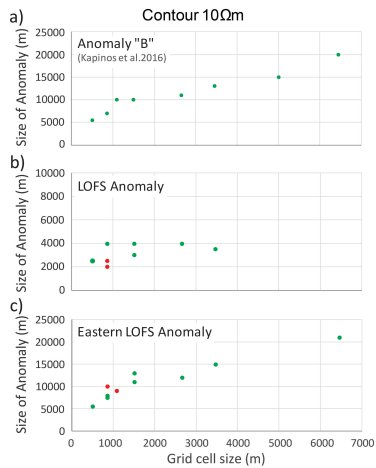
Figure 5.11.: Correlation analysis for variation in the size of the anomalies described in 3 based on different inversion models as a function of input parameter such as grid cell sizes. Green dots indicate inversion models without topography; Red dots represent inversion models including topography.
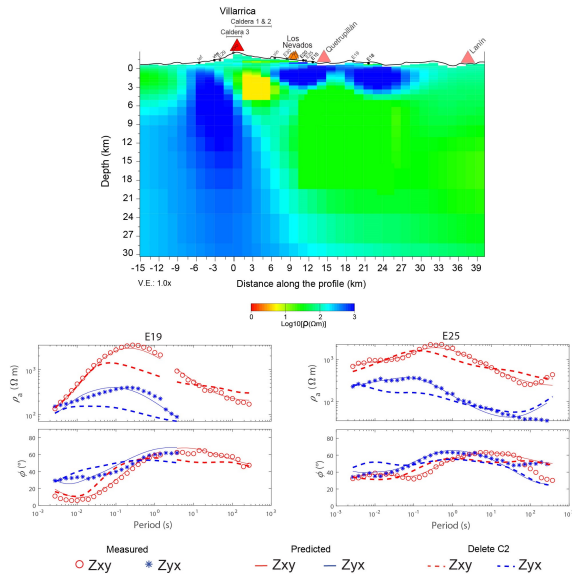
Figure 5.12.: Sensitivity test of conductor C2. a) Resistivity block (50 Ωm; resistivity of surrounding cells) is inserted instead of C2 anomaly. b) and c) Two example of apparent resistivity and phase curves of the non-diagonal components of the MT inversion model. Red represents the Z_{xy} component, blue the Z_{yx} component. The thin line represents the predicted data for the preferred model shown in Figure 3. The thick dash line represents the sensitivity test.

6.   Shallow and Deep Electric Structures in the Tolhuaca Geothermal System (S.Chile) Investigated by Magnetotellurics.

Abstract

The geoelectric properties of the geothermal system associated with the Tolhuaca volcano were investigated by three-dimensional (3-D) inversion of magnetotelluric (MT) data. This study presents the first resistivity model of Tolhuaca volcano derived from 3-D MT inversion to have a better understanding of its magmatic and hydrothermal system. We selected data from 54 MT stations for 3-D inversion. We performed a series of 3-D MT inversion tests by changing the type of data to be inverted, as well as the starting model to obtain a model in agreement with the geology. The final 3-D MT model presents a conductive body (<20 Ωm) located ~2 km below the summit of Tolhuaca volcano, inferred as a shallow magmatic storage compartment. We also distinguish a ~300 m thick layer of high conductivity (< 10 Ωm) corresponding to argillic hydrothermal alteration. The MT model includes two resistive bodies (~200 Ωm) in the upper crust below the laterally displaced argillic alteration layer to the west beneath the extinct Tolhuaca, which would correspond to a shallow reservoir (~1000 m from the surface) and a deep reservoir (> 1800 m from the surface) that had so far not been identified by previous resistivity models. The result of this study provides new insights into the complexity of the Tolhuaca geothermal system.

6.1. Introduction

The Andean volcanic arc is characterized by numerous hot springs, solfataras and geysers associated with abundant volcanic activity. Comprising more than 200 potentially active volcanoes and at least 12 giant caldera/ignimbrite systems (Stern 2004), it is a region with a vast potential for geothermal development.

In Chile, the Andean volcanism as a result of the subduction of the Nazca and Antarctic oceanic plates beneath South America (Stern 2004; Muñoz and Stern 1988; Cembrano et al. 2007) occurs in three segments separated by gaps or segments described as Central (CVZ; 14-28°S), Southern (SVZ; 33-46°S), and Austral (AVZ; 49-55°S) Volcanic Zones (Figure 6.1a). As a result, a wide range of volcano-tectonic configurations, crustal thicknesses and ascent pathways create different activity, products and morphology within volcanic zones (Cembrano and Lara 2009) and even between nearby volcanoes (Folguera et al. 2016; Lara et al. 2006a). More than 300 potential geothermal areas have been indicated throughout the Chilean Andes (Aravena et al. 2016; Lahsen et al. 2010), associated with Quaternary volcanism. The main high-enthalpy geothermal systems occur in CVZ (e.g. Apacheta, El Tatio) and SVZ (e.g. Tinguiririca, Mariposa, Tolhuaca) (Aravena et al. 2016). In areas where Quaternary volcanism is absent, Pampean flat-slab Segment and Patagonia Volcanic Gap, there are fewer hot springs or are less pronounced and their temperatures are usually lower (Lahsen et al. 2010).

According to variations in the petrology and geochemistry of its products, the Quaternary volcanism of the SVZ has been divided into four segments (Stern 2004; López-Escobar et al. 1995) (Figure 6.1a). Tolhuaca volcano is located in the South-Central Volcanic Zone (SCVZ: 37-42°S), which is characterized by, among others things, a reduced thickness of the continental crust, compared with areas further north, and a younger age of the subducted oceanic crust. The nature and origin of hydrothermal systems are strongly dependent on structurally controlled heat transfer mechanisms that define contrasting magmatic-tectonic-hydrothermal domains (Sánchez et al. 2013).

Both Lonquimay and Tolhuaca volcanoes are aligned with a WNW trend (Suárez and Emparan 1997; Pérez-Flores et al. 2017), and located in the arc-oblique long-lived fault systems domains that promote the development of magma reservoirs in the crust (Suárez and Emparan 1997; Sánchez et al. 2013). Both Pleistocene-Holocene volcanoes are built over Miocene volcano-
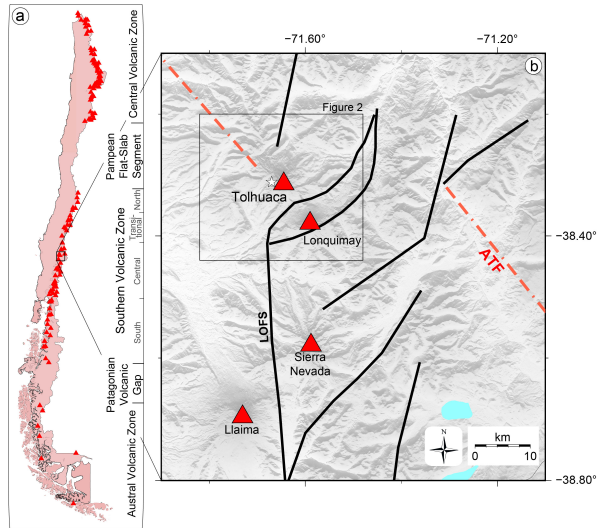
Figure 6.1.: a) Schematic map of the volcanic setting along the Chilean Andes showing the three main volcanic zones. All types of volcanic edifies are represented by red triangles (SERNA-GEOMIN, Servicio Nacional de Geología y Minería 2020 (accessed on 28 November 2022)). b) Simplified map of the major structural systems of the Liquiñe-Ofqui Fault System (LOFS) and the Andean Transversal Fault (ATF). Red triangles represent Holocene stratovolcanoes. Llaima and Lonquimay are counted among the most active volcanoes in Chile, while Tolhuaca is dormant and Sierra Nevada is extinct (Suárez and Emparan 1997). The white star indicates the location of the Tolhuaca Geothermal System.

sedimentary rocks (Moreno et al. 2012), which have high intrinsic porosity and permeability and thus enhance the development of hydrothermal reservoirs (Cembrano and Lara 2009; Sánchez et al. 2013).

Tolhuaca volcano is a glacially scoured stratovolcano (Lohmar et al. 2012b; Thiele et al. 1987). At the summit, there are several NW-trending aligned craters, indicating migration of the volcanic activity from SE towards the NW (Suárez and Emparan 1997; Thiele et al. 1987; Moreno et al. 2012), several hydrothermal manifestation and an active geothermal system.

Tolhuaca Geothermal System (TGS) has been investigated over the past decades by geological (e.g., Suárez and Emparan 1997; Moreno et al. 2012; Lohmar et al. 2012b; Sánchez-Alfaro et al. 2012; Pérez-Flores et al. 2017), geochemical (e.g., Sanchez-Alfaro et al. 2016; Collignon et al. 2021; Pérez-Moreno et al. 2021) and geophysical (e.g., Melosh et al. 2010; Melosh et al.

2012) studies, including magnetotellurics (MT). Classical MT and in particular the high-frequency variant of MT, audiomagnetotellurics (AMT) is frequently used to investigate magmatic reservoirs and deep geothermal resources to characterize the electrical resistivity of the structures of these systems with good resolution from a few tens of meters to several kilometers (Bertrand et al. 2012; Spichak and Manzella 2009; Munoz 2014).

Previous MT studies at areas surrounding TGS reveal upper crustal resistive structures at depths >10 km and conductive anomalies beneath active Lonquimay volcano. A conductive anomaly continues in the lower crust with an eastward dip and may be connected to the upper mantle (Brasse and Soyer 2001; Kapinos et al. 2016). While, the first electrical resistivity models at TGS detecting a clay hydrothermal alteration layer, at 400 m depth (Melosh et al. 2010; Melosh et al. 2012), and a resistivity image along the western flank of Tolhuaca volcano (Melosh et al. 2010).

Additional data from TGS was obtained from well logging (Lohmar et al. 2012a). A flow test of one of the deep wells identified a two-level reservoir with steam and steam-heated waters at shallow depth, and a deep fluid reservoir below (Melosh et al. 2012). The well temperature reaches 150-200°C at 500 m depth. Deep drilling revealed a fluid-dominated deposit at 300°C from 1100 to 2500 m depth (Lohmar et al. 2012a); Melosh et al. 2012.

The objective of this work is to gain a comprehensive understanding of the geoelectric properties of the geothermal system associated with Tolhuaca volcano in its western sector. For this purpose, MT data sets, including the full impedance tensor and vertical magnetic transfer function, obtained at Tolhuaca in recent decades have been reevaluated and interpreted by 3-D MT inversion.

6.2. Geological setting

The main tectonic features in the research area are the Liquiñe-Ofqui Fault System (LOFS) and the Andean Transverse Faults (ATF) ((Figure 6.1b) (Lavenu and Cembrano 1999; Rosenau et al. 2006; Pérez-Flores et al. 2016), forming a widely distributed structural system in the SVZ (Muñoz and Stern 1988; Hervé and Thiele 1987; Cembrano et al. 1996). Additionally, the major eruptive centers located in the research area are Tolhuaca volcano and Lonquimay Volcanic Complex volcanoes (Figure 6.2). The LOFS is a 1200 km-long intra-
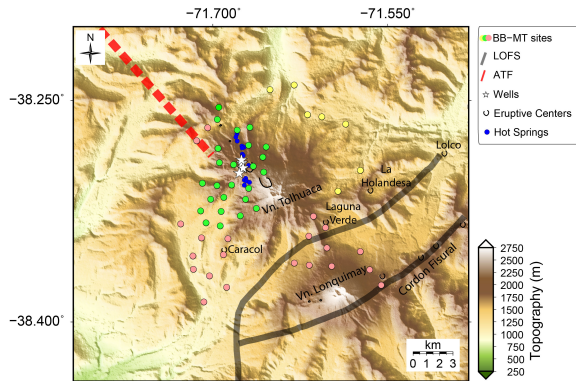
Figure 6.2.: Topographic map of the study area. The highest elevations correspond to the summits of Tolhuaca and Lonquimay volcanoes. Caracol, La Holandesa, Laguna Verde and Lolco pyroclastic cones aligned WNW-ESE are located between the two major summits (Moreno and Gardeweg 1989). Yellow, green and pink circles show locations of the 2007, 2014 and 2019-20 magnetotelluric sites used for this study. White stars indicate wells. Black lines outline the eruptive centers. Blue circles indicate hot springs. Elevation data are obtained from the SRTM1 Global relief model (NOAA 2022).

arc strike-slip fault system, defined by a series of major NNE-striking, right-lateral, strike-slip faults associated with NE-striking normal-dextral faults that splay off NNE-striking faults (Cembrano and Lara 2009; Rosenau et al. 2006; Lara et al. 2006b; Melnick and Echtler 2006). In the domain of research area, LOFS come into a play in its eastern section with spatial arrangement forming duplex and horsetail geometries (Figure 6.1) (Cembrano and Lara 2009; Rosenau et al. 2006; Moreno and Gardeweg 1989). In turn, four independent monogenic volcanoes (Caracol, Laguna verde, La Holandesa and Lolco) were built on a branch of LOFS (Figure 6.2) (Suárez and Emparan 1997; Moreno and Gardeweg 1989).

The ATF is formed by a series of NW-striking faults inherited from pre-Andean geological processes (Figure 6.2) (e.g., Pérez-Flores et al. 2016; Radic 2010). In the Central and Southern Andes, the faults that conform the ATF are spatially and genetically associated with the occurrence of Quaternary volcanism (Cembrano and Lara 2009; Sánchez et al. 2013; Lavenu and Cembrano 1999; Lara et al. 2006b; Lara and Folguera 2006; Sánchez-Alfaro et al. 2012). Likewise, ATF partially controls the past and present-day fluid flow and volcanic activity (Lara et al. 2006b; Lara and Folguera 2006). Tolhuaca volcano is located at the intersection of the LOFS and one fault of the ATF

(Figure 6.1b), thus providing a potential long-lived pathway for the ascent of deeply stored fluids (Sanchez-Alfaro et al. 2016; Pérez-Flores et al. 2016).

Several Cretaceous to Lower Pleistocene stratified sequences, together with Miocene plutonic rocks and Miocene-Pliocene hypabyssal intrusives (Suárez and Emparan 1997; Moreno et al. 2012), form the basement of both Tolhuaca volcano and Lonquimay Volcanic Complex. The N-NE Liquiñe-Ofqui Fault System is the first-order structure that crosses between Tolhuaca and Lonquimay volcanoes. The second-order alignments are the NE-SW, trending the four independent monogenetic volcanoes, and the NW-SE, trending the two major volcanoes (Figure 6.2).

Tolhuaca volcano (2,806 m a.s.l) is a middle Pleistocene stratovolcano, with a NW fissural structure and numerous volcanoclastic rocks at its base (Suárez and Emparan 1997; Moreno et al. 2012). It is an elliptical feature with a major axis of 20 km (northwest-southeast) and a minor axis of 13 km (Thiele et al. 1987; Moreno et al. 2012) (Figure 6.2). Its summit rises above the mid-level of the basement of Oligo-Miocene volcanic sedimentary rocks and Miocene granitic rocks of the Patagonian batholith (Suárez and Emparan 1997; Thiele et al. 1987). Two upper craters represent the last eruptive phases of the volcano; a 2 km long fissure and a pyroclastic cone are linked to a lava flow. All are oriented to the N-NW and enhanced by glacial action. At the SE termination of the summit of Tolhuaca, glaciers can still be observed, with a total area of ca. 5 km^2 (Suárez and Emparan 1997).

Basaltic and basaltic-andesitic lavas and pyroclastic flows intercalated with andesite and dacite lava flows dominate the eruptive products (Lohmar et al. 2012b; Melosh et al. 2010; Moreno et al. 2012). The main stratovolcano was formed about 280 and 30 ka ago, through four morphostructural units, with lava flows and dike, basaltic to dacitic in composition (Thiele et al. 1987; Lohmar et al. 2012b). However, Tolhuaca volcano has no record historical eruptions (Suárez and Emparan 1997; Thiele et al. 1987). The most recent units developed between about 30 ka and the Holocene, with basaltic to silicic andesitic lava flows.

On the NW flank of Tolhuaca volcano, the TGS has developed with reservoir temperatures estimated at 220-300°C (Lohmar et al. 2012b; Melosh et al. 2010; Melosh et al. 2012), characterized by several surface hydrothermal manifestations (Figure 6.2). Fumaroles, solfataras and hot springs are located in the NW fissure (Melosh et al. 2010; Hauser 1997), suggesting the existence of a NW striking fault that promotes hydrothermal and magmatic ascent

(Sanchez-Alfaro et al. 2016). The geothermal field is spatially associated with both the LOFS and the ATF (Cembrano et al. 2007; Sanchez-Alfaro et al. 2016; Melnick et al. 2006; Pérez-Flores et al. 2016) (Figure 6.1).

. Two slim holes (Tol-1 and Tol-2) and two larger diameter wells (Tol-3 and Tol-4) (Figure 6.2) up to 2117 m vertical depth, suggest the presence of a geothermal reservoir at approximately 1.5 km below surface (Lohmar et al. 2012b). Liquid saturated conditions were determined with temperatures of up to 300°C and a strong meteoric water component (Melosh et al. 2012). The reservoir appears to be covered by a steam-heated aquifer at shallow depths reaching up to 160°C (Melosh et al. 2010; Melosh et al. 2012). The well Tol-1 was continuously cored to 1073 m depth. Drilling paused for a flow test demonstration of the shallow 150°C to 160°C steam reservoir between 120 m and 320 m depth (Melosh et al. 2010).

Lonquimay volcano (2,865 m a.s.l.), located 8 km southeast of Tolhuaca volcano (Figure 6.2), is a symmetrical cone whose basal stage on basaltic to basaltic andesitic rocks started within the Upper Pleistocene (Polanco et al. 2014). The main cone formed from the upper Pleistocene to the early Holocene, with accumulations of basaltic to intermediate andesitic. Younger units are Holocene, with basaltic to andesitic lavas that flowed onto the northern, western, and southern flanks of the cone. From Holocene to present, volcanic activity has been concentrated in the Eastern Cordon Fisural (Suárez and Emparan 1997; Lara et al. 2012) (Figure 6.2). Historical volcanic activities of Lonquimay have been recorded in 1853, 1887-90 and 1988-90; the latter formed the Navidad ("Christmas") crater and an andesitic lava flow extending ~10 km to the north (Moreno and Gardeweg 1989) (Figure 6.2).

6.3. Magnetotelluric: Data, processing and results

Magnetotellurics (MT) is an electromagnetic method that records the fluctuations of electric and magnetic fields at the Earth's surface to obtain information on the resistivity distribution at depth. Since the penetration depth of electromagnetic fields into the Earth covers a large depth range, MT is used in crustal and even mantle studies to image the resistivity distribution. Depth of penetration decreases as the EM signal frequency increases.

In volcanic environments, MT is used to image conduits or magmatic reservoirs (Hill et al. 2015; Comeau et al. 2015; Aizawa et al. 2014), hydrothermal fluids (Peacock et al. 2016; Heise et al. 2008) and clay layers (Newman et al. 2008). In the southern volcanic zone, MT studies have characterized magmatic systems (Brasse and Soyer 2001; Kapinos et al. 2016; Cordell et al. 2018; Díaz et al. 2020), geothermal reservoirs (Melosh et al. 2010; Melosh et al. 2012), fluid pathways (Cordell et al. 2019; Pavez et al. 2020) and mid-crustal conductors (Held et al. 2016; Reyes-Wagner et al. 2017).

6.3.1. Data acquisition

The new MT data, which complement earlier data sets, were acquired during two field campaigns. In 2019, between November and December, we deployed 25 broadband magnetotelluric (BB-MT) stations mainly in the area between Tolhuaca and Lonquimay volcanoes. In March 2020, we added four additional BB-MT stations at the northern flank of Lonquimay. Combining the new MT data with previous datasets, we used a total of 54 BB-MT stations (Figure 6.2) to investigate the underground resistivity at crustal depths along the Tolhuaca volcano and the Lonquimay Volcanix Complex. A period band of 10^{-3} to 512 s was chosen for data acquisition.

Measurements were carried out using four BB-MT stations each equipped with a Metronix ADU-07e data logger. Magnetic fields were obtained using three MSF-07e coil magnetometers, buried into the ground for thermal and mechanical stability, and oriented in N, E and vertical directions. Electric fields were obtained by voltage difference taken over a dipole extension of 90 m, using four EFP-06 electrodes (Metronix Inc.) oriented in N-S, E-W direction. The time series of the horizontal components of the electric (E_h) and magnetic (B_h) fields, as well as the vertical component of the magnetic field (B_z) were recorded over 48 hours. To be able to apply remote reference processing (Egbert and Booker 1986), two stations were always operated simultaneously.

6.3.2. Processing and inversion

The processing of the broadband EM time series was performed with a robust code based on Egbert and Booker 1986 and Egbert 1997 that includes filtering of nearby artificial EM sources that may invalidate the plane-wave assumption of the MT fields. In addition, the remote referencing technique (Gamble

et al. 1979) is applied which leads to a significant improvement of the transfer function quality in the so-called dead band from about 1 to 10 seconds where the natural source signals are generally weak. From this robust processing, the complex impedance tensor (Z), defined by the relationship $E_h = Z \cdot B_h$ between the horizontal electric field and magnetic induction, E_h and B_h respectively, is estimated. In addition, robust processing also estimates the geomagnetic transfer function T ("tipper"), defined as $B_z = T \cdot \vec{B}$.

Apparent resistivity and phase curves corresponding to the impedance tensor elements Z_{xy} and Z_{yx} for the reference sites TGA-712a, T248a and Tol23, located northeast, west and southeast of Tolhuaca volcano, are shown in Figure 6.3. Here, the large split of apparent resistivity curves indicates a conductive anomaly at depth.

Our goal is to provide a 3-D resistivity model of Tolhuaca volcano to under-
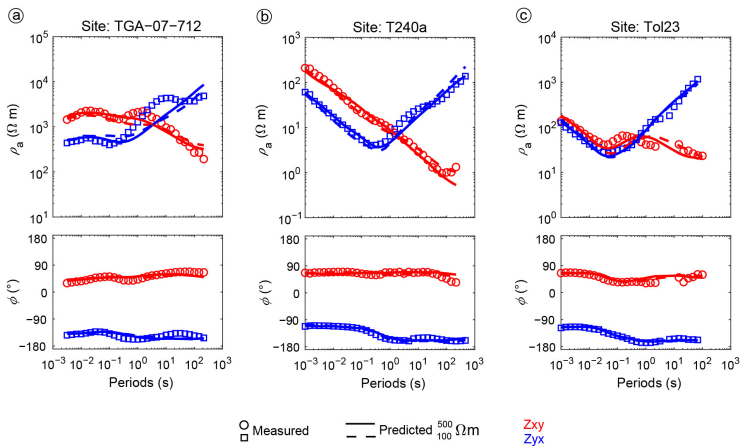
Figure 6.3.: Three example of apparent resistivity and phase curves of the non-diagonal components of the MT data (Measured) and responses of inversion model (Predicted). Red represents the Z_{xy} component, blue the Z_{yx} component. Thick line represents the predicted data for the preferred 500 Ωm initial model (model shown in Figure 6.5). Dashed lines represent the predicted data for the initial 100 Ωm model. a) Example of data measured in 2007. b) Example of data measured in 2014. c) Example of data measured in 2019 and 2020.

stand better its magmatic and hydrothermal system by correlating it with geological and well logging information. To achieve this goal, we applied an inversion process, in which the observed impedance data were fitted by least squares method to the calculated data.

Three-dimensional inversion of impedance tensor and geomagnetic transfer function data was performed using the "Modular System for Inversion of Electromagnetic Geophysical Data, ModEM" developed by Kelbert et al. 2014. The main advantage of ModEM is the fast convergence that finally allows the joint inversion of the impedance tensor together with the tipper transfer function. The inversion settings, 3-D mesh and results were prepared and analyzed using the 3-D-Grid Academic software (Melbeq, pers. comm.).

A regular grid extending over 100 (N-S, positive northward) × 90 (E-W, positive eastward) cells with a uniform size of 250 m × 250 m was used in the model core. To avoid boundary effects, 18 padding cells with an increasing factor of 1.3 were added to this model core. Topography was included of the study area discretized from SRTM3 using an initial cell size of 50 m and included 1750 m of topographic relief throughout the region with maximun elevation of 2865 m a.s.l. and a minumun elevation of 865 m a.s.l.The vertical cells continue with an increasing factor of 1.2; thus, 77 layers conform the vertical direction. In total, the grid extends 130 km × 100 km in the horizontal directions and to about 300 km depth, in accordance with the conditions and depth of the electromagnetic skin effect.

A set of different starting models were tested for the inversion. They all used a homogeneous half-space with varying initial resistivity values of 10, 100, 500 and 1000 Ωm. The tests were conducted to find the best fit to the data and the highest agreement of the MT models with the known information of the complex geology of the surrounding area of Tolhuaca volcano. We found that the shape and location of the anomalies obtained were independent of the initial resistivity values. Please refer to the Supplementary Material for a comprehensive explanation of the different inversion tests and their settings.

Figure 6.4 shows that the lowest Root Mean Square Error (RMS) of 1.35 was reached in the inversion test using an initial homogeneous half-space of 100 Ωm. However, the 500 Ωm resistivity value produced the second lowest RMS of 1.48 and since it was consistent with information from exploration wells it was chosen as the starting model. In general, the 500 Ωm initial model provides less extreme resistivity values that are more geologically realistic while the initial 100 Ωm starting model resulted in unrealistically large conductive anomalies with resistivity values below 1 Ωm. Therefore, all future models used the initial model with a 500 Ωm homogeneous half-space. Inversion tests, including joint inversion of Z and T, and non-diagonal and diagonal components of Z were performed. Finally, in the inversion, we included all
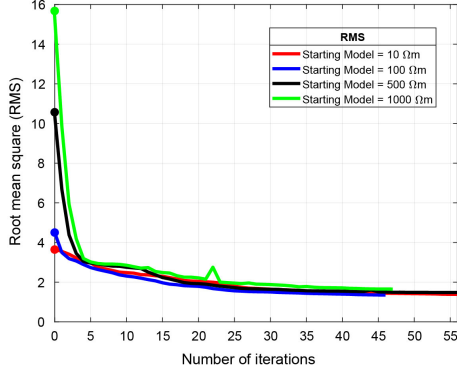
Figure 6.4.: Number of iterations versus root mean square misfit convergence curves for the MT inversion (model shown in Figure 6.5) with the a priori inversion and the fixed inversion (both models shown in Figure 6.9). The black lines represent the preferred starting model. The dots denote the initial RMS. The inversion with starting model of 10 Ωm began with the lowest RMS whereas the 1000 Ωm starting model began with a high RMS misfit. However, all starting models converged to similar misfit.

Z components, as well as the T components to improve sensitivity at depth and to investigate lateral constraints. After assessing the quality of our data for the inversion, we dispose a subset of data to be used efficiently in the 3-D inversion program. Consequently, we selected 25 of 29 sites from 2019-20, 21 of 74 sites from 2014, and 10 of 18 sites from 2007, at which transfer function were calculated for 42 logarithmically distributed periods between 0.000146 s and 1000 s, with 6 periods per decade.

We set an error floor as a portion of the absolute value of the impedance components ($|Z_{ij}|$) instead of the mean of the non-diagonal components ($|Z_{xy} \cdot Z_{yx}|^{1/2}$), because the mean value might have underestimated one component of the impedance tensor relative to the others (Tietze and Ritter 2013; Pace et al. 2022). For the Z_{xx} and Z_{yy} components, the error limit was set to a minimum value of 15% and for the Z_{xy} and Z_{yx} components to 8% (error floor). However, if the data error of some data was higher than this error limit, the original data error was adopted for these data. Higher values for the components Z_{xx} and Z_{yy} weight the on-diagonal components lower, since the data quality is lower here. For the real and imaginary parts of geomagnetic transfer functions the error floor was set to 5%.

6.3.3. The three-dimensional resistivity model

The preferred 3-D model provides high resolution of electrical structures up to 20 km depth. In the study area, there is a strong lateral change in electrical resistivity. On the western flank of Tolhuaca volcano a resistive body (>1000 Ωm) with an extension of approximately 5 km in the WE direction extends towards 12 km depth.

The model shows a prominent sub-vertical conductive structure C1 with a resistivity of 5-30 Ωm beneath the old crater of the Tolhuaca volcano at a depth of 2 km (Figure 6.5). C1 seems to be connected to a deeper zone, an elongated intermediate-resistive structure of (200-400 Ωm, labeled R1 in Figure 6.5), dipping southeast and extending to a depth of about 6 km.

Since the low resistivity anomaly, C1, is such a conspicuous feature in the 3-D resistivity model, persisting in all models, several sensitivity tests were carried out in order to determine the feasibility of C1. For the sensitivity tests, the low resistivity structure was replaced with different resistivity values (see supplementary material) and the resulting data misfit was up to 35% larger when compared to the model including the low resistivity structure. This indicates the importance of a conductive anomaly in order to explain the measured MT data.

The model along the Tolhuaca volcanic edifice shows a layer composed of
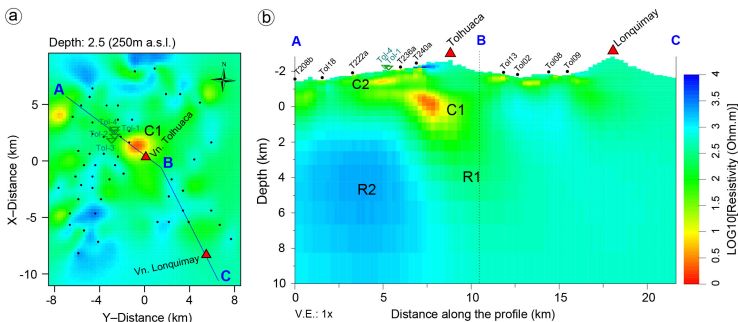
Figure 6.5.: Preferred MT resistivity model shown by vertical slice along profile ABC. a) Horizontal plan views at 2.5 km (250 m a.s.l.) depth. c) AB northwest diagonal cut along the NW flank of Tolhuaca volcano, passing through the well exploration site. BC N-NW diagonal cut connecting the Tolhuaca and Lonquimay volcanoes. Dashed black lines in the vertical sections show intersection of the profiles. The black dots and green inverted triangles on the vertical and horizontal sections are the locations of MT sites and exploration wells, respectively.

several conductive anomalies (<40 Ωm) spatially distributed near the surface (Figures 6.5 and 6.6). Within this conductive layer, a rather highly conductive anomaly ($\sim 20\Omega m$) is observed in the vicinity of the geothermal wells (star in Figure 6.6a and b). An extensive conductive anomaly, C2, below the exploration wells is imaged, extending approximately 2 km in N-S direction and 1.2 km in E-W direction, with a thickness of 200 m (Figure 6.6b). On the northwest flank of Tolhuaca volcano, a narrow conductive anomaly, C3, is visualized, extending approximately 0.5 km in N-S direction and 2 km in E-W direction, with a thickness of 200 m (Figure 6.6b). Southeast of Tolhuaca volcano, a conductive anomaly with similar characteristics to the one mentioned above is also revealed (Figure 6.6c and d).

In between Tolhuaca and Lonquimay volcanoes, specifically in the southeast
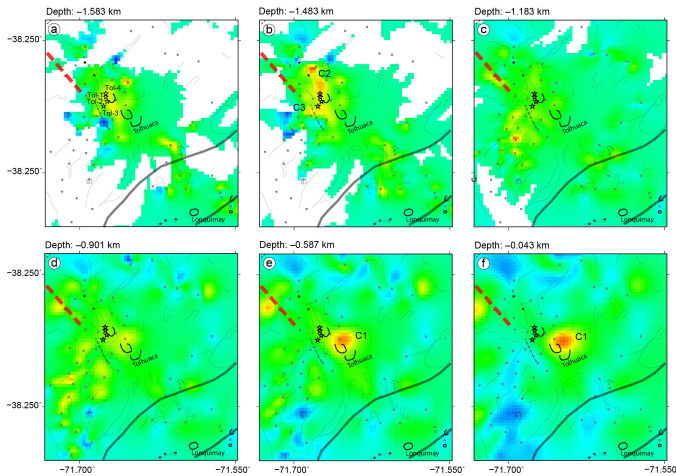
Figure 6.6.: Plan view of the 3-D model obtained from inversion presented for six different depths showing the relationship between conductive anomalies spatially distributed near the surface and geothermal surface manifestations and volcanic lineaments shown in Figure 6.2. Gray dots represent MT sites. Stars represent wells.

flank of Tolhuaca, a conductive anomaly of $\sim 20\Omega m$ with a thickness of 500 m is also identified (Figure 6.6a); however, the lateral extent is not well resolved due to limited coverage with MT stations.

In the eastern part of the study area, the subsurface is characterized by a homogeneous intermediate to low electrical resistivity (Figure 6.6). Note,

however, that coverage with MT sites is low east of Tolhuaca and that the model is therefore poorly constraint in this area. The absence of low resistivity structures beneath active Lonquimay volcano in our model (structures which could be associated with a possible shallow magmatic source) might therefore be due to an insufficient coverage with MT stations (Figure 6.6e and f).

6.4. Discussion

6.4.1. Shallow crustal melt zone

3-D inversion of MT data in Tolhuaca volcano shows a high conductivity anomaly, C1, at shallow crustal levels at depth of ~3 km. This well-defined anomaly underlies beneath the former eruptive crater on the NW flank of Tolhuaca volcano (Figure 6.5 and 6.7). C1 appears to be connected to a lower conductor. The elongated intermediate resistivity R1, below C1 (Figure 6.5), would probably represent a sub-vertically dipping basaltic-andesitic dike-like structure (roughly NW-SE oriented), which acted as a feeding zone for the magmatic system of Tolhuaca volcano and also serves as a path for high temperature geothermal fluids. The extent of this structure at depth and to the east cannot be delimited by this study. However, the geometry of R1 (Figure 6.7) would provide evidence for the existence of a fault dipping to the east that extends throughout the crust, forming weak zones that channel the ascent of fluids. Furthermore, the higher resistivity towards the western part, R2 (Figure 6.5), suggest that the eastern deep-reaching fault acts as a lateral barrier between the more heterogeneous crust, as has been observed in previous studies in the SVZ (e.g., (Kapinos et al. 2016; Pavez et al. 2020; Díaz et al. 2020). The enhanced conductive of C1 (between 5 to 25 Ωm), may be explained by high content of brines or a low melt fraction. Dacitic lava is dated to 50 ka (Thiele et al. 1987), meanwhile the youngest basaltic lava flow/volcanic event is dated to be less than 6 ka (Melosh et al. 2012). Therefore, the presence of partially crystallized melt could be probable. From a magma residence and crystallization point of view, 50 ka is sufficient time to completely cool small and shallow magma chambers. However, in our case, we assessed a volume >35 km^3 for C1, small-medium magma chamber size, and the occurrence of residual melt (mush) is a possibility.

We estimated the time scale of magmatic cooling using the model of (Bonafede et al. 1984; Hawkesworth et al. 2000). In a 35 km^3 magma chamber, basalt
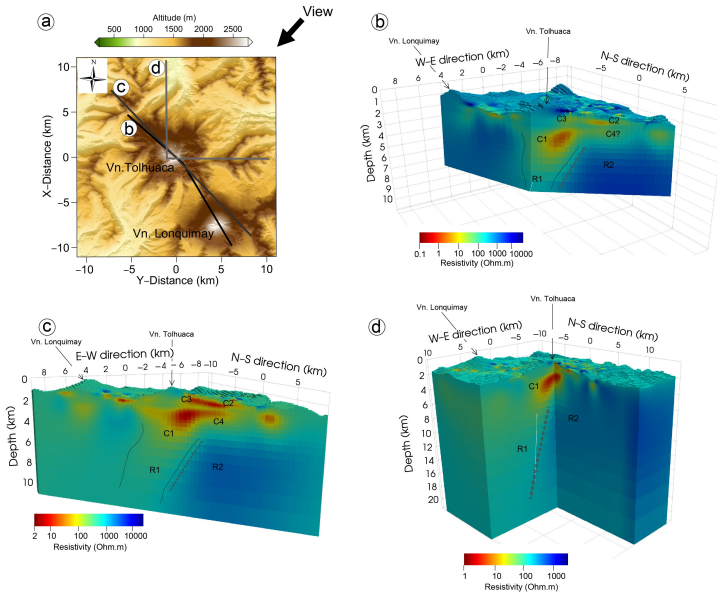
Figure 6.7.: a) Topographic map including three vertical slices of the preferred 3-D MT model. High altitudes correspond to the summit of volcanoes. b) Multi-segment cross-section through the wells and major volcanoes are shown in Figure 6.5. c) NW-SE cross-section magmatic and hydrothermal fluid pathways. d) Three-dimensional resistivity image derived from N-S and E-W orthogonal profiles in order to the inferred position and extension of the crustal long-term magmatic storage denoted by C1.

magmas (density of 2600 kg/m^3, specific heat capacity of 1500 J/kg per K and the latent heat of crystallization of 410^5 J/kg (Spera 2000), an initial temperature of about 1100°C should reach 75% crystallization after ∼12000 years. On the other hand, deep drilling revealed a fluid-dominated deposits at about 300°C and to a minimum depth of 1100 m. Thus, a temperature of about 800°C is possibly expected at 3 km of depth and this temperature is high enough to maintain a partial amount of melt.

Upper-crustal magma chambers spend the vast majority of their lifetimes at relatively cold (less than 750°C) conditions, i.e. "cold storage" (Cooper and Kent 2014), or tens to hundreds of thousands of years of storage under dominantly hotter conditions, i.e. "warm storage" (Barboni et al. 2016). If the "cold storage" model is applicable, detection of melt beneath volcanoes is likely a sign of imminent eruption (Cooper and Kent 2014). However, some

arc volcanic centers have been active for tens of thousands of years and show evidence for the continual presence of melt, which suggest that arc magmas are generally stored warm. Thus, the presence of intracrustal melt represents the normal state of magma storage underneath dormant volcanoes (Barboni et al. 2016).

We estimated different melt portion values as a function of the different dominant lavas of Tolhuaca volcano (Figure 6.8). As a result of the limited geochemical and petrological data of lavas and eruptive products of Tolhuaca, the bulk resistivity for different melt fractions was computed assuming diverse basaltic-andesitic, andesitic and dacitic melt compositions, using the models of Guo et al. 2016 and Guo et al. 2017 at a depth of 3 km (Figure 6.8a). Figure 6.8a shows resistivity values for basaltic-andesitic, andesitic and dacitic lavas varying water content, as a weight percentage (H_2O wt%). Pink bands represent values that are compatible with MT. The orange area represents electrical resistivity estimations for magmas of Tolhuaca. The
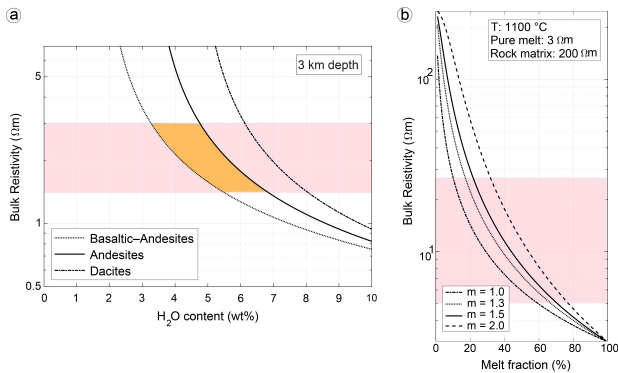
Figure 6.8.: a) Variation of electrical conductivity with water content for different melt compositions, using the models of Guo et al. 2016 and Guo et al. 2017. b) Bulk electrical resistivity of a two-phase system depending on the melt fraction for basaltic-andesitic melt with a resistivity of 3 Ωm, for different degrees of melt interconnection: Highly interconnected (m=1.0) and moderately-well interconnected (m=1.5) to isolated (m=2.0).

melt resistivity was estimated and combined with the matrix rock resistivity by the two-phase mixing model (Glover et al. 2000) for various degrees of melt interconnection (from interconnected melts, cementation factor m=1.0 to isolated melts, m=2.0), giving the fraction of melt needed to explain the observed resistivity of the melt and rock matrix.

Assuming a resistivity range of 5-25 Ωm in the anomalies, a minimum melt fraction of 5% (Figure 6.8b) is required in the case of a highly interconnected melt (m=1.3) to account for the resistivity values (Figure 6.7). A maximum melting fraction of 30% is required if the melt is not well connected (m=2.0) (6.8a). Depending on the temperature (900-1200°C), a melt fraction range of 3% to 11% would also be possible. If higher values of pure melt resistivity are used, e.g., due to lower water or sodium content, a higher melting fraction is required. Therefore, basaltic-andesitic residual melt (Figure 6.8) would explain the low resistivity value of the anomaly located beneath the NW flank of the volcano.

The Tolhuaca magmatic system appears to be at a more mature and in a crystalline stage. Therefore, C1 would correspond to the long-term residence of a subsurface magmatic intrusion associated with ATF structural control (Cembrano and Lara 2009; Pérez-Flores et al. 2016; Cooke et al. 2019; Sanchez-Alfaro et al. 2016), which would serve as a heat source for the Tolhuaca geothermal system. Numerical simulations of heat and fluid flow (Sanchez-Alfaro et al. 2016) would suggest the existence of a heat source of the Tolhuaca geothermal system associated with a magma body intruding at a depth of ~3 km below the summit of Tolhuaca volcano (Sánchez-Alfaro et al. 2012). If this were the case, anomaly C1 would correspond a shallow magmatic body triggering an increase in fluid enthalpy and a decrease in fluid pressures as a result of a transition of the hydrostatic pressure gradient to a fluid-saturated (boiling) environment at a shallow reservoir (Sanchez-Alfaro et al. 2016).

There is evidence that there are transient shallow reservoirs with partial melts beneath active volcanoes in the upper crustal layers of the SVZ, or there are also temporal interruptions in magma rise (Morgado et al. 2015; Morgado et al. 2017). Magmatic compartments controlled by major fault systems appear as medium-low resistivity anomalies (Cordell et al. 2018; Díaz et al. 2020). Therefore, the prevailing tectonic configuration in the area, the interaction between LOFS and ATF, would promote the development of a long-lived shallow reservoir (Pérez-Flores et al. 2016; Sanchez-Alfaro et al. 2016).

In the case of active Lonquimay volcano, our model does not show a strongly conductive anomaly in the crust that can be associated with a melt zone and a near-surface magmatic reservoir. The explanation for this may lie that the expected sub-surface magmatic reservoir is displaced towards to the southeast of the main volcanic edifice as have been described in other volcanoes

of SVZ (Moreno and Gardeweg 1989; Barrientos and Acevedo-Aránguiz 1992; Kapinos et al. 2016). Therefore, the shallow reservoir fails to be revealed by our model.

Additionally, in our model there would be no evidence of a link between shallow magmatic system of Lonquimay volcano with the conductive feature, C1 (Figure 6.6 and 6.7). The local stress regime of the upper crust seems to play a direct role in the spatial distribution of the volcanic centers. Thus, the eastward flexure of the LOFS appears to play an important role as a barrier. As a result, Lonquimay and Tolhuaca volcanoes having apparently independent systems (Barrientos and Acevedo-Aránguiz 1992).

6.4.2. Near surface conductive anomalies

In this study, we also provide a more detailed electrical resistivity model that images the hydrothermal alteration units in the Tolhuaca geothermal system. The 3-D model shows a zone of conductive anomalies (<40 Ωm), spatially distributed near the surface (Figure 6.5a and c). Within this zone, two conductive layers, C2 and C3 of high conductive anomalies <20 Ωm are identified at different depths, on the northwest flank of Tolhuaca volcano.

At a depth of 1500 m about sea level (a.s.l.) is the uppermost layer, C2, with a thickness of ~300 m (Figure 6.9b and d). It extends approximately 3 km in NW direction, following the trend of hot springs and the lineaments of the ancient eruptive centers of Tolhuaca volcano (Figure 6.2). Two maximum conductive anomalies (<10 Ωm) are distinguished in north and south ends (Figure 6.9b). This layer leads to an impermeable clay-cap of the Tolhuaca geothermal system (Melosh et al. 2012). Argillic material mapped at the surface and in the wells (Lohmar et al. 2012a; Sanchez-Alfaro et al. 2016), confirms that argillic alteration would be the primary cause of the high conductive layer (Melosh et al. 2012; Melosh et al. 2010). However, correlating our MT resistivity model with alteration mapped in the wells (Figure 6.9), we observed a vertical offset of ~300 m between the high conductive layer and the argillic alteration, which could be related to the discretization of the mesh design in the model. Refining the cell size in the model, e.g., using a cell thickness of 25 m from the surface to the base of the clay cap could be a solution to the offset. A new feature that has not yet been imaged in previous MT studies is the electrical conductor C4, which is located approximately between 750 and 350 m a.s.l (Figure 6.9b). C4 is a lower layer of ~400 m thick and extending 1500 m in the
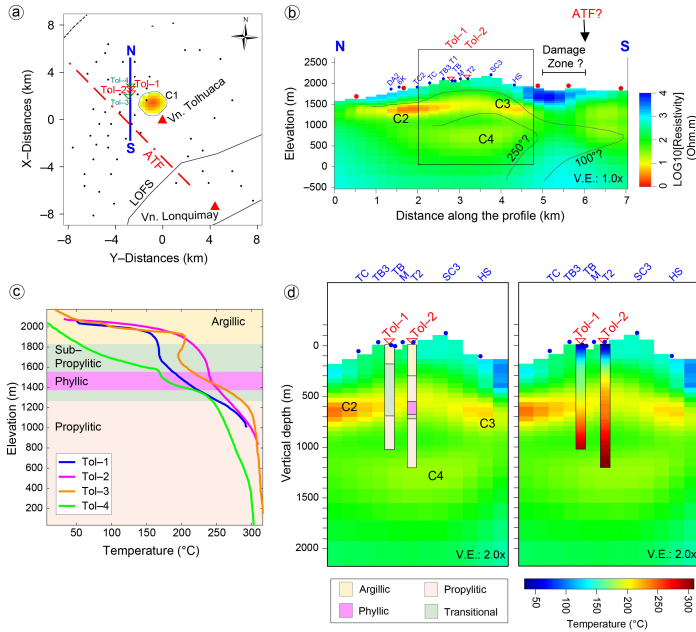
Figure 6.9.: a) Location of the N-S profile shown in b. ATF: Andean Transverse Fault; LOFS: Liquiñe-Ofqui Fault System; Tol-1, Tol-2: slim wells; Tol-3, Tol-4: deep wells. Black dots represent MT stations. b) N-S vertical section with a vertical exaggeration of 1x. Section running parallel to wells and the thermal manifestation and located to the west of the high conductive anomaly. The figure also includes an interpretation of the well temperature (modified after Melosh et al. 2012). Blue dots represent hot springs. c) Temperature vs. elevation profiles for the Tol-1 (blue line), Tol-2 (magenta line), Tol-3 (orange line) and Tol-4 (green line) wells (modified after Sanchez-Alfaro et al. 2016). Four structural-mineralogical zones are shown as a reference (modified after Lohmar et al. 2012a; Sanchez-Alfaro et al. 2016). d) Zoom of the central part of the N-S section shown in b. The figure include hydrothermal alteration units from Tol-1 and Tol-2 wells (Lohmar et al. 2012a), the ∼300 m thick uppermost high conductive anomaly, and the lower low-intermediate conductive anomalies. Note that the scale refers to the vertical extension of the wells.

N-S direction (Figure 6.9b and d), centered under a C1. This layer is slightly more resistive than the upper layer (C2 and C3) and appears to be linked to the high conductive anomaly (C1) located to the east beneath Tolhuaca volcano (Figure 6.7c). In addition, this layer lies between two horizontal zones, R3 and R4 (Figure 6.10), of intermediate low resistivity (∼200 Ωm) (Figure 6.9d), that might correspond to the reservoir zones. Therefore, it appears to be driving the development of two different reservoirs (shallow

(R3) and deep reservoir (R4) (Figure 6.10)), which could differ in temperature, geochemistry of the fluid and residence time.

6.4.3. Implications from hydrothermal alteration

According to the theoretical conceptual model used to explain electrical re-sistivity patterns observed at most high-temperature geothermal reservoirs (Anderson et al. 2000; Melosh et al. 2010; Ussher et al. 2000), our MT resistivity model is correlated with mineral alteration zoning (Figure 6.9c). Likewise, temperature logs from Tol-1, Tol-2, Tol-3 and Tol-4 (Figure 6.9c) were used to assess the performance of the MT resistivity imaging. Thus, Figure 6.9 shows a detailed NS slice of the upper 3 km transecting the Tolhuaca geothermal system at the location of the slim hole wells Tol-1 and Tol-2.

Smectite, illite and chlorite are especially known for being the main mineral phase of clay-caps in volcanic geothermal systems. Smectite and chlorite are observed at all wells from shallow depths and up to the surface (Lohmar et al. 2012a; Sanchez-Alfaro et al. 2016). For detailed alteration data of wells please refer to Lohmar et al. 2012a and Melosh et al. 2012. In the wells Tol-1 and Tol-2, smectite was found from the surface up to 160 m depth before an absence of alterations is observed (Figure 6.9c). In Tol-1 and Tol-2 the presence of the alteration minerals Illite, chlorite and smectite was observed between 300 and 400 m depth (Lohmar et al. 2012a; Sanchez-Alfaro et al. 2016). A minor presence of alteration minerals was found at Tol-1 until a depth of 600 m. In the depth ranges of 500-600 m and up to 1000 m a strong presence of alteration minerals of varying thickness was observed in all wells. Underneath this alteration zone, the mineral profiles are not as strong and clear as before. Starting at 800-900 m in Tol-1 and Tol-2 and 1100-1300 m in Tol-3 and Tol-4 first occurrence of epidote is documented, representing a high temperature (170°C) hydrothermal alteration mineral. Indication of smectite, illite, chlorite and epidote mineralization at depths from 1600 to 2300 m suggest another alteration zone.

The uppermost high-conductivity anomalies C2 and C3 correlate with argillic hydrothermal alteration zone, smectite and mixed smectite-illite zones (Sanchez-Alfaro et al. 2016) (Figure 6.10), and with the geometry of the associated temperature isotherm (Figure 6.9b). In figure 6.5, C2 and C3 are separate by a less conductive zone that we interpret it as an upflow zone. This is clearly visible in Figure 6.10. Therefore, anomalies C2 and C3 would form the clay-cap of the geothermal system associated with Tolhuaca volcano (Figure 6.5c).
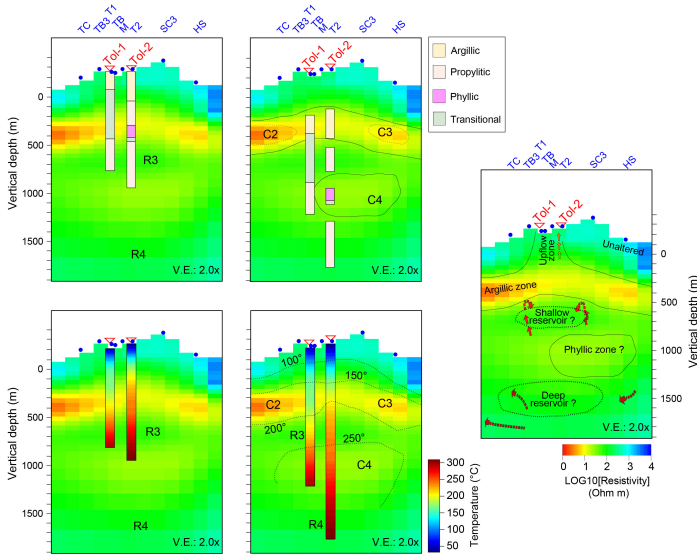
Figure 6.10.: Detailed NS-slice through the central part of Tolhuaca geothermal system shown in 9d, where the slim wells Tol-1 and Tol-2 are located. Blue circles indicate hot springs. Top left, NS-slice compared with hydrothermal alteration units from wells and correlated with conductivity anomalies. Bottom left, NS-slice compared with temperature logs and from hydrothermal alterations correlation. Middle right, schematic NS-slice interpretation showing conductive and intermediate resistivity anomalies related to the geothermal reservoir features. Note that the scale refers to the vertical extension of the wells.

It could also be related to the relatively high-temperature mineralization, which would explain the argillic alteration of the Tol-1 and Tol-2 wells close to the surface. Nearby well temperatures suggest that the upflow is currently steam-dominated down to 600 m depth. The reservoir zones are covered by steam-heated water, which may explain why our model detects the upflow zone as a more resistive anomaly compared to the argillic alteration zone.

Above C2, the 3-D inversion model shows a zone of high resistivity, which would correspond to unaltered rocks (Figure 6.10), while below and adjacent to the argillic zone (Figure 6.10), the high resistivity zone is correlated with illite to chlorite/smectite clays that could have formed from sub-propylitic alteration (Sanchez-Alfaro et al. 2016) or denominated as transitional alteration zone (Lohmar et al. 2012a). This zone could correspond to the shallower reservoir of the geothermal system (Figure 6.10).

At a deeper level below the sub-propylitic zone, an increase in conductivity ($\sim$30 Ωm) is observed, C4, which is correlated to the phyllic alteration zone described in well Tol-2. Our inversion model indicates that this anomaly could be connected to the east with highly conductive anomaly below Tolhuaca volcano (C1). This zone could have been generated through circulation of high-temperature volcanic fluids within a permeable rock which could have developed the deep reservoir below the phyllic zone. Higher altered andesite rocks may contain necessary permeability for fluid flow along faults and would also provide sufficient fluid storage to constitute a depth (Pérez-Flores et al. 2017), not previously documented, geothermal reservoir.

6.5. Conclusions

We used broadband MT data from sites deployed in the surrounding area of Tolhuaca volcano to reveal a detailed 3-D inversion model of electrical resistivity and additional evidence for the geothermal system.

To establish the best fit to the data, we use a 500 Ωm homogeneous starting model, which provides a model with electrical resistivity values in agreement with the geology and consistent with well data and geochemistry. Thereby, we provide a comprehensive 3-D inversion model of electrical resistivity compared to previous work.

The electrical resistivity model shows a shallow conductive anomaly ($<$ 20 Ωm resistivity), $\sim$3 km below the NW flank of Tolhuaca volcano, connected with a sub-vertical anomaly of intermediate resistivity ($\sim$500 Ωm). We interpret the shallow conductor as a magmatic storage compartment, which would be in a mature and partly crystalline phase. This magmatic compartment would have been fed from deep crustal zones by a sub-vertical dipping basaltic-andesitic mush column, which would act as a preferential pathway for the ascent of hydrothermal fluids.

The high-resolution resistivity images contribute to the understanding of the geothermal system associated with Tolhuaca volcano. We distinguished a $\sim$300 m thick layer of high conductivity ($<$10 Ωm) corresponding to argillic hydrothermal alteration. The MT model includes two resistive bodies ($\sim$200 Ωm) in the upper crust below the argillic alteration layer laterally offset to the west beneath the extinct Tolhuaca crater, which would correspond to a shallow reservoir R3 ($\sim$1000 m from the surface) and a deep reservoir R4

(>1800 m from the surface) that had so far not been identified by resistivity models.

Evidence for rapid heating events is provided by Melosh et al. 2012, who found borehole temperatures at Tol-4 and Tol-3 to be nearly 100°C higher than those inferred from fluid inclusions trapped in hydrothermally altered rocks in the same wells. These results would confirm that Tolhuaca magmatic and hydrothermal systems are connected and that magmatic volatiles are transported to the surface through faults and fracture pathways.

Consequently, our resistivity model provides evidence of structural control of the ATF faults, as a promoter of the long residence of magma reservoirs in the crust, which would serve as hosts for the development of heat sources for geothermal systems. Since we found no indications of a deep conductor in the study area, such as those observed in other high enthalpy geothermal systems, we conclude that the shallow magmatic deposit, which is cooling but still hot, is the heat source of the geothermal system. It is not located below the geothermal field but laterally offset.

On the other hand, we provide the first electrical resistivity image that may constitute a test of the hypothesis of the existence of independent magmatic systems between the major volcanic edifices present in Tolhuaca volcano and Lonquimay volcanic complex. The magmatic systems are possibly separated by the tectonic activity associated with the bending of the branches of the Liquiñe-Ofqui Fault System.

Future work should expand the investigated area, ideally with MT station coverage east of Tolhuaca volcano and south-southeast of Lonquimay volcano, which may significantly improve the 3-D inversion result, and image a likely shallow magma reservoir beneath Lonquimay. In addition, joint inversion or integration of multiple geophysical data sets (e.g., gravity, seismic) would also be beneficial for a further study of the volcanic chain.

Supplementary Material

Inversion test settings

The resistivity of the homogeneous starting model was chosen after some inversion tests on four different resistivity values: 10, 100, 500, and 1000 Ωm, settings A, B, C, and D respectively, described in Table S6.1. Each test hence required a different number of iterations. The final RMS range is between 1.382 and 1.652. The starting-model resistivity of 10 and 100 Ωm resulted in the lowest RMS. The 10 Ωm test resulted in the lowest RMS and provided an overestimated resistivity contrast. For this reason and due to the average apparent resistivity of all the sites, the resistivity of 500 Ωm was chosen for the starting model. We also tested different tensor settings (B, E, F) for the 500 Ωm starting model and the best setting was reached with both tensors (Z+T) inverted. Additionally, we tested the error floor. The best case was obtained using a 10% error floor for non-diagonal components of Z, 15% for diagonal components of Z and 8% for T components as shown in Table S6.1.

Table 6.1.: The inversion test settings performed on the MT data set of Tolhuaca. Inversions A, B, C, D, and E inverted, respectively, full Z and T and same error settings for different initial resistivity (half-space). Inversion A, E, and F inverted different impedance and error settings for 500 Ωm half-space.

Settings	A	B	C	D	E	F
Starting model	10 Ωm	100 Ωm	500 Ωm	1000 Ωm	500 Ωm	500 Ωm
Tensor inverted	$Z + T$	$Z + T$	$Z + T$	$Z + T$	$Z + T$	Z
Error floor $Z_{xy}Z_{yx}$	10%	10%	10%	10%	10%	10%
Error floor $Z_{xy}Z_{yx}$	15%	15%	15%	15%	10%	15%
Error floor $Z_{xy}Z_{yx}$	8%	8%	8%	8%	8%	-
Iterations	56	56	55	55	53	59
RMS	1.382	1.349	1.479	1.652	1.912	2.11

Sensitivity test
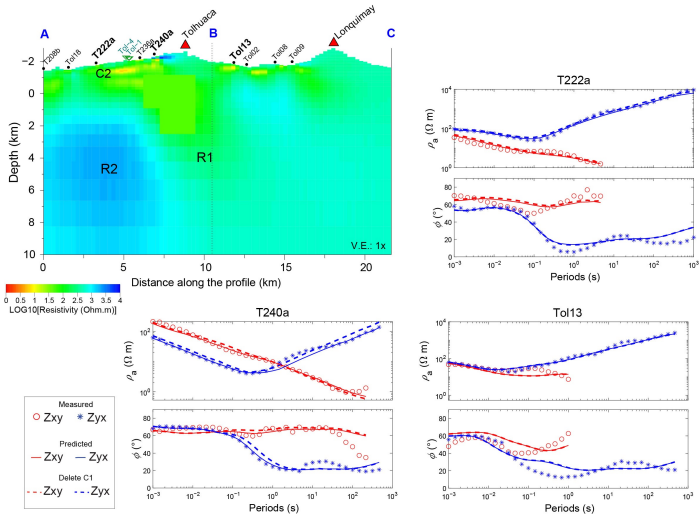
Figure 6.11.: Sensitivity test of conductor C2. a) Resistivity block (50 Ωm; resistivity of surrounding cells) is inserted instead of C2 anomaly. b) and c) Two examples of apparent resistivity and phase curves of the non-diagonal components of the MT inversion model. Red represents the Z_{xy} component, and blue the Z_{yx} component. The thin line represents the predicted data for the preferred model shown in Figure 3. The thick dash line represents the sensitivity test.

Table 6.2.: The inversion test settings performed on the MT data set of Tolhuaca. Inversions A, B, C, DE inverted, respectively, full Z and T and same error settings for different initial resistivity (half-space). Inversion A, E, F inverted different impedance and error settings for 500 Ωm half-space.

	T222a	T240a	Tol13
RMS: inversion	1.121	1.001	1.231
RMS: forward	1.131	1.024	1.258

7. Comprehensive discussion

Geothermal energy represents an important renewable resource that is characterized by base-load capability and low to zero CO_2 emission. Since 2015, Chile has started its electric power with an installed capacity of 48 MWel at Cerro Pabellon in the Northern Andean Cordillera (Cappetti et al. 2020). This capacity build-up positions Chile next to traditional geothermal countries such as the Philippines, New Zealand, and Costa Rica. Although the development of a number of high enthalpy fields such as the Tolhuaca in 2016, have been ceased, doubling of the installed electric capacity is envisaged by 2025 (Huttrer 2020). However, high traditionally, geothermal resources in Chile have been used for recreational and touristic purposes with thermal waters collected from natural hot springs and piped to buildings and pools (Vargas-Payera et al. 2020). Geothermal energy of 228.91 TJ per year is used at 29 locations for direct use and spa; among those are the Centro Termal Armada Liquiñe - Los Ríos and the Puyuhuapi Lodge - Aysén regions (Lund and Toth 2021). Although more than 20 thermal springs are located in the Pucón/Villarica area, geothermal energy there is still marginally used.

To extend and accelerate the utilization of geothermal energy in Chile, different strategies may be applied. Guided by the expected high enthalpy, most industrial projects focus on the exploitation of reservoirs directly linked to the volcanoes such as Cerro Pabellón. The presented thesis follows the concept of gaining knowledge from natural outflow zones in order to transfer it to other areas. Therefore, fluid pathways to natural thermal springs (Held et al. 2016) along fault zones and their connection to the deep underground are first investigated in the Pucón/Villarrica area using magnetotelluric methods. Findings from such electrically visualized thermal fluid pathways along faults and fractures are then compared to structures in the high enthalpy reservoir in the Tolhuaca geothermal field.

In the following, a comparative analysis of the subsurface observations in the Pucón/Villarrica area (chapters 4 and 5) is collated with key subsurface structures from the Tolhuaca area (chapter 6) with the aim to understand the

significance of faults and fractures in high-enthalpy fields.

Key findings: Pucón/Villarrica area

The characteristics of the Pucón/Villarica area is the co-existence of low-to medium thermal water outflows and magmatic pathways leading to volcanic edifices. In the following, we summarize the characteristics for both, hydrothermal and magmatic features, next to and distant from the Villarrica-Quetrupillán-Lanín volcanic chain.

Hydrothermal key features

The 3-D MT model discloses anomalies of low electric resistivity of 20-30 Ωm
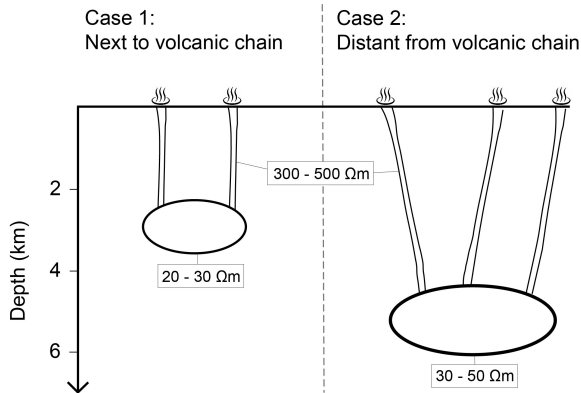
Figure 7.1.: Summary of hydrothermal key elements that were observed crossing to the main tectonic structures in the Pucón/Villarrica area.

and 30-50 Ωm close (case 1, Figure 7.1) and distant (case 2, Figure 7.1) to the volcanic chain at comparably shallow crustal levels of about 3 and 5 kilometers, respectively. Both anomalies are connected to thermal springs through sub-vertical anomalies at intermediate resistivity of about 300-500 Ωm. The geometry of these matches the existing fault pattern in the area. Evidence a for this coincidence is provided by the match of the anomaly C1 (Figure 4.5) with the eastern branch of the Liquiñe-Ofqui Fault System. In conclusion, the low resistivity anomalies may represent the reservoir zones from which the thermal springs in the area are fed through faults that function as thermal water conduits. It has been shown that the fluids are of meteoric fluid origin (Held et al. 2018). Note that these findings propose a fractured reservoir of

possibly medium temperature, located to the south of Lake Caburgua and east of LOFS. This is in agreement with geochemical studies (Held et al. 2018; Nitschke et al. 2018) and coincide with location of hot springs and thermal spa.

Magmatic key features

Similar to the pure hydrothermal key feature in the area close to the volcanic
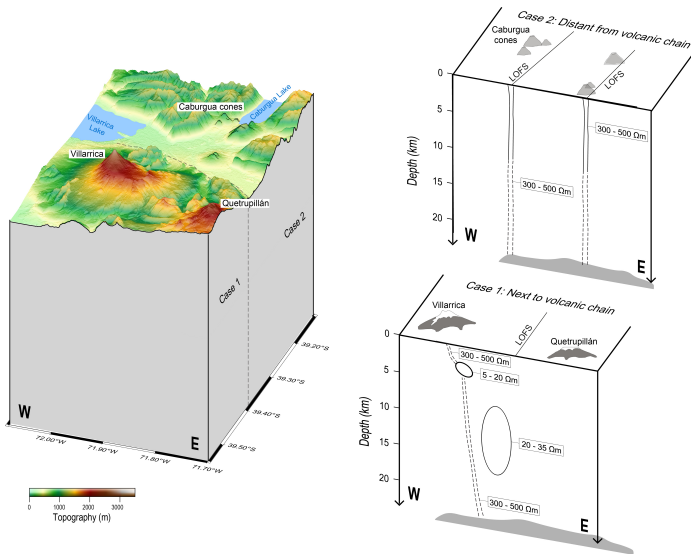
Figure 7.2.: Summary of magmatic key elements that were observed crossing to the main tectonic structures in the Pucón/Villarrica area.

chain, we observe a low resistive anomaly at shallow depth of <5 km (Figure 7.2). Note that the resistivity of 5-20 Ωm is comparably low. This in combination with the occurrence of seismicity at rim of this anomaly prior to eruptions in 2015 as well as the current volcanic activity of the in the Los Nevados and the Villarrica craters suggest the anomaly being a key magmatic feature. Furthermore, related thermal springs reveal a magmatic origin. The 3-D MT model furthermore exhibits a second crustal conductor (20-35 Ωm) north of the inactive Quetrupillán volcano. Its resistivity anomaly persists vertically between 8 and <20 km depth. At the shallow level it links to the eastern brunch of the LOFS close to the intersection with ATF, while at depth its main strike aligns NE-SW parallel to the adjacent Los Nevados vents.

A connection at several hundreds of Ωm to the surface or between the two conductors such as observed for the hydrothermal key features are less evident. On the contrary, the two magmatic features are spatially separated. However, the suggested occurrence of a western branch of the LOFS crossing the volcanic chain could represent a connection between the upper 5-20 Ωm anomaly and deep-seated anomalies the are observed in the long-period data. Distant from the volcanic chain, similar deep connections along the LOFS are indicated feeding the monogenetic cones. This suggests that LOFS is an important structural feature in the magmatic-hydrothermal system and that vertical fluid ascent may occur through this structure.

The magmatic system in the Pucón/Villarrica area is complex, trans-crustal and three-dimensional. It is not consistent with simple conceptual models that imply a single magma reservoir in the crust and magma movement driven solely by buoyancy. Our results indicate a system that includes magmatic bodies at deep, intermediate and shallow depth as well as hydrothermal reservoirs that are partly connected to each other and feed different hydrothermal and magmatic manifestations at the surface. Our results furthermore reveal faults a main connectors.

Key findings: Tolhuaca area

With a temperature of 309°C, the Tolhuaca geothermal systems represents a

Figure 7.3.: Summary of key elements that were observed crossing to the main tectonic structures in the Tolhuaca area.

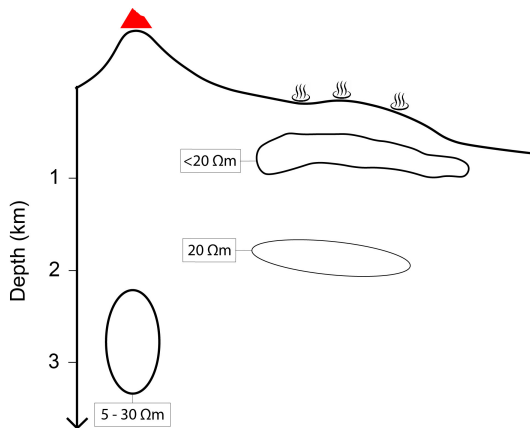high enthalpy field. Furthermore, at a first sight, the distribution of resistivity anomalies follows the classic observations in fields of high enthalpy (Figure 7.3). Compared to the Pucón/Villarrica area, all anomalies are located at shallow depth. The deepest of those occurs at >2 km beneath the NW flank of the dormant Tolhuaca volcano and is characterized by an electric resistivity of 5-30 Ωm. The location below the volcano as well as the observed resistivity values suggest a magmatic origin of this structure. This is supported by the fit of the resistivity to the petrological composition of the magma and the condition of a mature and partly crystalline, i.e., cooling but still hot, storage compartment.

At a depth of about <2 km, a low-resistivity anomaly of about 20 Ωm is encountered, above which the shallowest anomaly of <20 Ωm coincides with a depth, in which smectite-chloride assemblages reveal hydrothermal alteration as well as may explain the low resistivity. However, in this apparently classical high-enthalpy setting, a spatial extension of the latter anomaly parallel to the ATF indicates a takeover of structural control on the reservoir by the ATF in this area. Note that the Pucón/Villarrica controlling LOFS splits up into horse-tailing fault termination with a deviation of strike to the NE. In this area, the 3-D MT model exhibits no significant resistivity anomalies.

Overall conclusion

A number of similarities between to the geothermal areas, Pucón/Villarica and Tolhuaca are observed. In close vicinity of the respective volcanoes, we observe both magmatic and hydrothermal key features at similar depth and resistivity. The related vertical pathways in both cases appear to be fault controlled. Major features are linked to the respective dominating faults, the LOFS in the Pucón/Villarrica area and the ATF in the Tolhuaca area.

This main observation confirms our approach to gain knowledge from fractured reservoir producing natural hydrothermal outflows and to apply these findings to magnetotelluric exploration of high-enthalpy fields in which classical cap-layer structures often mask the fault control on the reservoir.

Bibliography

Aiuppa, Alessandro, Marcello Bitetto, Vincenzo Francofonte, Gabriela Velasquez, Claudia Bucarey Parra, Gaetano Giudice, Marco Liuzzo, Roberto Moretti, Yves Moussallam, Nial Peters, et al. (2017). "A CO2-gas precursor to the March 2015 Villarrica volcano eruption". In: *Geochemistry, Geophysics, Geosystems* 18.6, pp. 2120–2132.

Aizawa, Koki, Takao Koyama, Hideaki Hase, Makoto Uyeshima, Wataru Kanda, Mitsuru Utsugi, Ryokei Yoshimura, Yusuke Yamaya, Takeshi Hashimoto, Kenichi Yamazaki, et al. (2014). "Three-dimensional resistivity structure and magma plumbing system of the Kirishima Volcanoes as inferred from broadband magnetotelluric data". In: *Journal of Geophysical Research: Solid Earth* 119.1, pp. 198–215.

Aizawa, Koki, Takao Koyama, Makoto Uyeshima, Hideaki Hase, Takeshi Hashimoto, Wataru Kanda, Ryokei Yoshimura, Mitsuru Utsugi, Yasuo Ogawa, and Kenichi Yamazaki (2013). "Magnetotelluric and temperature monitoring after the 2011 sub-Plinian eruptions of Shinmoe-dake volcano". In: *earth, planets and space* 65.6, pp. 539–550.

Alam, Mohammad Ayaz, Pablo Sánchez, and MA Parada (2010). "Interplay of volcanism and structural control in defining the geothermal system (s) along the Liquiñe-ofqui Fault Zone, in the south-central Chile". In: *gRC transactions* 34, pp. 747–750.

Allard, Patrick (1997). "Endogenous magma degassing and storage at Mount Etna". In: *Geophysical Research Letters* 24.17, pp. 2219–2222.

Anderson, Errol, Daryl Crosby, and Greg Ussher (2000). "Bulls-eye! Simple resistivity imaging to reliably locate the geothermal reservoir". In: *Proceedings World Geothermal Congress*, pp. 909–914.

Annen, Catherine, Jonathan D Blundy, Julien Leuthold, and R Stephen J Sparks (2015). "Construction and evolution of igneous bodies: Towards an integrated perspective of crustal magmatism". In: *Lithos* 230, pp. 206–221.

Aravena, Diego, Mauricio Munoz, Diego Morata, Alfredo Lahsen, Miguel Ángel Parada, and Patrick Dobson (2016). "Assessment of high enthalpy geothermal resources and promising areas of Chile". In: *Geothermics* 59, pp. 1–13.

Araya Vargas, Jaime, NM Meqbel, Oliver Ritter, H Brasse, Ute Weckmann, G Yáñez, and B Godoy (2019). "Fluid distribution in the Central Andes subduction zone imaged with magnetotellurics". In: *Journal of Geophysical Research: Solid Earth* 124.4, pp. 4017–4034.

Archie, Gustave E (1942). "The electrical resistivity log as an aid in determining some reservoir characteristics". In: *Transactions of the AIME* 146.01, pp. 54–62.

Bahr, Karsten (1991). "Geological noise in magnetotelluric data: a classification of distortion types". In: *Physics of the Earth and Planetary Interiors* 66.1-2, pp. 24–38.

Barboni, Mélanie, Patrick Boehnke, Axel K Schmitt, T Mark Harrison, Phil Shane, Anne-Sophie Bouvier, and Lukas Baumgartner (2016). "Warm storage for arc magmas". In: *Proceedings of the National Academy of Sciences* 113.49, pp. 13959–13964.

Barrientos, Sergio E and Patricio S Acevedo-Aránguiz (1992). "Seismological aspects of the 1988–1989 Lonquimay (Chile) volcanic eruption". In: *Journal of Volcanology and Geothermal Research* 53.1-4, pp. 73–87.

Barton, Colleen A, Mark D Zoback, and Daniel Moos (1995). "Fluid flow along potentially active faults in crystalline rock". In: *Geology* 23.8, pp. 683–686.

Becken, Michael, Oliver Ritter, SK Park, PA Bedrosian, Ute Weckmann, and Michael Weber (2008). "A deep crustal fluid channel into the San Andreas Fault system near Parkfield, California". In: *Geophysical Journal International* 173.2, pp. 718–732.

Bedrosian, PA, MJ Unsworth, GD Egbert, and CH Thurber (2004). "Geophysical images of the creeping segment of the San Andreas fault: implications for the role of crustal fluids in the earthquake process". In: *Tectonophysics* 385.1-4, pp. 137–158.

Bedrosian, Paul A, Jared R Peacock, Esteban Bowles-Martinez, Adam Schultz, and Graham J Hill (2018). "Crustal inheritance and a top-down control on arc magmatism at Mount St Helens". In: *Nature Geoscience* 11.11, pp. 865–870.

Bense, VF, Tom Gleeson, SE Loveless, Olivier Bour, and Jacek Scibek (2013). "Fault zone hydrogeology". In: *Earth-Science Reviews* 127, pp. 171–192.

Bertrand, EA, TG Caldwell, GJ Hill, EL Wallin, SL Bennie, N Cozens, SA Onacha, GA Ryan, C Walter, A Zaino, et al. (2012). "Magnetotelluric imaging of upper-crustal convection plumes beneath the Taupo Volcanic Zone, New Zealand". In: *Geophysical Research Letters* 39.2.

Bonafede, M, M Dragoni, and E Boschi (1984). "Heat diffusion and size reduction of a spherical magma chamber". In: *Bulletin volcanologique* 47.2, pp. 343–347.

Brahm, Raimundo, Miguel Angel Parada, Eduardo Morgado, Claudio Contreras, and Lucy Emma McGee (2018). "Origin of Holocene trachyte lavas of the Quetrupillán volcanic complex, Chile: examples of residual melts in a rejuvenated crystalline mush reservoir". In: *Journal of Volcanology and Geothermal Research* 357, pp. 163–176.

Brasse, Heinrich, Gerhard Kapinos, Yuguo Li, Lutz Muetschard, Wolfgang Soyer, and Diane Eydam (2009). "Structural electrical anisotropy in the crust at the South-Central Chilean continental margin as inferred from geomagnetic transfer functions". In: *Physics of the Earth and Planetary Interiors* 173.1-2, pp. 7–16.

Brasse, Heinrich and Wolfgang Soyer (2001). "A magnetotelluric study in the Southern Chilean Andes". In: *Geophysical Research Letters* 28.19, pp. 3757–3760.

Brown, Stephen R and Ronald L Bruhn (1998). "Fluid permeability of deformable fracture networks". In: *Journal of Geophysical Research: Solid Earth* 103.B2, pp. 2489–2500.

Cagniard, Louis (1953). "Basic theory of the magneto-telluric method of geophysical prospecting". In: *Geophysics* 18.3, pp. 605–635.

Caine, Jonathan Saul, James P Evans, and Craig B Forster (1996). "Fault zone architecture and permeability structure". In: *Geology* 24.11, pp. 1025–1028.

Caldwell, T Grant, Hugh M Bibby, and Colin Brown (2004). "The magnetotelluric phase tensor". In: *Geophysical Journal International* 158.2, pp. 457–469.

Cappetti, G, N Giorgi, A Arias, G Volpi, G Rivera, M Cei, M Fedeli, G Di Marzio, M Pasti, S Massei, et al. (2020). "The Cerro Pabellón Geothermal Project (Chile): from Surface Exploration to Energy Production". In: *Proceedings*.

Cembrano, Jose, Alain Lavenu, Gonzalo Yañez, Rodrigo Riquelme, Marcelo García, Gabriel González, and Gerard Hérail (2007). "Neotectonics". In: *The geology of Chile* 9, pp. 231–262.

Cembrano, José, Francisco Hervé, and Alain Lavenu (1996). "The Liquiñe Ofqui fault zone: a long-lived intra-arc fault system in southern Chile". In: *Tectonophysics* 259.1-3, pp. 55–66.

Cembrano, José and Luis Lara (2009). "The link between volcanism and tectonics in the southern volcanic zone of the Chilean Andes: a review". In: *Tectonophysics* 471.1-2, pp. 96–113.

Cembrano, José, Alain Lavenu, Peter Reynolds, Gloria Arancibia, Gloria López, and Alejandro Sanhueza (2002). "Late Cenozoic transpressional ductile deformation north of the Nazca–South America–Antarctica triple junction". In: *Tectonophysics* 354.3-4, pp. 289–314.

Cembrano, José, Elizabeth Schermer, Alain Lavenu, and Alejandro Sanhueza (2000). "Contrasting nature of deformation along an intra-arc shear zone, the Liquiñe–Ofqui fault zone, southern Chilean Andes". In: *Tectonophysics* 319.2, pp. 129–149.

Charrier, R, O Baeza, S Elgueta, JJ Flynn, P Gans, S Mahlburg Kay, N Muñoz, AR Wyss, and E Zurita (2002). "Evidence for Cenozoic extensional basin development and tectonic inversion south of the flat-slab segment, southern Central Andes, Chile (33–36 SL)". In: *Journal of South American Earth Sciences* 15.1, pp. 117–139.

Chave, Alan D and Alan G Jones (2012). *The magnetotelluric method: Theory and practice*. Cambridge University Press.

Collignon, Marine, Carlo Cardellini, Sylvia Duprat-Oualid, Øyvind Hammer, Giovanni Chiodini, Jean Vandemeulebrouck, Diego Gonzalez-Vidal, Alberto Espinoza, Andrés Tassara, and Joel Ruch (2021). "Carbon dioxide diffuse emission at the Tolhuaca hydrothermal system (Chile) controlled by tectonics and topography". In: *Journal of Volcanology and Geothermal Research* 417, p. 107316.

Comeau, Matthew J, Martyn J Unsworth, Faustino Ticona, and Mayel Sunagua (2015). "Magnetotelluric images of magma distribution beneath Volcán Uturuncu, Bolivia: Implications for magma dynamics". In: *Geology* 43.3, pp. 243–246.

Cooke, David R, Orlando Rivera, José Piquer, and Gonzalo Yáñez (2019). "Long-lived crustal damage zones associated with fault intersections in the high Andes of Central Chile". In: *Andean Geology* 46.2, pp. 223–239.

Cooper, Kari M and Adam JR Kent (2014). "Rapid remobilization of magmatic crystals kept in cold storage". In: *Nature* 506.7489, pp. 480–483.

Cordell, Darcy, Martyn J Unsworth, Daniel Diaz, Valentina Reyes-Wagner, Claire A Currie, and Stephen P Hicks (2019). "Fluid and melt pathways in the central Chilean subduction zone near the 2010 Maule earthquake (35–36 °S) as inferred from magnetotelluric data". In: *Geochemistry, Geophysics, Geosystems* 20.4, pp. 1818–1835.

Cordell, Darcy, Martyn J Unsworth, and Daniel Díaz (2018). "Imaging the Laguna del Maule Volcanic Field, central Chile using magnetotellurics: Evidence for crustal melt regions laterally-offset from surface vents and lava flows". In: *Earth and Planetary Science Letters* 488, pp. 168–180.

Córdova, Loreto, Alex Alarcón, Cristian Mardones, Carlos Cardona, Fernando Gil, Gonzalo Rojas, Jonathan Quijada, Hélène Le Mèvel, Kurt Feigl, Chuck De Mets, et al. (2015). "Monitoreo de la deformación en volcanes chilenos mediante técnica GPS, resultados asociados a la actividad de los volcanes La-

guna del Maule, Copahue y Villarrica". In: *XIV Congreso Geológico Chileno*. Colegio de Geólogos de Chile La Serena.

Cruden, AR and RF Weinberg (2018). "Mechanisms of magma transport and storage in the lower and middle crust—magma segregation, ascent and emplacement". In: *Volcanic and igneous plumbing systems*, pp. 13–53.

Delgado, Francisco, Matthew E Pritchard, Susanna Ebmeier, Pablo González, and Luis Lara (2017). "Recent unrest (2002–2015) imaged by space geodesy at the highest risk Chilean volcanoes: Villarrica, Llaima, and Calbuco (Southern Andes)". In: *Journal of Volcanology and Geothermal Research* 344, pp. 270–288.

DeMets, Charles, R Go Gordon, DF Argus, and Seth Stein (1990). "Current plate motions". In: *Geophysical journal international* 101.2, pp. 425–478.

Díaz, Daniel, Heinrich Brasse, and Faustino Ticona (2012). "Conductivity distribution beneath Lascar volcano (Northern Chile) and the Puna, inferred from magnetotelluric data". In: *Journal of Volcanology and Geothermal Research* 217, pp. 21–29.

Díaz, Daniel, Wiebke Heise, and Fernando Zamudio (2015). "Three-dimensional resistivity image of the magmatic system beneath Lastarria volcano and evidence for magmatic intrusion in the back arc (northern Chile)". In: *Geophysical Research Letters* 42.13, pp. 5212–5218.

Díaz, Daniel, Felipe Zúñiga, and Angelo Castruccio (2020). "The interaction between active crustal faults and volcanism: A case study of the Liquiñe-Ofqui Fault Zone and Osorno volcano, southern Andes, using magnetotellurics". In: *Journal of Volcanology and Geothermal Research* 393, p. 106806.

Egbert, Gary D (1997). "Robust multiple-station magnetotelluric data processing". In: *Geophysical Journal International* 130.2, pp. 475–496.

Egbert, Gary D and John R Booker (1986). "Robust estimation of geomagnetic transfer functions". In: *Geophysical Journal International* 87.1, pp. 173–194.

Egbert, Gary D and Anna Kelbert (2012). "Computational recipes for electromagnetic inverse problems". In: *Geophysical Journal International* 189.1, pp. 251–267.

Folguera, A, E Rojas Vera, L Vélez, J Tobal, D Orts, M Agusto, Ay Caselli, and Victor Alberto Ramos (2016). "A review of the geology, structural controls, and tectonic setting of Copahue volcano, Southern Volcanic Zone, Andes, Argentina". In: *Copahue volcano*, pp. 3–22.

Folguera, Andrés, Víctor A Ramos, Reginald L Hermanns, and José Naranjo (2004). "Neotectonics in the foothills of the southernmost central Andes (37–38 °S): Evidence of strike-slip displacement along the Antiñir-Copahue fault zone". In: *Tectonics* 23.5.

Folguera, Andrés, Víctor A Ramos, and Daniel Melnick (2002). "Partición de la deformación en la zona del arco volcánico de los Andes neuquinos (36-39 S) en los últimos 30 millones de años". In: *Revista geológica de Chile* 29.2, pp. 227–240.

Gaffney, Edward S, Branko Damjanac, and Greg A Valentine (2007). "Localization of volcanic activity: 2. Effects of pre-existing structure". In: *Earth and Planetary Science Letters* 263.3-4, pp. 323–338.

Gamble, Thomas D, Wolfgang M Goubau, and John Clarke (1979). "Magnetotellurics with a remote magnetic reference". In: *Geophysics* 44.1, pp. 53–68.

Geiermann, Johannes and Eva Schill (2010). "2-D Magnetotellurics at the geothermal site at Soultz-sous-Forêts: Resistivity distribution to about 3000 m depth". In: *Comptes Rendus Geoscience* 342.7-8, pp. 587–599.

Gianelli, Giovanni and Sergio Grassi (2001). "Water–rock interaction in the active geothermal system of Pantelleria, Italy". In: *Chemical Geology* 181.1-4, pp. 113–130.

Glodny, Johannes, Helmut Echtler, Santiago Collao, Mary Ardiles, Pablo Burón, and Oscar Figueroa (2008). "Differential late paleozoic active margin evolution in South-Central Chile (37° S–40° S)–the lanalhue fault zone". In: *Journal of South American Earth Sciences* 26.4, pp. 397–411.

Glover, Paul WJ, Malcolm J Hole, and Jaume Pous (2000). "A modified Archie's law for two conducting phases". In: *Earth and Planetary Science Letters* 180.3-4, pp. 369–383.

Guo, Xuan, Bin Li, Huaiwei Ni, and Zhu Mao (2017). "Electrical conductivity of hydrous andesitic melts pertinent to subduction zones". In: *Journal of Geophysical Research: Solid Earth* 122.3, pp. 1777–1788.

Guo, Xuan, Li Zhang, Harald Behrens, and Huaiwei Ni (2016). "Probing the status of felsic magma reservoirs: Constraints from the P–T–H2O dependences of electrical conductivity of rhyolitic melt". In: *Earth and Planetary Science Letters* 433, pp. 54–62.

Hashin, Zvi and Shmuel Shtrikman (1963). "A variational approach to the theory of the elastic behaviour of multiphase materials". In: *Journal of the Mechanics and Physics of Solids* 11.2, pp. 127–140.

Hauser, Arturo (1997). *Catastro y caracterización de las fuentes de aguas minerales y termales de Chile.* 50. Servicio Nacional de Geología y Minería.

Hawkesworth, CJ, S Blake, P Evans, R Hughes, Ray Macdonald, LE Thomas, SP Turner, and G Zellmer (2000). "Time scales of crystal fractionation in magma chambers—integrating physical, isotopic and geochemical perspectives". In: *Journal of Petrology* 41.7, pp. 991–1006.

Heise, Wiebke, TG Caldwell, Hugh M Bibby, and SC Bannister (2008). "Three-dimensional modelling of magnetotelluric data from the Rotokawa geothermal field, Taupo Volcanic Zone, New Zealand". In: *Geophysical Journal International* 173.2, pp. 740–750.

Held, S, E Schill, J Schneider, F Nitschke, D Morata, T Neumann, and T Kohl (2018). "Geochemical characterization of the geothermal system at Villarrica volcano, Southern Chile; Part 1: Impacts of lithology on the geothermal reservoir". In: *Geothermics* 74, pp. 226–239.

Held, Sebastian, Eva Schill, Maximiliano Pavez, Daniel Díaz, Gerard Munoz, Diego Morata, and Thomas Kohl (2016). "Resistivity distribution from mid-crustal conductor to near-surface across the 1200 km long Liquiñe-Ofqui Fault System, southern Chile". In: *Geophysical Journal International* 207.3, pp. 1387–1400.

Hernandez-Moreno, Catalina, Fabio Speranza, and Anita Di Chiara (2014). "Understanding kinematics of intra-arc transcurrent deformation: Paleomagnetic evidence from the Liquiñe-Ofqui fault zone (Chile, 38−41° S)". In: *Tectonics* 33.10, pp. 1964–1988.

Herve, Francisco, Robert J Pankhurst, CM Fanning, Mauricio Calderón, and GM Yaxley (2007). "The South Patagonian batholith: 150 my of granite magmatism on a plate margin". In: *Lithos* 97.3-4, pp. 373–394.

Hervé, F and R Thiele (1987). "Estado de conocimiento de las megafallas en Chile y su significado tectónico". In: *Comun. Univ. Chile* 38, pp. 67–91.

Hervé, Francisco (1994). "The southern Andes between 39 and 44 °S latitude: The geological signature of a transpressive tectonic regime related to a magmatic arc". In: *Tectonics of the Southern Central Andes*. Springer, pp. 243–248.

Hickey-Vargas, R, M Sun, and S Holbik (2016). "Geochemistry of basalts from small eruptive centers near Villarrica stratovolcano, Chile: evidence for lithospheric mantle components in continental arc magmas". In: *Geochimica et Cosmochimica Acta* 185, pp. 358–382.

Hickey-Vargas, Rosemary, Hugo Moreno Roa, Leopolde Lopez Escobar, and Frederick A Frey (1989). "Geochemical variations in Andean basaltic and silicic lavas from the Villarrica-Lanin volcanic chain (39.5 °S): an evaluation of source heterogeneity, fractional crystallization and crustal assimilation". In: *Contributions to Mineralogy and Petrology* 103.3, pp. 361–386.

Hill, Graham J, Hugh M Bibby, Yasuo Ogawa, Erin L Wallin, Stewart L Bennie, T Grant Caldwell, Harry Keys, Edward A Bertrand, and Wiebke Heise (2015). "Structure of the Tongariro Volcanic system: Insights from magnetotelluric imaging". In: *Earth and Planetary Science Letters* 432, pp. 115–125.

Hill, Graham J, T Grant Caldwell, Wiebke Heise, Darren G Chertkoff, Hugh M Bibby, Matt K Burgess, James P Cull, and Ray AF Cas (2009). "Distribution of melt beneath Mount St Helens and Mount Adams inferred from magnetotelluric data". In: *Nature Geoscience* 2.11, pp. 785–789.

Huttrer, Gerald W (2020). "Geothermal power generation in the world 2015-2020 update report". In: *Proceedings world geothermal congress*. Vol. 1.

Jones, G.A. and R.W. Groom (1993). "Strike-angle determination from the magnetotelluric impedance tensor in the presence of noise and local distortion: rotate at your peril!" In: *Geophysical Journal International* 113.2, pp. 524–534.

Jordan, Teresa E, W Matthew Burns, Ricardo Veiga, Francisco Pángaro, Peter Copeland, Shari Kelley, and Constantino Mpodozis (2001). "Extension and basin formation in the southern Andes caused by increased convergence rate: A mid-Cenozoic trigger for the Andes". In: *Tectonics* 20.3, pp. 308–324.

Kapinos, Gerhard, Mansoureh Montahaei, Naser Meqbel, and Heinrich Brasse (2016). "Three-dimensional electrical resistivity image of the South-Central Chilean subduction zone". In: *Tectonophysics* 666, pp. 76–89.

Kay, Suzanne Mahlburg, Victor A Ramos, Constantino Mpodozis, and Patricia Sruoga (1989). "Late Paleozoic to Jurassic silicic magmatism at the Gondwana margin: Analogy to the Middle Proterozoic in North America?" In: *Geology* 17.4, pp. 324–328.

Kelbert, Anna, Naser Meqbel, Gary D Egbert, and Kush Tandon (2014). "ModEM: A modular system for inversion of electromagnetic geophysical data". In: *Computers & Geosciences* 66, pp. 40–53.

Kendrick, Eric, Michael Bevis, Robert Smalley Jr, Benjamin Brooks, Rodrigo Barriga Vargas, Eduardo Laurıa, and Luiz Paulo Souto Fortes (2003). "The Nazca–South America Euler vector and its rate of change". In: *Journal of South American Earth Sciences* 16.2, pp. 125–131.

Lahsen, Alfredo, Nelson Muñoz, and Miguel Angel Parada (2010). "Geothermal development in Chile". In: *Proceedings world geothermal congress, Bali, Indonesia*, pp. 25–29.

Lange, Dietrich, Jose Cembrano, Andreas Rietbrock, Christian Haberland, Torsten Dahm, and K Bataille (2008). "First seismic record for intra-arc strike-slip tectonics along the Liquiñe-Ofqui fault zone at the obliquely convergent plate margin of the southern Andes". In: *Tectonophysics* 455.1-4, pp. 14–24.

Lara, L, D Bertin, and C Vergara (2012). "El Complejo Volcánico Lonquimay: arquitectura y control estructural de la evolución magmática". In: *Congreso Geologico Chileno*. 13, pp. 522–524.

Lara, LE, H Moreno, JA Naranjo, S Matthews, and C Pérez de Arce (2006a). "Magmatic evolution of the Puyehue–Cordón Caulle Volcanic Complex (40 °S), Southern Andean Volcanic Zone: from shield to unusual rhyolitic fissure volcanism". In: *Journal of Volcanology and Geothermal Research* 157.4, pp. 343–366.

Lara, Luis (2004). "Villarrica-Lanín chain: Tectonic constraints for volcanism in a transversal alignment". In: *Villarrica Volcano (39.5 ° S), Southern Andes, Chile (Lara, L*, pp. 13–16.

Lara, Luis, Carolina Rodríguez, Hugo Moreno, and Carlos Pérez de Arce (2001). "Geocronología K-Ar y geoquímica del volcanismo plioceno superior-pleistoceno de los Andes del sur (39-42 °S)". In: *Revista geológica de Chile* 28.1, pp. 67–90.

Lara, Luis E and Jorge Clavero (2004). *Villarrica Volcano (39.5 S), Southern Andes, Chile*. Servicio Nacional de Geología y Minería.

Lara, Luis E and Andrés Folguera (2006). "The Pliocene to Quaternary narrowing of the Southern Andean volcanic arc between 37° and 41°S latitude". In: *SPECIAL PAPERS-GEOLOGICAL SOCIETY OF AMERICA* 407, p. 299.

Lara, Luis E, Alain Lavenu, José Cembrano, and Carolina Rodríguez (2006b). "Structural controls of volcanism in transversal chains: resheared faults and neotectonics in the Cordón Caulle–Puyehue area (40.5 °S), Southern Andes". In: *Journal of Volcanology and Geothermal Research* 158.1-2, pp. 70–86.

Lara, Luis E, José A Naranjo, and Hugo Moreno (2004). "Lanín volcano (39.5 S), Southern Andes: geology and morphostructural evolution". In: *Revista geológica de Chile* 31.2, pp. 241–257.

Lara, Luis E. and Hugo Moreno (2004). *Mapa geología del Área Liquiñe-Neltume. Carta Geológica de Chile, Serie Geología Básica, 83.*

Lavenu, Alain and José Cembrano (1999). "Compressional-and transpressional-stress pattern for Pliocene and Quaternary brittle deformation in fore arc and intra-arc zones (Andes of Central and Southern Chile)". In: *Journal of Structural Geology* 21.12, pp. 1669–1691.

Le Corvec, Nicolas, Thierry Menand, and Jan Lindsay (2013). "Interaction of ascending magma with pre-existing crustal fractures in monogenetic basaltic volcanism: an experimental approach". In: *Journal of Geophysical Research: Solid Earth* 118.3, pp. 968–984.

Lohmar, Silke, Miguel Parada, Francisco Gutiérrez, Claude Robin, and Marie Christine Gerbe (2012a). "Mineralogical and numerical approaches to establish the pre-eruptive conditions of the mafic Lican Ignimbrite, Villarrica Volcano (Chilean Southern Andes)". In: *Journal of Volcanology and Geothermal Research* 235, pp. 55–69.

Lohmar, Silke, Jim Stimac, Anna Colvin, Andrea González, Sergio Iriarte, Glenn Melosh, Maxwell Wilmarth, and David Sussman (2012b). "Tolhuaca volcano (southern Chile, 38.3 latitude S): New learnings from surface mapping and geothermal exploration wells". In: *Proceedings of the 12° Congreso Geológico Chileno*, pp. 443–445.

López-Escobar, Leopoldo, José Cembrano, and Hugo Moreno (1995). "Geochemistry and tectonics of the Chilean Southern Andes basaltic Quaternary volcanism (37-46 S)". In: *Andean geology* 22.2, pp. 219–234.

López-Escobar, Leopoldo, Rolf Kilian, Pamela D Kempton, and Michio Tagiri (1993). "Petrography and geochemistry of Quaternary rocks from the Southern Volcanic Zone of the Andes between 41°30and 46°00S, Chile". In: *Andean Geology* 20.1, pp. 33–55.

Lund, John W and Aniko N Toth (2021). "Direct utilization of geothermal energy 2020 worldwide review". In: *Geothermics* 90, p. 101915.

McGee, Lucy E, Raimundo Brahm, Michael C Rowe, Heather K Handley, Eduardo Morgado, Luis E Lara, Michael B Turner, Nicolas Vinet, Miguel-Ángel Parada, and Pedro Valdivia (2017). "A geochemical approach to distinguishing competing tectono-magmatic processes preserved in small eruptive centres". In: *Contributions to Mineralogy and Petrology* 172.6, p. 44.

Melnick, Daniel and Helmut P Echtler (2006). "Morphotectonic and geologic digital map compilations of the south-central Andes (36–42 S)". In: *The andes*. Springer, pp. 565–568.

Melnick, Daniel, Andrés Folguera, and Victor A Ramos (2006). "Structural control on arc volcanism: The Caviahue–Copahue complex, Central to Patagonian Andes transition (38 °S)". In: *Journal of south american Earth sciences* 22.1-2, pp. 66–88.

Melosh, Glenn, William Cumming, Dick Benoit, Max Wilmarth, Anna Colvin, Jeff Winick, Elizabeth Soto-Neira, David Sussman, Luis Urzúa-Monsalve, Tom Powell, et al. (2010). "Exploration results and resource conceptual model of the Tolhuaca Geothermal Field, Chile". In: *Proceedings, World Geothermal Congress*.

Melosh, Glenn, Joseph Moore, and Robert Stacey (2012). "Natural reservoir evolution in the Tolhuaca geothermal field, southern Chile". In: *High temperature* 500.600, p. 700.

Meqbel, Naser and Oliver Ritter (2015). "Joint 3D inversion of multiple electromagnetic datasets". In: *Geophysical prospecting* 63.6, pp. 1450–1467.

Meqbel, Naser Mohammad Meqbel (2009). "The electrical conductivity structure of the Dead Sea Basin derived from 2D and 3D inversion of magnetotelluric data". PhD thesis.

Mora Stock, Cindy Nathalie (2015). "Seismic Structure and Seismicity of the Villarrica Volcano (Southern Central Chile)". PhD thesis. Christian-Albrechts-Universität.

Moreno, H, L López-Escobar, and J Cembrano (1994). "The Villarrica-Quetrupillan-Lanin volcanic chain: a review and probable significance in the Southern Andes, Chile". In: *Congreso Geologico Chileno*. 7, pp. 339–341.

Moreno, H, J Naranjo, and E Polanco (2012). "Geología del complejo volcánico Lonquimay-Tolhuaca". In: *Carta Geológica de Chile* 1.50.000.

Moreno, Hugo and Jorge Clavero (2006). "Geología del volcán Villarrica, Regiones de la Araucanía y de los Lagos." In: *Servicio Nacional de Geología y Minería. Carta Geológica de Chile, Serie Geología Básica* 98.1.

Moreno, Hugo and Moyra C Gardeweg (1989). "La erupción reciente en el complejo volcánico Lonquimay (Diciembre 1988), Andes del Sur". In: *Andean Geology* 16.1, pp. 93–117.

Moreno, Hugo and Luis E. Lara (2008). "Geología del área Pucón-Curarrehue, regiones de La Araucanía y de Los Ríos, Escala 1: 100.000". In.

Morgado, E, MA Parada, C Contreras, A Castruccio, F Gutiérrez, and LE McGee (2015). "Contrasting records from mantle to surface of Holocene lavas of two nearby arc volcanic complexes: Caburgua-Huelemolle Small Eruptive Centers and Villarrica Volcano, Southern Chile". In: *Journal of Volcanology and Geothermal Research* 306, pp. 1–16.

Morgado, E, MA Parada, DJ Morgan, F Gutiérrez, A Castruccio, and C Contreras (2017). "Transient shallow reservoirs beneath small eruptive centres: Constraints from Mg-Fe interdiffusion in olivine". In: *Journal of Volcanology and Geothermal Research* 347, pp. 327–336.

Munoz, Gerard (2014). "Exploring for geothermal resources with electromagnetic methods". In: *Surveys in geophysics* 35.1, pp. 101–122.

Muñoz, J and CR Stern (1988). "The Quaternary volcanic belt of the southern continental margin of South America: Transverse structural and petrochemical variations across the segment between 38 °S and 39 °S". In: *Journal of South American Earth Sciences* 1.2, pp. 147–161.

Muñoz, M, H Fournier, M Mamani, J Febrer, E Borzotta, and A Maidana (1990). "A comparative study of results obtained in magnetotelluric deep soundings in Villarrica active volcano zone (Chile) with gravity investigations, distribution of earthquake foci, heat flow empirical relationships, isotopic geochemistry 87Sr/86Sr and SB systematics". In: *Physics of the Earth and Planetary Interiors* 60.1-4, pp. 195–211.

Naranjo, J, H Moreno, E Polanco, and S Young (2000). "Mapa de peligros de los volcanes del Alto Biobio. Regiones del BioBio y de la Araucanía". In: *Documento de trabajo* 15.

Newman, Gregory A, Erika Gasperikova, G Michael Hoversten, and Philip E Wannamaker (2008). "Three-dimensional magnetotelluric characterization of the Coso geothermal field". In: *Geothermics* 37.4, pp. 369–399.

Nitschke, Fabian, S Held, I Villalon, N Mundhenk, T Kohl, and T Neumann (2016). "Geochemical reservoir exploration and temperature determination at the Mt. Villarrica geothermal system, Chile". In: *Proceeding European Geothermal Congress*, pp. 19–24.

Nitschke, Fabian, Sebastian Held, Thomas Neumann, and Thomas Kohl (2018). "Geochemical characterization of the Villarrica geothermal system, Southern Chile, part II: site-specific re-evaluation of SiO2 and Na-K solute geothermometers". In: *Geothermics* 74, pp. 217–225.

NOAA, National Centers for Environmental Information (2022). *ETOPO 2022 15 Arc-Second Global Relief Model.* `www.ngdc.noaa.gov/mgg/global/global.html`, Last accessed on 2022-09-12.

Pace, Francesca, Anna Martí, Pilar Queralt, Alessandro Santilano, Adele Manzella, Juanjo Ledo, and Alberto Godio (2022). "Three-Dimensional Magnetotelluric Characterization of the Travale Geothermal Field (Italy)". In: *Remote Sensing* 14.3, p. 542.

Parada, Miguel A, Leopoldo López-Escobar, Verónica Oliveros, Francisco Fuentes, Diego Morata, Mauricio Calderón, Luis Aguirre, Gilbert Féraud, Felipe Espinoza, Hugo Moreno, et al. (2007). "Andean magmatism". In: *The geology of Chile*, pp. 115–146.

Pardo-Casas, Federico and Peter Molnar (1987). "Relative motion of the Nazca (Farallon) and South American plates since Late Cretaceous time". In: *Tectonics* 6.3, pp. 233–248.

Parker, Robert L (1977). "Understanding inverse theory". In: *Annual Review of Earth and Planetary Sciences* 5, p. 35.

Pavez, A (1997). "Geología e historia evolutiva del Complejo Volcánico Quetrupillán, Andes del Sur, 39, 5°S". In: *Congreso Geológico Chileno, No. 8: Actas.* Vol. 2.

Pavez, Maximiliano, Daniel Diaz, Heinrich Brasse, Gerhard Kapinos, Ingmar Budach, Valentin Goldberg, Diego Morata, and Eva Schill (2022). "Shallow and Deep Electric Structures in the Tolhuaca Geothermal System (S. Chile) Investigated by Magnetotellurics". In: *Remote Sensing* 14.23, p. 6144.

Pavez, Maximiliano, Eva Schill, Sebastian Held, Daniel Díaz, and Thomas Kohl (2020). "Visualizing preferential magmatic and geothermal fluid pathways via electric conductivity at Villarrica Volcano, S-Chile". In: *Journal of Volcanology and Geothermal Research* 400, p. 106913.

Peacock, Jared R, Margaret T Mangan, Darcy McPhee, and Phil E Wannamaker (2016). "Three-dimensional electrical resistivity model of the hydrothermal

system in Long Valley Caldera, California, from magnetotellurics". In: *Geophysical Research Letters* 43.15, pp. 7953–7962.

Pearce, RK, A Sánchez de la Muela, M Moorkamp, James OS Hammond, TM Mitchell, J Cembrano, J Araya Vargas, PG Meredith, P Iturrieta, N Pérez-Estay, et al. (2020). "Reactivation of fault systems by compartmentalized hydrothermal fluids in the Southern Andes revealed by magnetotelluric and seismic data". In: *Tectonics* 39.12, e2019TC005997.

Pérez-Flores, Pamela, José Cembrano, Pablo Sánchez-Alfaro, Eugenio Veloso, Gloria Arancibia, and Tomas Roquer (2016). "Tectonics, magmatism and paleo-fluid distribution in a strike-slip setting: Insights from the northern termination of the Liquiñe–Ofqui fault System, Chile". In: *Tectonophysics* 680, pp. 192–210.

Pérez-Flores, Pamela, Eugenio Veloso, José Cembrano, Pablo Sánchez-Alfaro, Martín Lizama, and Gloria Arancibia (2017). "Fracture network, fluid pathways and paleostress at the Tolhuaca geothermal field". In: *Journal of Structural Geology* 96, pp. 134–148.

Pérez-Moreno, Rodrigo, Martin Reich, Linda Daniele, Diego Morata, Sebastian Held, and Jackie Kleinsasser (2021). "Stable isotope and anthropogenic tracer signature of waters in an Andean geothermal system". In: *Applied Geochemistry* 128, p. 104953.

Petiau, Gilbert (2000). "Second generation of lead-lead chloride electrodes for geophysical applications". In: *Pure and applied geophysics* 157.3, pp. 357–382.

Piña-Varas, P, J Ledo, P Queralt, D Martínez van Dorth, A Marcuello, I Cabrera-Pérez, L D'Auria, and A Martí (2023). "Volcanic monitoring of the 2021 La Palma eruption using long-period magnetotelluric data". In: *Scientific Reports* 13.1, p. 15929.

Pinel, Virginie and Claude Jaupart (2000). "The effect of edifice load on magma ascent beneath a volcano". In: *Philosophical Transactions of the Royal Society of London. Series A: Mathematical, Physical and Engineering Sciences* 358.1770, pp. 1515–1532.

Polanco, E, H Moreno, JA Naranjo, and C Pérez de Arce (2014). "Nuevas edades Ar/Ar del Complejo Lonquimay-Tolhuaca y su contribución a la comprensión de su evolución geológica". In: *Jornadas Geológicas, Sesión Temática* 12, 139e142.

Pommier, Anne and Emmanuel Le-Trong (2011). ""SIGMELTS": A web portal for electrical conductivity calculations in geosciences". In: *Computers & Geosciences* 37.9, pp. 1450–1459.

Pritchard, ME, SL De Silva, Gary Michelfelder, G Zandt, Stephen R Mc-Nutt, J Gottsmann, ME West, J Blundy, DH Christensen, NJ Finnegan,

et al. (2018). "Synthesis: PLUTONS: Investigating the relationship between pluton growth and volcanism in the Central Andes". In: *Geosphere* 14.3, pp. 954–982.

Pruess, K and GS Bodvarsson (1984). "Thermal effects of reinjection in geothermal reservoirs with major vertical fractures". In: *Journal of Petroleum Technology* 36.09, pp. 1567–1578.

Radic, Juan Pablo (2010). "Las cuencas cenozoicas y su control en el volcanismo de los Complejos Nevados de Chillán y Copahue-Callaqui (Andes del Sur, 36-39 °S)". In: *Andean geology* 37.1, pp. 220–246.

Radic, Juan Pablo, Lisandro Rojas, Aldo Carpinelli, and Enrique Zurita (2002). "Evolución tectónica de la cuenca terciaria de Cura-Mallín, región cordillerana chileno argentina (36°30-39°00S)". In: *Congreso Geológico Argentino*. Vol. 15, pp. 233–241.

Ramos, Victor A, Vanesa D Litvak, Andrés Folguera, and Mauro Spagnuolo (2014). "An Andean tectonic cycle: From crustal thickening to extension in a thin crust (34–37 SL)". In: *Geoscience Frontiers* 5.3, pp. 351–367.

Rapela, CW and RJ Pankhurst (1992). "The granites of northern Patagonia and the Gastre Fault System in relation to the break-up of Gondwana". In: *Geological Society, London, Special Publications* 68.1, pp. 209–220.

Reyes-Wagner, Valentina, Daniel Díaz, Darcy Cordell, and Martyn Unsworth (2017). "Regional electrical structure of the Andean subduction zone in central Chile (35–36 S) using magnetotellurics". In: *Earth, Planets and Space* 69.1, pp. 1–9.

Robidoux, Philippe, Daniela Pastén, Gilles Levresse, Gloria Diaz, and Dante Paredes (2021). "Volatile Content Implications of Increasing Explosivity of the Strombolian Eruptive Style along the Fracture Opening on the NE Villarrica Flank: Minor Eruptive Centers in the Los Nevados Group 2". In: *Geosciences* 11.8, p. 309.

Rodi, William and Randall L Mackie (2001). "Nonlinear conjugate gradients algorithm for 2-D magnetotelluric inversion". In: *Geophysics* 66.1, pp. 174–187.

Rosenau, Matthias, Daniel Melnick, and Helmut Echtler (2006). "Kinematic constraints on intra-arc shear and strain partitioning in the southern Andes between 38 S and 42 S latitude". In: *Tectonics* 25.4.

Sánchez, Pablo, Pamela Pérez-Flores, Gloria Arancibia, José Cembrano, and Martin Reich (2013). "Crustal deformation effects on the chemical evolution of geothermal systems: the intra-arc Liquiñe–Ofqui fault system, Southern Andes". In: *International Geology Review* 55.11, pp. 1384–1400.

Sanchez-Alfaro, Pablo, Martin Reich, Gloria Arancibia, Pamela Pérez-Flores, José Cembrano, Thomas Driesner, Martin Lizama, Julie Rowland, Diego

Morata, Christoph A Heinrich, et al. (2016). "Physical, chemical and mineralogical evolution of the Tolhuaca geothermal system, southern Andes, Chile: insights into the interplay between hydrothermal alteration and brittle deformation". In: *Journal of Volcanology and Geothermal Research* 324, pp. 88–104.

Sánchez-Alfaro, Pablo, Martin Reich, Gloria Arancibia, Pamela Pérez-Flores, Thomas Driesner, Martín Lizama, José Cembrano, Diego Morata, and Julie Rowland (2012). "Evolution of the Tolhuaca Geothermal System: insights from mineralogy, structural data and numerical simulations". In: *XIV Congr. Geológico Chileno*, pp. 500–502.

Sernageomín (2010). *Mapa Geológico.* `http://portalgeomin.sernageomin.cl:6080/arcgis/rest/services/geoportal/GeologiaBase/MapServer/3`, Last accessed on 2020-04-25.

SERNAGEOMIN, Servicio Nacional de Geología y Minería (2020). *Portal GEOMIN: Catálogo Nacional de Geología y Minería.* `https://portalgeominbeta.sernageomin.cl`, Last accessed on 2022-11-28.

Sibson, Richard (1996). "Structural permeability of fluid-driven fault-fracture meshes". In: *Journal of Structural geology* 18.8, pp. 1031–1042.

Sibson, Richard H (1994). "Crustal stress, faulting and fluid flow". In: *Geological Society, London, Special Publications* 78.1, pp. 69–84.

Simmons, Isla C, Joaquín A Cortés, Dave McGarvie, and Eliza S Calder (2020). "Tectonic constraints on a magmatic plumbing system: The Quetrupillán Volcanic Complex (39°30S, 71°43W), Southern Andes, Chile". In: *Journal of Volcanology and Geothermal Research* 407, p. 107101.

Simmons, Isla Catherine (2021). "Quetrupillán volcanic complex, Chile: Holocene volcanism, magmatic plumbing system, and future hazards". In.

Simpson, Fiona and Karsten Bahr (2005). *Practical magnetotellurics.* Cambridge University Press.

Smith, Robert B and Ronald L Bruhn (1984). "Intraplate extensional tectonics of the eastern Basin-Range: Inferences on structural style from seismic reflection data, regional tectonics, and thermal-mechanical models of brittle-ductile deformation". In: *Journal of Geophysical Research: Solid Earth* 89.B7, pp. 5733–5762.

Somoza, Ruben (1998). "Updated azca (Farallon)—South America relative motions during the last 40 My: implications for mountain building in the central Andean region". In: *Journal of South American Earth Sciences* 11.3, pp. 211–215.

Soyer, Wolfgang (2002). "Analysis of geomagnetic variations in the Central and Southern Andes". In.

Spera, Frank J (2000). "Physical properties of magma". In: *Encyclopedia on Volcanoes*.

Spichak, Viacheslav and Adele Manzella (2009). "Electromagnetic sounding of geothermal zones". In: *Journal of Applied Geophysics* 68.4, pp. 459–478.

Stanley, William D and Richard D Tinkler (1983). *A practical, low-noise coil system for magnetotellurics*. Tech. rep. US Geological Survey.

Stern, Charles R (2004). "Active Andean volcanism: its geologic and tectonic setting". In: *Revista geológica de Chile* 31.2, pp. 161–206.

Suárez, Manuel and Carlos Emparan (1997). *Hoja Curacautin: Regiónes de la Araucania y del Biobio*. Servicio.

Szarka, L (1987). "Geophysical mapping by stationary electric and magnetic field components: a combination of potential gradient mapping and magnetometric resistivity (MMR) methods". In: *Geophysical prospecting* 35.4, pp. 424–444.

Thiele, R, A Lahsen, H Moreno, J Varela, M Vergara, and F Munizaga (1987). "Estudio Geológico Regional a Escala 1: 100.000 de la Hoya superior y curso médio del rio Biobío". In: *ENDESA-Departamento de Geología y Geofísica, Universidad de Chile. Informe Inédito*.

Thomson, Stuart N (2002). "Late Cenozoic geomorphic and tectonic evolution of the Patagonian Andes between latitudes 42 S and 46 S: An appraisal based on fission-track results from the transpressional intra-arc Liquiñe-Ofqui fault zone". In: *Geological Society of America Bulletin* 114.9, pp. 1159–1173.

Tietze, Kristina and Oliver Ritter (2013). "Three-dimensional magnetotelluric inversion in practice—the electrical conductivity structure of the San Andreas Fault in Central California". In: *Geophysical Journal International* 195.1, pp. 130–147.

Tikhonov, AN (1950). "On determining electrical characteristics of the deep layers of the Earth's crust". In: *Doklady*. Vol. 73. 2. Citeseer, pp. 295–297.

Tormey, Daniel R, Rosemary Hickey-Vargas, Frederick A Frey, and Leopoldo López-Escobar (1991). "Recent lavas from the Andean volcanic front (33 to 42 S); interpretations of along-arc compositional variations". In: *Andean magmatism and its tectonic setting* 265, pp. 57–77.

Tyburczy, James A and Harve S Waff (1983). "Electrical conductivity of molten basalt and andesite to 25 kilobars pressure: Geophysical significance and implications for charge transport and melt structure". In: *Journal of Geophysical Research: Solid Earth* 88.B3, pp. 2413–2430.

Unsworth, Martyn and Paul Bedrosian (2004a). "On the geoelectric structure of major strike-slip faults and shear zones". In: *Earth, planets and space* 56, pp. 1177–1184.

Unsworth, Martyn and Paul A Bedrosian (2004b). "Electrical resistivity structure at the SAFOD site from magnetotelluric exploration". In: *Geophysical research letters* 31.12.

Unsworth, Martyn, Gary Egbert, and John Booker (1999). "High-resolution electromagnetic imaging of the San Andreas fault in central California". In: *Journal of Geophysical Research: Solid Earth* 104.B1, pp. 1131–1150.

Ussher, Greg, Colin Harvey, Roy Johnstone, and Errol Anderson (2000). "Understanding the resistivities observed in geothermal systems". In: *proceedings world geothermal congress*. Kyushu Japan, pp. 1915–1920.

Vargas-Payera, Sofía, Amanda Martínez-Reyes, and Olivier Ejderyan (2020). "Factors and dynamics of the social perception of geothermal energy: Case study of the Tolhuaca exploration project in Chile". In: *Geothermics* 88, p. 101907.

Walker, Richard J, Robert E Holdsworth, Peter J Armitage, and Daniel R Faulkner (2013). "Fault zone permeability structure evolution in basalts". In: *Geology* 41.1, pp. 59–62.

White, Robert S, Marie Edmonds, John Maclennan, Tim Greenfield, and Thorbjorg Agustsdottir (2019). "Melt movement through the Icelandic crust". In: *Philosophical Transactions of the Royal Society A* 377.2139, p. 20180010.

Wiese, von H (1962). "Geomagnetische Tiefentellurik Teil II: die Streichrichtung der Untergrundstrukturen des elektrischen Widerstandes, erschlossen aus geomagnetischen Variationen". In: *Geofisica pura e applicata* 52.1, pp. 83–103.

Wrage, Jackie, Daniele Tardani, Martin Reich, Linda Daniele, Gloria Arancibia, José Cembrano, Pablo Sánchez-Alfaro, Diego Morata, and Rodrigo Pérez-Moreno (2017). "Geochemistry of thermal waters in the Southern Volcanic Zone, Chile–Implications for structural controls on geothermal fluid composition". In: *Chemical Geology* 466, pp. 545–561.

Yoshimura, R, N Oshiman, M Uyeshima, H Toh, T Uto, H Kanezaki, Y Mochido, K Aizawa, Y Ogawa, T Nishitani, et al. (2009). "Magnetotelluric transect across the Niigata-Kobe Tectonic Zone, central Japan: A clear correlation between strain accumulation and resistivity structure". In: *Geophysical research letters* 36.20.

Žák, Jiří and Josef Klomínskỳ (2007). "Magmatic structures in the Krkonoše–Jizera Plutonic Complex, Bohemian Massif: evidence for localized multiphase flow and small-scale thermal–mechanical instabilities in a granitic magma chamber". In: *Journal of Volcanology and Geothermal Research* 164.4, pp. 254–267.

A. Declaration of authorship

Chapter 4: Visualizing preferential magmatic and geothermal fluid pathways via electric conductivity at Villarrica Volcano, S-Chile.

Citation: Pavez, M., Schill, E., Held, S., Diaz, D., & Kohl, T. (2020). Visualizing preferential magmatic and geothermal fluid pathways via electric conductivity at Villarrica Volcano, S-Chile. *Journal of Volcanology and Geothermal Research*, 400, 106913.

The study is part of a collaborative research project between Karlsruhe Institute of Technology (KIT) and the Andean Geothermal Center of Excellence (CEGA, FONDAP-CONICYT 15090013). Additional support the BMBF-CONICYT International Scientific Collaborative Research Program (FKZ01DN14033/PCCI130025) and by the state of Baden-Württemberg through bwHPC is gratefully acknowledged. I thank Gary Egbert and Anna Kelbert for the use of their ModEM inversion program and special thanks to Naser Meqbel for providing visualization program.

I re-processed the data collected in the 2013 campaign (Held et al. 2016) using a robust code based on (Egbert and Booker 1986). I conducted the 3-D inversion and forward modeling using ModEM software (Kelbert et al. 2014). I evaluate resistivity distribution in terms of hydrothermal and magmatic features. I wrote the manuscript.

Chapter 5: Magma storage and transfer in the Villarrica volcanic chain, South Chile: MT insights into volcano-tectonic interactions.

Citation: Pavez, M., Brasse, H., Kapinos, G., Diaz, D., Lara, L., & Schill, E. (2023). Magma storage and transfer in the Villarrica volcanic chain, South Chile: MT insights into volcano-tectonic interactions. *Journal of Volcanology and Geothermal Research*, 439, 107832.

The study is part of a collaborative research project between Karlsruhe Institute of Technology (KIT) and the Andean Geothermal Center of Excellence (CEGA), ANID-FONDAP projects 15090013 and ACE210005. We also thank the support of FONDECYT 1211257. Computational resources are provided by the State of Baden-Württemberg through bwHPC (BwUniCluster 2.0). Additionally, I thank Gary Egbert and Anna Kelbert for the use of their ModEM inversion program and special thanks to Naser Meqbel for providing visualization program.

I used the Broadband magnetotelluric data described in Chapter 4, while Gerhard Kapinos provided the Long-period magnetotelluric data processed. I interpolated and merged both datasets. I conducted the 3-D inversion and forward modeling using ModEM software (Kelbert et al. 2014). I evaluated resistivity distribution model. I wrote the manuscript.

Chapter 6: Shallow and Deep Electric Structures in the Tolhuaca Hydrothermal System (Chile) Investigated by Magnetotelluric.

Citation: Pavez, M., Diaz, D., Brasse, H., Kapinos, G., Budach, I., Goldberg, V., Morata, D., & Schill, E. (2022). Shallow and Deep Electric Structures in the Tolhuaca Geothermal System (S. Chile) Investigated by Magnetotellurics. *Remote Sensing*, 14(23), 6144.

The study is part of a collaborative research project between Karlsruhe Institute of Technology (KIT) and the Andean Geothermal Center of Excellence (CEGA), ANID-Fondap projects 15200001 and ACE210005. This research was funded by BMBF Client II (Federal Ministry of Education and Research, FKZ: 033R190B). The magnetotelluric data were acquired in the frame of the BrineMine project. Additional support by the KIT-Publication Fund of the Karlsruhe Institute of Technology and by the state of Baden-Württemberg through bwHPC is gratefully acknowledged.

I organized and managed the geophysical campaign in November and December 2019. Together Daniel Diaz we coordinated the research team conducting all the 25 magnetotelluric measurements. I processed the data using a robust code based on (Egbert and Booker 1986). I conducted the 3-D inversion and forward modeling using ModEM software (Kelbert et al. 2014). I evaluated resistivity distribution in terms of hydrothermal and magmatic origin. I wrote the manuscript.

B. Publications

B.1. Publications in peer-reviewed journals

Pavez, M., Brasse, H., Kapinos, G., Díaz, D., Lara, L. E., & Schill, E. (2023). Magma storage and transfer in the Villarrica volcanic chain, South Chile: MT insights into volcano-tectonic interactions. Journal of Volcanology and Geothermal Research, 439, 107832.

Pavez, M., Díaz, D., Brasse, H., Kapinos, G., Budach, I., Goldberg, V., Morata, D., & Schill, E. (2022). Shallow and Deep Electric Structures in the Tolhuaca Geothermal System (S. Chile) Investigated by Magnetotellurics. Remote Sensing, 14(23), 6144.

Goldberg, V., Winter, D., Nitschke, F., Rath, M., Held, S., Spitzmüller, L., Budach, I., Pavez, M., Morata, D., Koschikowski, J., & Kohl, T. (2021). The potential of raw material extraction from thermal brines successful milestones of the BrineMine project. Oil Gas-European Magazine, 47, 26-33.

Pavez, M., Schill, E., Held, S., Díaz, D., & Kohl, T. (2020). Visualizing preferential magmatic and geothermal fluid pathways via electric conductivity at Villarrica Volcano, S-Chile. Journal of Volcanology and Geothermal Research, 400, 106913.

Held, S., Schill, E., Pavez, M., Díaz, D., Munoz, G., Morata, D., & Kohl, T. (2016). Resistivity distribution from mid-crustal conductor to near-surface across the 1200 km long Liquiñe-Ofqui Fault System, southern Chile. Geophysical Journal International, 207(3), 1387-1400.

B.2. Presentations with abstracts

Pavez, M., Brasse, H., Kapinos, G., Diaz, D., Lara, L.E., & Schill, E. (2023) The electrical structure of Villarrica volcano, S-Chile: Oral presentation. 9th Physics of Volcanoes Workshop, Hannover.

Pavez, M., Diaz, D., Goldberg, V., Brasse, H., Budach, I., Kapinos, G., & Schill,E. (2022). New insight of the hydrothermal system beneath Tolhuaca volcano (South Chile) revealed by magnetotelluric observations: Poster presentation. 25th Electromagnetic Induction Workshop, Cesme.

Pavez, M., Cornejo-Trivino, N., Bauer, F., & Schill, E. (2021) Gravity survey in delineating geologic features of interest for deep geothermal use at Campus North of KIT: Oral presentation. 9th European Geothermal Workshop, Karlsruhe.

Pavez, M., Schill, E., Held, S., Diaz, D., & Kohl, T. (2021). Geophysical Characterization of Medium and Low Temperature Geothermal Systems Using MT: an Example of the Villarrica Area: Oral presentation. World Geothermal Congress, Reykjavik.

Pavez, M., Schill, E., Held, S., Diaz, D., & Kohl, T. (2019) Geothermal Systems Exploration in the Southern Chilean Volcanic Zone by Magnetotelluric Method: a case study at Villarrica Volcano: Poster presentation. 7th European Geothermal Workshop, Karlsruhe.

Pavez, M., Schill, E., Haaf, N., Mora-Stock, C., & Diaz, D. (2019). Indication of Forecasting Seismic Activity by Magnetotelluric Methods from Fluid Injection During Reservoir Engineering: Poster presentation. 27th IUGG General Assembly, Montreal.

Pavez, M., Schill, E., Held, S., Diaz, D., & Kohl, T. (2018). Magnetotelluric visualization of preferential fluid pathways in the geothermal system at Villarrica volcano, S-Chile: Oral presentation. XV Congreso Geologico Chileno, Concepcion.

Pavez, M., Schill, E., Held, S., & Kohl, T. (2018). High-conductivity zones linked with fluid pathways in the Villarrica geothermal system, S-Chile: Poster presentation. 6th European Geothermal Workshop, Strasbourg.

Pavez, M., Diaz, D., Held, S., & Schill, E. (2018). Magnetotelluric visualization of preferential fluid pathways in the geothermal system at Villarrica volcano, S-Chile: Poster presentation. 24th Electromagnetic Induction Workshop, Helsingor.

Pavez, M., Held, S., Diaz, D., & Schill, E. (2017). Exploration in Villarrica geothermal system from 3D magnetotellurics modelling: Oral presentation. 5th European Geothermal Workshop, Karlsruhe.